AN ABSTRACT OF THE DISSERTATION OF

Stephanie Walker for the degree of Doctor of Philosophy in Materials Science and Robotics presented on September 17 2018.

Title: Functional Materials and Techniques for Additive Manufacturing in Soft Robotics

Abstract approved:

_____

Yiğit Mengüç

This thesis outlines the development of new elastomeric materials and manufacturing processes for soft robotics. Specifically, this work describes the development of custom material formulations for use in additive manufacturing, additive manufacturing processing techniques for silicone elastomers, and multi-component additive manufacturing techniques. Material synthesis and processing is a gap in the field that needs more research to produce more predictable, higher quality, and more scalable soft robot technologies. This thesis includes papers that address the above topics, preceded by an introduction and literature review into additive manufacturing and materials characterization for soft robotics. The first work (Chapter 2) outlines the development of a custom elastomer designed to make biodegradable soft robots via 3D printing. The second work (Chapter 3) shows how liquid silicone thermoset polymers 3d printing can be improved by controlling reaction kinetics and rheology. The last work (Chapter 4) describes the process of using silicone 3D printing to embed multiple discrete sensing and electronic components into a functioning soft wearable device, with a focus on customizability. Each work describes a different part of how materials science plays a role in soft robotics, including the creation of elastomeric material, control of the elastomeric material, and combining the multiple materials in custom device manufacturing. For each work, a soft robot actuator or robot system is developed to emphasize the importance of material behavior and process development in improving soft robot manufacturing.

# Functional Materials and Techniques for Additive Manufacturing in Soft Robotics

by
Stephanie Walker

A DISSERTATION

submitted to

Oregon State University

in partial fulfillment of
the requirements for the
degree of

Doctor of Philosophy

Presented September 17, 2018
Commencement June 2019

Doctor of Philosophy dissertation of Stephanie Walker presented on September 17, 2018

APPROVED:

Major Professor, representing Materials Science and Robotics

Head of the School of Mechanical, Industrial, and Manufacturing Engineering

Dean of the Graduate School

I understand that my dissertation will become part of the permanent collection of Oregon State University libraries. My signature below authorizes release of my dissertation to any reader upon request.

Stephanie Walker, Author

# ACKNOWLEDGEMENTS

I would like to acknowledge several people who helped me during my Ph.D.

I especially thank my partner Chris who I would not have survived this experience without. I love you!

I am also very thankful to Dr. Yiğit Mengüç who provided the guidance and mentoring for all of the following work.

I am thankful to Dr. Jamie Paik who provided the guidance for my wearable device work.

I am thankful to the members of mLab and the Reconfigurable Robotics Lab for their inspiration, help, and guidance.

I am thankful for the interns I've worked with including Dylan Thrush, Anushka Pandey, Jacob Rueben, and Tessa Van Volkenburg. Their help and hard work was integral to the success of these projects.

I would like to thank my advising committee Dr. Skip Rochefort, Dr. John Simonsen, Dr. Ross Hatton, and Dr. Oksana Ostroverkhova.

# CONTRIBUTION OF AUTHORS

Chapter 1: Steph Walker – writing and editing
Yiğit Mengüç – editing
Gina Olson – editing

Chapter 2, Paper 1 of 2:

Steph Walker – wrote paper, edited paper, designed experiments, analyzed experimental data, created figures
Jacob Rueben – performed experiments
Tessa Van Volkenburg – performed experiments
Samantha Hemleben – performed motion capture experiment
Cindy Grimm – provided text for motion capture explanation
John Simonsen – adviser for the project
Yiğit Mengüç – edited the paper, adviser for the project

Chapter 2, Paper 2 of 2 (shared authorship with Jacob Rueben):

Jacob Rueben – (synthesis, FTIR, tensile/cyclic tests) wrote paper, edited paper, designed experiments, performed experiments, analyzed experimental data, created figures
Steph Walker – (concept development, synthesis, actuator production) wrote paper, edited paper, designed experiments, performed experiments, analyzed experimental data, created figures
Stephen Huhn - performed NMR experiments, analyzed and wrote NMR analysis
John Simonsen – adviser for the project
Yiğit Mengüç – main adviser for the project

Chapter 3: Steph Walker - wrote paper, edited paper, designed experiments, analyzed experimental data, created figures, co-designed printer
Uranbileg Daalkhaijav – helped perform rheology experiments, helped design rheology experiments
Dylan Thrush – co-designed printer
Callie Branyan – provided models for 3D printing
Osman Yirmibeşoğlu - provided preliminary 3D models
Gina Olson – edited paper, provided preliminary 3D models
Yiğit Mengüç – edited paper, adviser for the project

Chapter 4: Steph Walker - wrote paper, edited paper, designed experiments,

designed experimental setups, analyzed experimental data, created figures

Amir Firouzeh – advised on previous sensor work
Matthew Robertson – contributed to actuator and circuit design
Yiğit Mengüç – edited paper, adviser on the project
Jamie Paik – edited paper, main adviser on the project

Chapter 5: Steph Walker – writing and editing
Yiğit Mengüç – editing
Gina Olson – editing

TABLE OF CONTENTS

Page

TABLE OF CONTENTS (Continued)

TABLE OF CONTENTS (Continued)

TABLE OF CONTENTS (Continued)

LIST OF FIGURES

Figure Page

LIST OF FIGURES (Continued)

LIST OF FIGURES (Continued)

LIST OF TABLES

# LIST OF SYMBOLS

| | |
|---|---|
| $G'$ | (fluid) shear elastic modulus (Pa) |
| $G''$ | (fluid) shear viscous modulus (Pa) |
| tan δ | loss tangent (unitless, $G''/G'$) |
| $\sigma_y$ | (fluid) yield stress (Pa) |

# 1
# Materials Science and Additive Manufacturing for Soft Robotics

The simplest way to describe a soft robot would be to replace all or most of a hard robot's components with materials like soft elastomers, fabrics, threads, conductive fluids, and flexible films. Soft robotics research is necessary to provide devices in fields where robot compliance is advantageous, such as medical technology, wearables, safety, and navigation of unusual terrain (*1*–*9*) (Figure 1).

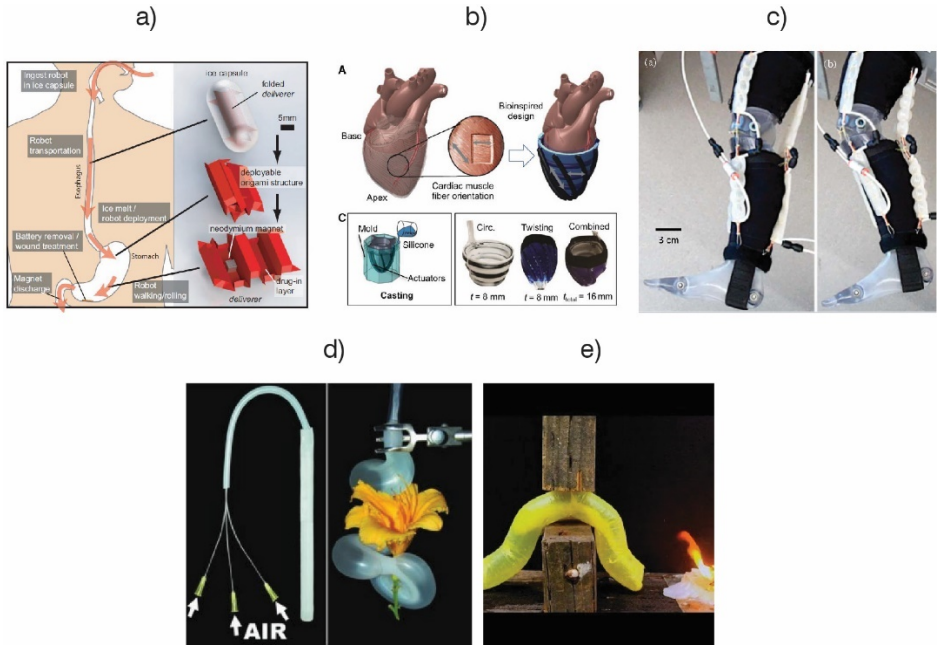


**Figure 1.** Soft robots are developed for uses such as (a,b) medical technology (*6*, *7*) (c) (including wearables (*5*)), (d) safety(*10*), and (e) navigation of unusual terrain (*9*).

In each case, the robot's compliance provides a benefit, such as ability to interact safely with the human body, ability to interact gently with delicate objects, or ability to deform significantly to move within tight spaces. Many of these tasks are not currently possible with hard robotics.

Soft robotics shares several requirements with hard robotics, including the need for electronics and control systems. However, soft robotics also relies heavily on the performance of compliant materials. But, even though compliant materials are the central focus of soft robot design, there are currently a lack of methodologies for fabricating soft robots with these materials that are repeatable, scalable, and customizable. Many soft robots are made one at a time and manually constructed either by molding or by 2D lamination. Inner mandrels or meltable wax cores are also be added to the molding process to create more complex shapes. Material choices are generally also limited to off-the-shelf elastomers that are not easily customizable.

While these fabrication methods and materials may be successful for producing a prototype idea for a research paper, the manufacturing leaves too much room for human error (damage due to difficult mandrel removal, uneven part thickness due to misalignment of wax cores, improperly adhered /misaligned seams due to the difficulty of aligning several soft parts). The material choices also limit what types of functionalities are possible for soft robots. The critical research question then becomes – ***how* can soft robots be made in a more controlled, more predictable**

**way? *How* do soft materials behave and *how* can they be processed into a desired form?** This is a complex problem that requires the skills of a materials science researcher *and* the skills of a roboticist.

More types of manufacturing methods and material control are needed to overcome these fabrication limitations. For manufacturing methods, there are several existing technologies that can be implemented. One of the most promising categories is additive manufacturing. Instead of molding or laminating the robot(s) pieces and then assembling those pieces, the robot can be created with a printer in smaller increments such as extruded filaments, droplets, or thin layers. These smaller increments can be built up in 3D space into a full robot or robot component. Many additive manufacturing processes can also potentially be used with soft materials to create models very similar in quality to those created with molding. Soft robot materials often begin in a liquid state and so can be used in existing 3D printers with slight modifications to the material deposition system. Mechanical equipment on 3d printers is also precise enough so that printed part resolution can compete with a molded result. However, the materials used in additive manufacturing systems need to be optimized for different conditions than those used with molding or 2D lamination. 3D printing is inherently related to material chemistry and fluid material properties like viscoelasticity, viscosity, and yield stress because fluid is flowing through pipes, nozzles, and on top of and/or within other fluids. Tracking these parameters is important for print success. To achieve a higher level of control of material properties such as ultimate tensile strength, toughness, or even degradability in soft robots, more

custom materials must be synthesized within soft robotics research. This requires study into polymer synthesis, reactive polymer chemistries, and many types of material characterization of both fluids and solids. To combine the synthesis of a custom designed material with a custom additive manufacturing process would be the ultimate goal when striving for a higher level of control in soft robot behavior. However, there are many development steps needed in between the current state of soft robotics research and this idealized goal.

An important aspect of soft robot manufacturing is that robots and their components are often made of multiple materials. Similar to hard robotics, soft roboticists want their robots to think, sense and act (or at least two out of the three). This means that several different materials can be included into a soft robot or soft robot part. For example, a soft roboticist would like to make a curling actuator for grasping that senses both the strain in the compliant actuator skin (to predict motion) as well as the pressure when an object is grasped (to ensure safety). The actuator already requires multiple materials to achieve this goal, including some strain limitation via material patterning or inclusion of a strain limiting fabric in the actuator, and a conductor that can stretch with the actuator and change resistance as the object is squeezed. Even when discussing relatively simple robotics concepts like this one (sense and act), the question of ***how*** this can be produced in a repeatable way makes for a challenging problem. Each material (elastomer, fabric, conductive fluid) may have a different modulus, reactivity, ultimate strain, strength and state (solid, liquid). To additively manufacture these materials together requires multiple separate material behavior

analyses, one set for how these materials will be automatically printed into the desired form, one set for each material in its current and deformed state, and one set for the combined material characterization of the composite(s). Ultimately, a soft roboticist must know how to properly synthesize and/or characterize these materials to predict the behavior of the materials before, during, and after processing through an additive manufacturing system.

The main categories of components that are needed for soft robotics are very similar to hard robotics. These include: actuators (*11*), wires (*12*), sensors (*13*), circuits (*14*), and power supplies (pneumatic, hydraulic, chemical reaction, battery, etc.) (*15*, *16*). Additive manufacturing has already been used to create some of these components (Figure 2). Circuit boards have recently been fabricated out of soft materials (*17*, *18*) but are not commonly made exclusively with additive manufacturing. However, each of these components have the potential to be created via additive manufacturing as a standalone entity or into a combined robot structure. One reason for combining these materials into one process is the desire for robot autonomy, which is common in hard robotics. Soft robots are often tethered to pneumatic or hydraulic systems, and multi-component additive manufacturing has potential to remove this tether via automated inclusion of pumps and power sources.

In order to achieve both the ability to additively manufacture soft robots, and to increase the level of material control via customization, materials science knowledge is required. Material synthesis and processing for additive manufacturing is a gap in

the field that needs more research to produce better soft robots. This thesis addresses that gap by introducing methods to better incorporate additive manufacturing into soft robotics with the augmentation of materials science knowledge and testing methods.

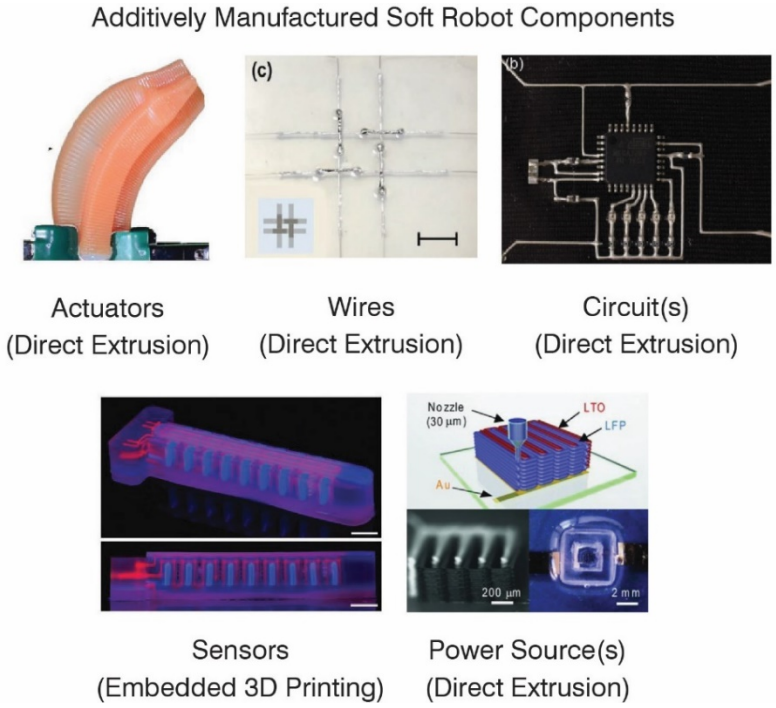


**Figure 2.** Each part of a soft robot has the potential to be additively manufactured. Additive manufacturing for soft robotics can include: actuators (*11*), wires (*12*), circuits (*14*), sensors (*13*), and power supplies (*16*). With proper materials characterization and process development, more complex components can be fabricated without human intervention.

## 1.1
## Additive Manufacturing for Soft Robotics, a Review

It is important to reiterate that additive manufacturing in soft robotics is not yet a common occurrence, and that non-automated methods still dominate the literature. Science Robotics released a review about the grand challenges of robotics this year. They noted that one of the grand challenges in robotics is the development of new materials and manufacturing methods for robot technologies, specifically with regard to soft materials. They outline that this challenge encompasses both the need for increased available materials for soft robot functionalities as well as the need for fabrication methods that include both 3D printing and multi-process methods. They cite a common complaint about soft robotics research – that many of the robots created are one-offs that in the current state cannot be widely adopted (*19*). The desire for new materials and manufacturing methods for those materials stems from the goal of creating soft robots that function outside of the research lab and that can be produced at large scales.

The examples described below include the state of the art of additive manufacturing for soft robotics as well as relevant additive manufacturing processes and material systems that can be applied to soft robotics. These additive manufacturing methods are some of the best solutions to approach the soft robot material and fabrication problem. The important question is how can these methods come together to produce

soft robots in a repeatable and high-quality way, so soft robots can move out of the laboratory?

From extrusion-based 3D printing to photopolymerization 3D printing, there are many options for the soft roboticist when beginning to develop an additively manufactured prototype. The state of the art in additive manufacturing for soft robotics and soft materials as of this writing is a spread of both the improvement of additive manufacturing technologies that can be used for soft robotics and the application of existing additive manufacturing techniques to create novel robots. Current research in soft robotics is just starting to reach into the additive manufacturing possibilities of polymers and conductive materials with appropriate material properties for soft devices. Other additive manufacturing methods that have not been specifically developed for soft robotics also give valuable insights for soft robotics production, and so these are included in this review. Robots can potentially be created via one 3D printer or several machines in an assembly line. Both the study of individual material behavior(s) and composite material behavior(s) are important for improving soft robotics manufacturing, so examples of both individual and multi-material 3d printing of (mostly) soft materials are included in this section.

### 1.1.1 Extrusion-Based Additive Manufacturing

Extrusion methods involve the 3D printing of an uncured fluid through a nozzle either directly onto the build plate or into a supportive reservoir. In soft robotics, these are often elastomeric fluids or materials that are flexible after curing. The main categories

for extrusion-based additive manufacturing in soft robotics are (1) direct extrusion, (2) reservoir bath printing, and (3) embedded 3D printing. Each use extrusion techniques in a different way.

Direct extrusion is very similar to thermoplastic extrusion in the way that 3D prints are built via filaments layer by layer, except that the extruded filament source is a fluid pushed through a nozzle. Fluids can be extruded via syringe pump, piston, or air pressure. Direct extrusion has been performed with single materials (Figure 3) such as silicone (*11*, *20*, *21*), liquid metals (*12*, *22*, *23*), silver nanoparticle inks (*14*, *24–26*), hydrogels (*27–29*), and graphene oxide (*30*) and lithium ion chemistries (*16*) for batteries. Direct extrusion has also been performed with multi-material systems (Figure 4) like two silicones (*31*), silicone or epoxy with additives (*32*), multiple hydrogels (*33–38*), deposition of hydrogel and polymer melts (*39*, *40*), polyurethane acrylates with magnetic particles (*41*), and battery materials (*42*). The above examples use different strategies of extruder design in order to facilitate multi-material printing. These strategies include: the use of microfluidics to quickly switch between 2 silicone lines (*31*) or extrude multiple hydrogel lines at once (*38*), active mixing of reactive silicone or epoxy with additives to vary material properties (*32*), and collecting several fluid lines and extruding chosen fluids by rapidly starting and stopping the flow of the polymer (*37*).

The ability to print with multiple materials in the same extrusion system is important because soft roboticists can create a robot with customized actuation or sensing

behavior within the same printing system. Being able to design the material chemistry and control the extruded material's properties is also important for predictable and customizable soft robot behavior. This will be discussed further in Section 1.3.

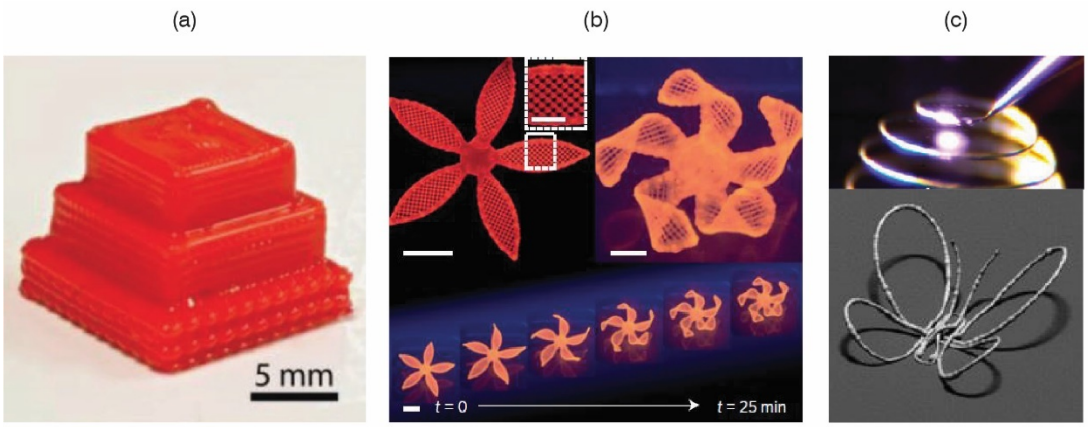


**Figure 3.** Direct extrusion has been performed with single materials such as (a) silicone (*21*), (b) hydrogels (*27*), and (c) liquid metals (*25*). Curing mechanisms include the application of heat, chemical reactions, and precise UV radiation. There are many functionalities produced using this method including variation of resolution and strain behavior within the same print (a), hydration actuation (b), and custom conductive springs (c), all of which are useful for soft robotics.

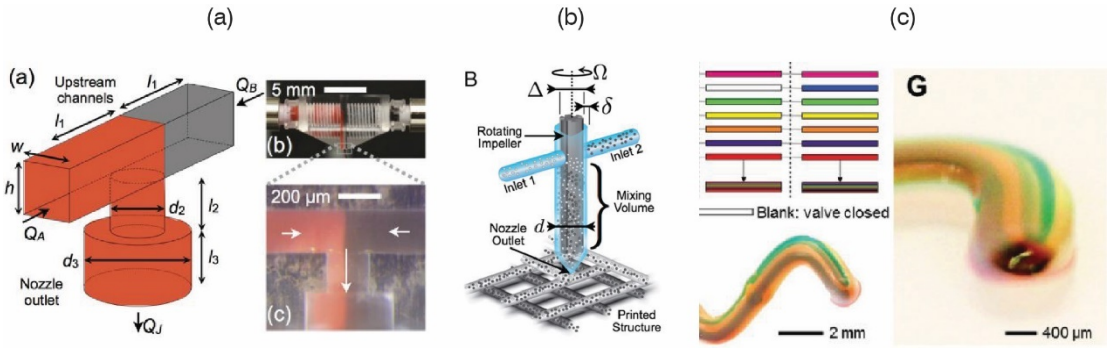


**Figure 4.** Direct extrusion of multiple materials has been performed with microfluidic extrusion heads and multiple silicones (*31*), mixing extrusion heads with silicone, epoxy, and additives (*32*), and controlled collected extrusion of multiple hydrogels (*37*). These strategies facilitate printing of many materials within the same system, which is useful when designing a soft robot with varying properties in the same component.

Reservoir bath printing uses a system similar to direct extrusion except that the material is extruded into a supportive fluid reservoir. Reservoir printing has been performed with silicones and hydrogels in a granular gel medium (*43*), silicone elastomers in an organogel support medium (*44*), PDMS in a hydrophilic Carbopol support bath (*45*) (Figure 5), and hydrogel inks in a hydrogel support bath (*46*, *47*). The reservoir helps support the extruded fluid which allows lower viscosity liquids to be patterned that would not hold their shape during direct extrusion. The printed part can be later taken out of the bath and cleaned to remove the reservoir material.

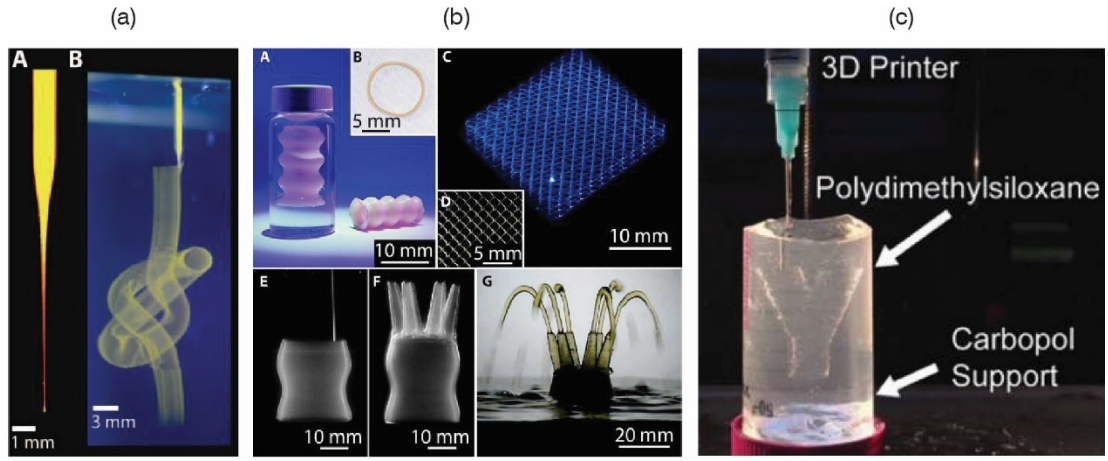


**Figure 5.** Reservoir printing has been performed with silicones and hydrogels in a granular gel medium (*43*), silicone elastomers into an organogel support medium (*44*), and printing PDMS into a hydrophilic Carbopol support bath (*45*). The reservoir bath provides support for low viscosity extruded fluids before curing. After curing, the part is taken from the bath and cleaned to remove support material.

The reservoir bath can also be used to cure the extruded fluid, with examples including polyelectrolyte inks in an alcohol coagulation reservoir (*48*), alginate filament in a calcium chloride reservoir (*49*), silicone catalyst in an uncured silicone bath (*50*) (Figure 6). Reservoir printing is which is especially applicable with low viscosity silicone materials, where diffusion between the reservoir bath material and the filament material is sufficient to fully cure the printed model without mixing (*50*). Very small filament diameters (1 µm) (*48*) and complex nested shapes (*43*) are possible with these methods.

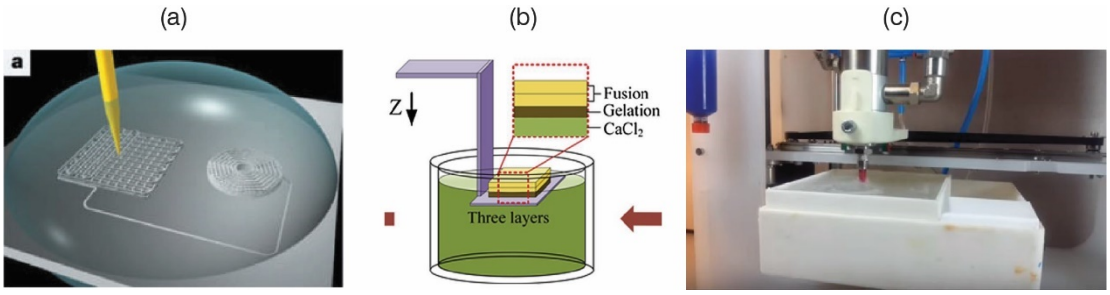


**Figure 6.** Reservoir fluids can also be used to cure the extruded polymer, with compositions such as (a) polyelectrolyte inks in an alcohol coagulation reservoir (*48*), (b) alginate filament in a calcium chloride reservoir (*49*), and (c) silicone catalyst in an uncured silicone bath (*50*).

Embedded 3D printing uses a similar concept to reservoir bath printing except that the reservoir bath itself makes up a portion of the model and is not meant to be removed from the printed part. Fugitive polymers can be included in the print and then heated to flow out and create a complex hollow space (*15*, *51*). Embedded 3D printing has been used with catalytic and fugitive inks inside a silicone matrix (*15*) for pneumatic actuation via gas-producing reactive chemistry, ionically conductive fluids inside a silicone matrix (*13*) for sensing and actuation, and a carbon-based ink inside a silicone matrix (*52*) for sensing (Figure 7). Silicone matrices can cure after printing at room temperature, or at increased temperatures for faster cure. Embedded 3D printing provides the same benefits as reservoir printing with the additional bonus of not having to clean the printed part after curing.

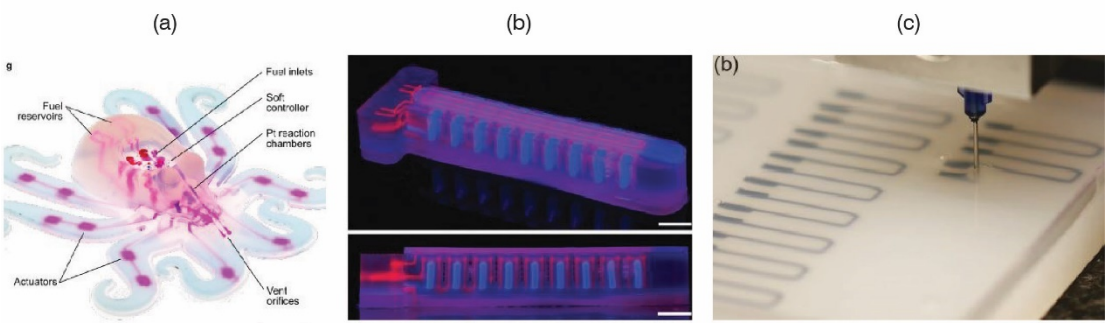


**Figure 7.** Embedded 3D printing has been used with catalytic and fugitive inks inside a silicone matrix (*15*), ionically conductive fluids inside a silicone matrix (*13*), and a carbon-based ink inside a silicone matrix (*52*). The support material is included as part of the final model, so there is no need to clean the part after curing unless the extruded material is a fugitive ink.

Some reservoir support 3D printing and embedded 3D printing research examples are detailed in Table 1. Both reservoir and embedded 3D printing are inherently multi-material processes. Whether the material is meant to serve a temporary or a permanent function, material interactions and complimentary material properties are important to determine. This will be discussed further in Section 1.3.

Table 1. Printing with reservoir support / embedded 3D printing

| Extruded Materials | Bath Materials | Purpose | Source | Year |
|---|---|---|---|---|
| • Concentrated polyelectrolyte inks (poly(acrylic acid), poly(ethylenimine), poly(allylamine hydrochloride))/water | • isopropanol/water<br>• ethanol/water | Mask-less microperiodic structures (tissue engineering, microfluidics, etc.) | (*48*) | 2004 |

| | | | | |
|---|---|---|---|---|
| • carbon<br>• conductive grease | • Ecoflex 00-30 / Slo-Jo / Thi-Vex / Silicone Thinner | Strain sensors inside elastomers (embedded method) | (*52*) | 2014 |
| • photocrosslinkable polyvinyl alcohol / fluorescent polystyrene microspheres<br>• Sylgard 184 / Fluorescent polystyrene microspheres | • Carbopol ETD 2020 /water / NaOH<br>• Irgacure photoinitiator / Carbopol<br>• cell growth media /Carbopol<br>• Dow Corning 9041 / silicone oil | General reservoir printing technique improvement (tissue engineering, electronics, smart materials, etc.) | (*43*) | 2015 |
| • Platinum catalyst solution | • unpolymerized silicone bath | Picsima sub-surface catalyzation printing (commercial product) | (*50*) | 2016 |
| • Sylgard 184 | • Carbopol | General reservoir printing technique improvement | (*45*) | 2016 |
| • Pluronic F127 / water<br>• Pluronic (F127-DA) / Irgacure 2959 / water / PEG-DA, Pt Black | • Sylgard 184 and SE 1700<br>• Ecoflex 00-30 / Slo-Jo / Thi-Vex | Soft, autonomous robots (embedded method) | (*15*) | 2016 |
| • Momentive UV Electro 225 / silicone oil<br>• Smooth-On Mold Max 10<br>• vinyl-terminated PDMS base (GelestDMS-V31) / (mercaptopropyl)methylsiloxane)]-dimethylsiloxane copolymer cross-linker (Gelest SMS-022) / 2,2-dimethoxy-2-phenylacetophenone photoinitiator / ethanol / fluorescent microspheres | • polystyrene (KRATON G1702) / polystyrene (KRATON G1650) / light mineral oil | Reservoir printing process improvement for materials like silicone | (*44*) | 2017 |
| • Aerosil 380 fumed silica / EMIM-ES<br>• Pluronic F127/ water | • Ecoflex 00–10 / Slo-Jo /Thi-Vex<br>• SortaClear 40 / Slo-Jo / Thi-Vex | Somatosensitive actuators (embedded method) | (*53*) | 2018 |

| | | | | |
|---|---|---|---|---|
| | • Ecoflex 00–30 / Slo-Jo / Thi-Vex | | | |

Currently the most relevant extrusion-based methods in soft robotics revolve around PDMS. Silicone is the most popular material family in soft robotics due to available simple two-part chemistries, their favorable processing conditions (pour, mix, and mold), and their favorable material properties (high deformation, strength, and inertness). Silicone materials suitable for soft robotics are ready available via commercial silicone kits like Sylgard 184 (Dow Chemical) (*54*), SE 1700 (Dow Chemical) (*55*), and Ecoflex / Dragon Skin (Smooth-On) (*56*).

Based on the success of silicone as a molded and laminated material in soft robotics, it is logical that the most popular material family should be developed for additive manufacturing. Silicone 3D printing has been commercially developed using extrusion-based or jetting methods (*50*, *57–60*), but several academic works use silicone printing as a means to produce soft robots or soft devices. Research into silicone printing, for both soft robotics and other relevant fields, is listed in Table 1. Silicone can either function as a directly extruded material or as a reservoir bath material. Silicone materials are versatile and 1-part RTV systems (*61*), 2-part cure systems (*11*, *20*, *31*, *32*, *34*, *62–65*), and mixtures either with another silicone or other polymer (*21*, *66–68*) have been printed. Silicone has also been used in drop on demand and jetting methods but these are less common in soft robotics (*60*, *69*). Material characterization like rheology is integral for printing high quality silicone parts for soft robotics, as discussed in Section 1.3.

Table 2. Silicone 3D Printing Research in Extrusion Additive Manufacturing and/or Soft Robotics

| Materials | Purpose | Source | Year |
|---|---|---|---|
| • GE Silicone II household silicone RTV sealant<br>• 3M DP460NS 2-part epoxy<br>• SS-26F 1-part, silver-filled RTV silicone | 3D printing devices with conductive silicone, Fab@Home | (*70*) | 2007 |
| • 1-part RTV Silicone | Fab@Home printing system | (*61*) | 2009 |
| • Dow Corning 732 Silicone (1 part RTV)<br>• Ecoflex 00-50 (2-part RTV)<br>• Wax | Silicone/wax actuators | (*62*) | 2014 |
| • SE 1700 with fluorophore dyes<br>• Pluronic F127 in deionized, ultrafiltrated water<br>• pure or cell-laden GelMA solutions | Tissue constructs | (*34*) | 2014 |
| • 2-part silicone | structur3D printing system (commercial product) | (*59*) | 2014 |
| • SE 1700, anhydrous hexanes, silicone oil | Microfludic printing, multimaterial switching | (*31*) | 2015 |
| • water/glycerol<br>• aqueous polymer lubricant<br>• Pluronic F-127 (Sigma-Aldrich) / deionized water/ molecular tracer dye<br>• SE 1700 / polystyrene tracer particles<br>• EPON 828 (Momentive), TS-720 fumed silica / blue epoxy pigment / Epikure / TS-720 fumed silica<br>• silver ink<br>• conductive carbon black powder / sodium hydroxide /aqueous hydroxyethyl cellulose | Active mixing in extrusion system | (*32*) | 2015 |
| • sodium chloride / glycerol / PEG 1500<br>• Dragonskin 10 Slow / Thi-Vex / Slo-Jo | Extruding concentric fibers | (*63*) | 2015 |
| • SE-1700 / Sylgard 184<br>• Epoxy (Epon 828) filler | Multistable architected materials | (*64*) | 2015 |
| • Ecoflex 00-30 / aliphatic hydrocarbon solvent | Conformable printing onto balloon | (*65*) | 2015 |
| • WACKER Silicones | ACEO silicone 3D printing (commercial product) | (*60*) | 2016 |

| | | | |
|---|---|---|---|
| • Dextran/isopropanol<br>Elastollan 35A (TPU) / tetrahydrofuran:dimethylformamide<br>• Elastollan 35A/carbon black/tetrahydrofuran:dimethylformamide.<br>• silver flakes (5–8 μm) / versamid 973/pentanol<br>• SE1700 (Dow-Corning)<br>• SE1700 (Dow-Corning) /Sylgard 184 | Multi-material microphysiological devices | (*66*) | 2016 |
| • Dragon Skin 30 / SE 1700 | Controlling silicone filaments via deformation, instability, fracture | (*21*) | 2017 |
| • Ecoflex 00-30 / Urefil-11<br>• Dragon Skin 10 Very Fast / Thi-Vex | Direct extrusion fabrication of soft robot actuators | (*11*, *20*) | 2017, 2018 |
| • vinyl terminated poly(dimethylsiloxane)-co-(diphenylsiloxane) (PDMS-co-PDPS) / hexamethyldisilazane-treated (HMDZ) silica | Process improvement, tunable stiffness silicone | (*67*) | 2018 |
| • Proprietary silicone | German RepRap, 3D printing liquid silicone | (*71*) | 2017 |
| • Silicone polyurethane mixture | Carbon3D, combination of silicone and urethane | (*68*) | 2017 |

### 1.1.2 Photopolymerization Printing

Photopolymerization technologies provide 3D printing solutions for soft robotics due to their ability to produce high resolution architectures and multi-material models. The working principle of photopolymerization 3D printing revolves around the use of a UV light emitting device to cure a polymer during deposition. However, material limitations such as poor elastomeric cyclic behavior (*72*) and anisotropy issues (*73*) have limited their use. Photopolymerized structures useful for soft robotics have been created via PolyJet (jetting of droplets similar to inkjet) (*74–79*) because of its ability to create high resolution multi-material elastomeric architectures, and projection stereolithography (projected UV light area) (*72*, *80–83*) because of the new

developments in chemistry that improve the material quality of the photopolymer elastomers. These improved material qualities help achieve desired soft robot mechanical properties like high elongation and repeatable deformation (Figure 8).

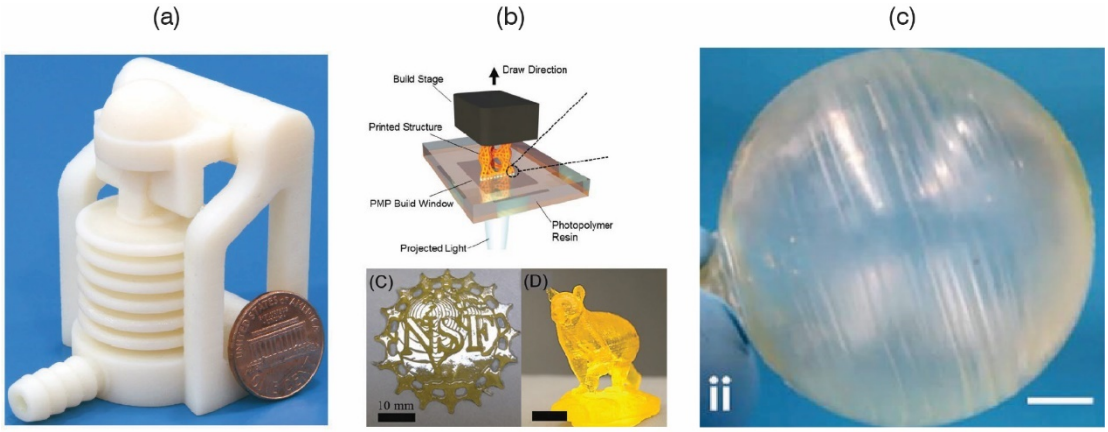


**Figure 8.** Photopolymerization related to soft robotics has mainly centered around (a) PolyJet and (b,c) projection stereolithography. (a) PolyJet also allows for multi-material printing with hard and soft polymers (*78*). The improvement of chemistries to include those that (b) self heal (*72*) and (c) have high elongation abilities (*82*) makes photopolymerization processes more promising for soft robotics.

PolyJet-produced materials have played an integral part in several soft robotics research works, including soft actuators for unstructured terrain (*75*), creating hard/soft composite grippers (*76*), creating graded structures in a robot body (*77*), making actuators with an embedded hydraulic fluid (*78*), and creating shape memory actuators (*84–87*). The commercially available PolyJet printing system by Stratasys provides the ability to print and blend together multiple materials in high resolution,

in ranges like 26 shore A elastomer (Tango) to rigid plastic (Vero) (*88*, *89*). Methods such as digital light projection have been used with improved photopolymer chemistries that self heal (*72*), have high elongations (*82*), and have tough and resilient hydrogel chemistry (*83*) more ideal for soft robotics. Improved chemistries, processing conditions, and material qualities are needed to make photopolymerization more widespread in soft robotics. Discussion of these needs is addressed later in this work. Table 4 outlines some of the previously discussed photopolymerization methods used to print soft robots and elastomeric structures.

Table 3. Photopolymerization processes in soft robotics

| Material | Method | Reason | Source | Year |
|---|---|---|---|---|
| • Tango Black Plus / VeroClear | PolyJet (Connex) | Navigating unstructured terrain | (*75*) | 2017 |
| • TangoPlus / VeroWhite | PolyJet (Connex) | ER fluid valve | (*74*) | 2018 |
| • TangoPlus / VeroClear | PolyJet (Connex) | Fish fin style gripper | (*76*) | 2016 |
| • TangoPlus FLX930 / VeroWhitePlus RGD835 | PolyJet (Connex) | Graded material properties in robot body | (*77*) | 2015 |
| • Model cleaning fluid / Rigur (RGD450)<br>• Polyethylene glycol / Tango Black 28 Shore A | PolyJet (Connex) | Hydraulic actuators for robotics | (*78*) | 2016 |
| • Elastomeric Precursor (EP; Spot-E resin) | Digital mask projection stereolithography (custom machine) | Antagonistic systems of artificial muscle for soft robotics | (*81*) | 2015 |
| • Benzyl methacrylate (BMA) / Poly (ethylene glycol) dimethacrylate (PEGDMA) / Bisphenol A ethoxylate dimethacrylate (BPA) / Di(ethylene glycol) dimethacrylate (DEGDMA) | High resolution projection microstereolithography (2 bath) | Multi-material shape memory polymer architectures | (*80*) | 2016 |
| • AUD (Ebecryl 8413, Allnex) and EAA (Ebecryl 113, Allnex) / TPO | Digital light processing | Elongation improvement for UV curable elastomers | (*82*) | 2017 |

| | | | | |
|---|---|---|---|---|
| • Vinyl terminated PDMS (V.S.) / • (mercaptopropyl)methylsiloxane]-dimethylsiloxane (M.S.) / (mercaptopropyl)methylsiloxane]-dimethylsiloxane • (M.S.) / diphenyl (2,4,6-trimethylbenzoyl)phosphine oxide / toluene | Click chemistry / stereolithography (open source SLA printer, projection) | PDMS-based UV curable polymer, soft robotics use, self-healing | (*72*) | 2017 |
| • acrylamide / [2-(Acryloyloxy)ethyl]trimethylammonium • chloride *N,N*2-methylenebisacrylamide • crosslinker / ionic, sulfonate-modified silica nanoparticles | Ember (Autodesk, Inc.) digital mask projection stereolithography | Printing hydrogels with improved toughness and resilience for applications like soft robotics | (*83*) | 2017 |

### 1.1.3 Multi-Component and Multi-Material Additive Manufacturing

Multi-material and multi-process printing research is the logical next step in additive manufacturing (*34*), with recent reviews focusing on the topic for both hard and soft systems (*90, 91*). Multi-material printing can be as varied as co-printed fluid and cured polymer for hydraulic actuation (*78*), inclusion of liquid metal circuits inside of silicone (*12*), co-printed conductive and thermoplastic urethane chemistry (*14*), or even placement of hard components (*14*). As soft robotics additive manufacturing develops, materials science of both the individual and composite soft components is needed. Their ability to interface with non-elastomeric or hard components will also need more study. Both of these needs can be addressed via existing materials science characterization techniques.

## 1.3
## Materials Science Techniques for Soft Robotics

Fluid extrusion and UV curing methods have both been used with varying levels of success when making soft robots. Direct extrusion methods allow for many different types of material chemistries to be included in soft robot additive manufacturing, all the way from hydrogels to rubbers to ceramic composites to liquid metals. UV curing methods have the ability to produce high resolution components but are more difficult to integrate with multiple material systems. Lessons learned from individual manufacturing methods can be combined to create better single material systems as well as multi-material printing solutions. Regardless of additive manufacturing type, material property knowledge is required for both fluids and solids. The next few sections briefly explain some relevant material properties and characterization techniques.

Soft robots created via additive manufacturing depend heavily on the type and quality of their respective materials for performance. Material properties limit or extend elongation, enhance or reduce compliance, strengthen or weaken adhesion, and can also make additive manufacturing elegantly simple or incredibly frustrating. Knowledge and characterization of such materials clarify which methods of manufacturing and equipment are appropriate as well as, with some exploration, give ways to improve the chemistry for easier flow, more controlled curing, higher elongation, and even improved conductivity.

The types of materials in the above styles of additive manufacturing are only a fraction of the possible options that could be available to soft roboticists in the near future. However, the characterization methods available to soft roboticists to improve their understanding of their current working materials are usually readily available and well-known. Understanding these characterization methods and their ultimate results will streamline additive manufacturing and material customization processes to improve the quality of the resulting devices. Before being able to build a printer for example, material properties should be known. Properties like curing kinetics, viscosity, yield stress, and interface interactions will directly translate to required power and size of mechanical equipment, as well as achievable extrusion speeds and resolution. Material characterization will also help determine if the fluid will even hold enough weight to make a 3D structure.

### 1.3.1 Polymer Chemistry

Soft roboticists are often dealing with a large range of polymeric fluids when fabricating soft components. These polymers may have properties that change depending on time after mixing, processing temperature, solvent evaporation, and interaction with high shear regions in equipment. The additive manufacturing of these materials may also depend on how the material is synthesized. So, polymer chemistry knowledge is important to obtain to understand what kinds of reactions are possible before, during, and after material use. Knowledge of general polymer material properties such as molecular weight, curing mechanisms, crosslinking density,

sensitivity to UV radiation, and self-diffusion are only some of the many aspects of material design and processing for 3d printing (*29*, *36*). Increasing the polymer chain length and/or decreasing the amount of crosslinks can increase the elongation percent before break of the final material. Proprietary polymers make this difficult to change, as there may be no control over changing the chain length or degree of crosslinking, but for synthesizing custom polymers this is another means of optimizing mechanical behavior.

Soft robotics relies heavily on commercially available polymers in order to make robot bodies. Typical commercially available silicones used in soft robotics literature include the vinyl-terminated PDMS Sylgard 184 (Dow Corning) (*92*), SE 1700 (Dow Corning) (*55*), and the family of platinum-cure silicones available from Smooth-On (*56*). Mixtures of Sylgard 184 and SE 1700 have also been used to tune extrusion behavior (*64*). Several facts are known about these polymers. Each of these silicones have similar reaction chemistries instigated by a catalyst (in which no byproduct is produced) (*54*), they have recommended mixing ratios to ensure proper curing, and their curing is accelerated by the application of heat. Even though their exact formulations may be proprietary, curing kinetics characterization can be performed at various temperatures to determine a model for reaction progression. If more control of polymer chemistry is desired due to increased customization needs or novel functionalities, elastomeric polymer(s) can be synthesized. Research like that presented in Chapter 2 of this thesis proposes that making custom materials for soft robotics can give a higher level of control of the material properties of the resulting

robot. But, this requires knowledge of how the polymer properties drive the synthesis, the processing, and the ultimate mechanical properties of the robot.

Chemical characterization of polymers can provide insight into their synthesis or processing results. Some useful techniques include: Fourier transform infrared spectroscopy (FTIR), which gives the molecular fingerprint of the material via elucidation of chemical structures (*93*), $^{1}H$ and/or $^{13}C$ nuclear magnetic resonance spectroscopy (NMR), which gives insight into the types of molecular structure(s) present in the material, and crosslink density characterization, which estimates the number of crosslinked points per volume of networked polymer. For soft robotics, choices can be made via chemistry that affect biodegradability, expected elongation, expected tensile strength, and flexibility of the elastomeric material. The chemical synthesis of custom polymers does require extra expertise focused in chemistry lab work, but the interdisciplinary nature of soft robotics makes the incorporation of custom polymer syntheses possible.

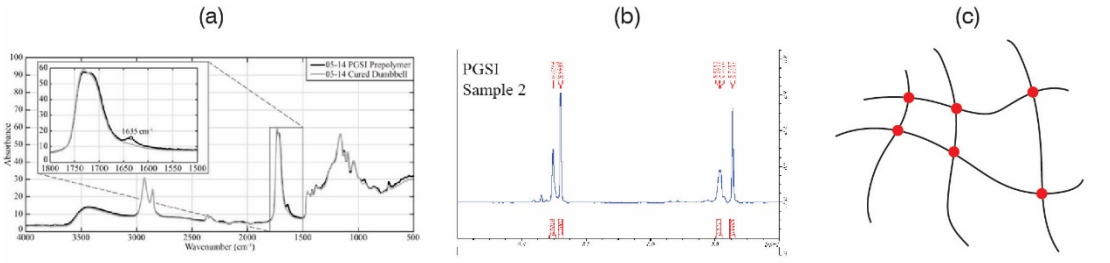


**Figure 9.** Chemical testing of polymers is useful for identifying (a) a molecular fingerprint of the material (FTIR) (results from (*94*)), (b) types of molecular structures present in the material (NMR) (results from (*94*)), and (c) amount of crosslinks in the material (if applicable) (crosslink density). These properties affect synthesis conditions of the materials, their processing in additive manufacturing systems, and their final material properties.

### 1.3.2 Kinetics of Reactive Systems

The speed and state of cure in reactive chemistries are directly related to the material's mechanical structure and processability in an additive manufacturing system. When working with transient materials that cure during extrusion, the closer a 3D printable fluid is to its final cure state, the more likely it is going to be partially crosslinked, stiffer, and harder to extrude. Papers written about the extrusion of silicone elastomers, especially those using products from Smooth-On, note the use of a cure retarding additive to slow the polymerization reaction and make the silicone printable for a longer period of time (*21*, *63*). However, by characterizing and monitoring how the reaction progresses, one can quantify cure time versus

temperature and then use these transient properties as an advantage. The curing kinetics can then be correlated to fluid structure via rheological testing.

Analysis of curing kinetics for heat curing polymers like silicone is performed with differential scanning calorimetry (DSC). DSC measures the differential amount of heat flow needed to heat the sample polymer at the same rate as an empty reference sample. Small amounts of sample can be isothermally held at a temperature and/or dynamically heated until they display an exothermic jump in the heat data signifying chemical bonding (curing). Heat flow can be directly correlated to the amount of chemical bonding occurring in the sample, assuming that each chemical bond releases the same amount of energy (*95*). Dynamic heating at rates of 1- 10 K/min gives data that can be used to calculate the activation energy of the reaction (*96*). Isothermal measurement of heat flow coming from samples as they cure can give extent of reaction and total heat of reaction (*97*, *98*). Depending on the type of reaction in the fluid, different DSC procedures may be necessary (*99*). The resulting data can be directly turned into cure rate and cure percent data based on time and temperature (Figure 10).

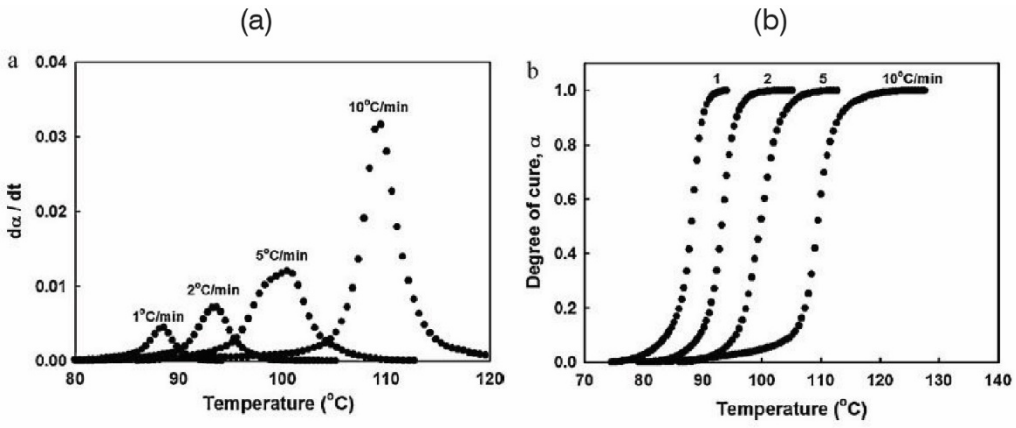


**Figure 10.** Cure rate and degree of cure data in a silicone rubber. Data example from (*95*). This type of data is useful when 3D printing with reactive chemistries to pair with rheology and ensure that the material is not too cured to extrude.

DSC fitted with a UV lamp (photo-DSC) can be used to analyze the curing kinetics of photopolymers (*100*). For photopolymerization systems, several parameters that inform the curing kinetics are considered and include: light intensity, layer thickness, layer area, the photoinitiator efficiency, and concentration of the photoinitator (*101–103*). Amount of inhibiting species such as oxygen also affect curing reactions. Another characterization technique for UV curing chemistries is real time infrared spectroscopy (RTIR) which monitors the conversion versus time in the curing polymer (*104*).

Curing kinetics data can be further combined with the rheology of the fluid to bound the printable time of the fluid by cure percent and fluid structure.

### 1.3.3 Fluid Rheology

Characterization of rheological properties of the flowing soft material (how it deforms under stress) is very important for understanding how the fluid will behave in a printing system. Rheological characterization is integral to both extrusion-based additive manufacturing and photopolymerization additive manufacturing research. Common tools for rheological testing are rotational rheometers and viscometers, but capillary rheometers have also been used in extrusion-based printing literature to measure rheological behaviors at high shear rates (*31*). Several parameters can be tested in order to determine printability of fluid and/or reservoir materials, but the most important include viscoelastic moduli (G"/G'), viscosity, and yield stress. Another consideration can be using fluids of similar densities and chosen polarities help prevent the collapse of the printed structure (*105, 106*). For photopolymerization systems, rheology is especially important for print success due to the use of high resolution inkjet nozzles (PolyJet) and movement of the model in a resin bed (*72*).

#### 1.3.3.1 Viscoelasticity

Viscoelastic behavior is important to characterize when printing materials with transient material properties. During extrusion, the material ideally should behave more like a fluid to readily flow through nozzles, and after extrusion it should behave more like a solid to retain printed structure. Viscoelasticity is described via the elastic modulus (G') and the loss modulus (G"). The G' is a measure of the amount of energy stored in the material (solid-like behavior), and G" is a measure of the ability of the

polymer to dissipate energy via heat (liquid-like behavior) (*107*). It is rare that a material will be entirely elastic or entirely viscous, and so many materials are considered to be viscoelastic.

G" and G' behavior in response to strain amplitude can be determined via a strain sweep test on a rotational rheometer (*108*). A higher dependence of G' on oscillation frequency during a frequency sweep test also indicates a more fluid-like material (*108*). Tan δ, also called the loss tangent, is the ratio G"/ G' and describes the amount of relative energy dissipation in the sample (*107*). Determining whether or not the ratio is below or above 1 at any given time and temperature gives information as to the state of solid-like behavior of the system (as opposed to liquid-like behavior). The point at which the ratio rapidly decreases during a curing/solidification process, for example, can be used to determine the point at which the fluid is no longer printable (the fluid is too solid-like). Tan δ can be determined via dynamic oscillatory shear experiments on a rotational rheometer. The gel point of a curing polymer can also be estimated by noting where G′ and G" crossover during a time sweep (*109*). Reaching the gel point is to be avoided if the material is being extruded.

A high G′ is an important parameter for keeping filament shape after extrusion, ensuring adequate spanning length, and maintaining the supportive structure of a reservoir bath (*51*, *52*, *106*). If the G′ is too low in the extruded fluid, a support bath is needed (*45*). Phase change induced G′ decrease has also been used to remove temporary inks and make a hollow structure inside an elastomeric print.

Recovery testing has also been performed for a sensor ink by cycling a sample at frequencies and strains seen in the final device, and then noting the change in G′ over time (*52*). Tests for thixotropy (time dependent change in viscosity) for a silicone reservoir material have also been performed using G′ recovery and tan δ ratio variation in order to estimate the time of recovery after nozzle disturbance (*53*, *110*). Under varying strain conditions, a modulus that can rapidly recover from a fluid-like state to a solid-like state is also desired for a reservoir bath so that it can heal from the cut path of the nozzle (*46*). Change in viscoelastic parameters over time is a useful technique in curing additive manufacturing systems and printers that use reservoir support (Figure 11).

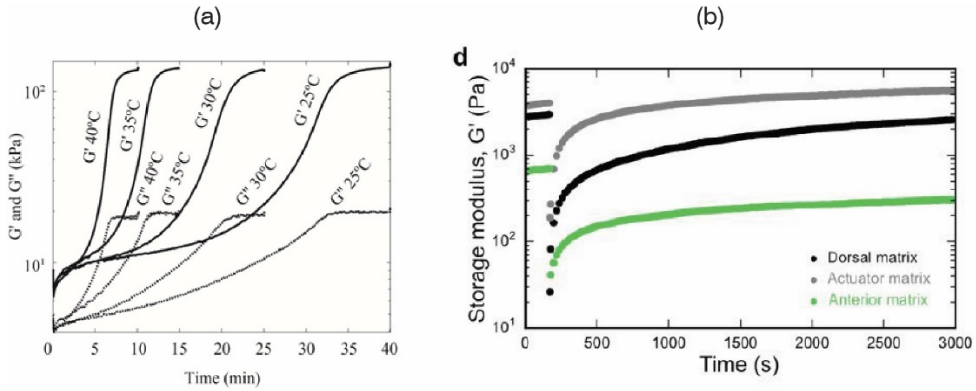


**Figure 11.** (a) G′ and G" data can be used to estimate the appropriate temperature range for a printing system utilizing reactive polymers during extrusion. Tan δ, the ratio of G" / G′, can be calculated to ensure that the elastic behavior of the extruded fluid is not outpacing the viscous behavior (signaling an acceleration of cure) to prevent clogging (*111*). (b) Testing of G′ recovery after disturbance is especially valuable to investigate the recovery ability of a reservoir bath after being disturbed by an extrusion nozzle in embedded 3d printing (example data from (*53*)).

Photorheology is performed via a rotational rheometer with a UV translucent window and UV light source, and other additions such as IR readings have recently been added to the same system to retrieve polymer composition data (*112*). This method can be used to gather G′ and G" for photopolymers during steady state oscillatory shear experiments as part of the determination of curing behavior (*72*, *83*). However, due to the very fast rate of curing in some photopolymers like acrylates, this technique has previously been limited by data acquisition speed (*113*).

1.3.3.2 Viscosity

Viscosity of the fluid, particularly in the transient case, is important to know at all points of the extrusion system, as viscosity is resistance to flow. Viscosity can be tested via a rotational rheometer or a viscometer. The simplest explanation of viscosity is a sort of internal friction in the fluid as it is stressed. When designing materials for extrusion processes, a lower viscosity is desired when the fluid is moving through a tiny nozzle (*52*). However, too low of a viscosity means that the fluid will have insufficient structure to pattern into a 3D shape without the use of a support bath. (*45*).

Shear thinning describes the phenomenon of fluid viscosity decreasing with increasing shear rate. Many fluids naturally exhibit this behavior, which is a realignment of the molecular strands of a polymeric fluid under stress which decreases the internal friction between chains and lowers the viscosity. The lower the

viscosity of the fluid as it moves through the extrusion nozzle, the less pressure needs to be applied by any pumps and motors up the line and the easier the fluid movement will be through small nozzles (*31*). Lower maximum shear stress fluids are more desirable extrusion systems because they require less force to extrude (*46*). Shear thinning additives, such as nanoclay, can be added to promote shear thinning behavior in materials where shear thinning is insufficient (*114*).

Viscosity should also be tracked if there is concern about a change in viscosity in the uncured polymers due to temperature increases before crosslinking (*35, 115*). High viscosity, similar to high G', is also going to limit how well an extrusion nozzle can move through a reservoir support bath. However, a higher viscosity reservoir fluid paired with a lower viscosity liquid (with chemically identical functionality) allows voids produced in the reservoir to be immediately filled by the extruded liquid (*51*).

Viscosity is also important to track for photopolymerization systems. Low viscosity is important in PolyJet processes because of the use of high resolution inkjet heads (*116*). The evolution of viscosity of a photopolymer during curing and its reliance on shear rate can be monitored via rheology (*83*). There can be low and high shear regimes when the model is pulled off of the bottom build plate and uncured resin flows to replace it (*81*). For photopolymerization processes like continuous liquid interface production (CLIP), viscosity determines the resin flow behavior when replenishing the area of uncured material below a print when it is being lifted out of

the bath (*117*). Evolution of complex viscosity can also be used to describe curing behavior in the polymer (*72*).

#### 1.3.3.3 Yield Stress

Yield stress is another important parameter to characterize in order to determine how much stress the fluid has to receive in order to flow. Yield stress behavior is a desirable property in direct extrusion methods due to the ability of the fluid to better hold a structure when disturbed (*21*). Yield stress can be determined via several methods, one being a stress ramp on a rotational rheometer to determine the stress value where the maximum viscosity occurs (*108*), and another as an estimation of the stress value during the crossover of G′ and G" during a stress sweep (*31*). Yield stress can also be found via a stress growth test, where yield stress is determined as a local maximum in the stress vs. time curve before the data plateaus (*118*).

In an extrusion-based system, yield stress applies both to the pumping mechanism(s) for the fluid as well as how well the fluid in the lower layers of the print can hold up successive polymer layers that are applied above it. Yield stress can be used advantageously in extrusion-based systems to prevent the flow of polymer until a critical stress is applied (*31*, *52*). In reservoir bath systems, a bath with too high of a yield stress will limit the motion of an extrusion needle through the reservoir. Before the yield stress is reached, the polymer try to return to its original state, and even make the delicate printed parts hard to remove from the bath (*45*). A low yield stress is needed to allow for movement of the needle through the reservoir (*51*). Yield stress

results relevant for curing reactive silicone and silicone for microfluidic extrusion are presented in Figure 12.

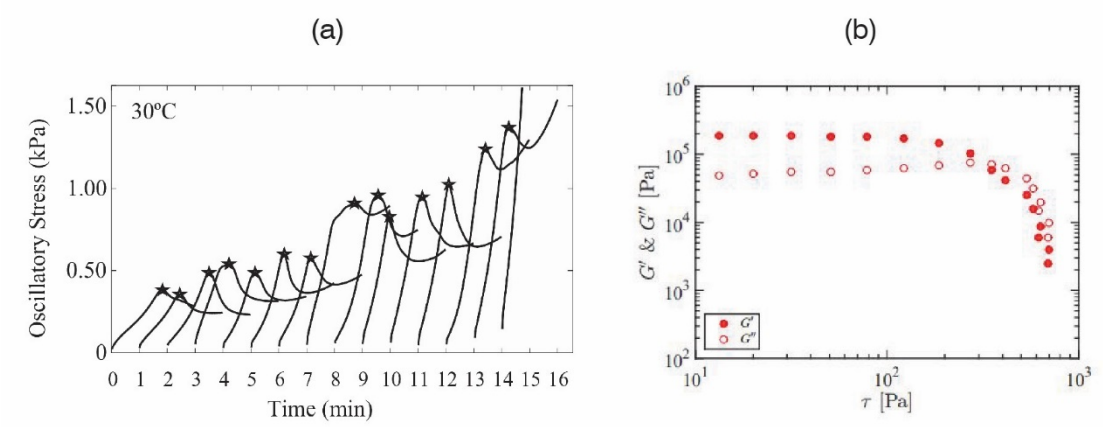


**Figure 12.** (a) Yield stress is an important parameter to track during curing processes in order to ensure that extruded structures will have enough stability after disturbance(s) (*111*). (b) Yield stress (estimated here as the stress at the elastic and viscous modulus crossover point) is also useful to know to prevent fluid from flowing out of a nozzle without sufficient pressure application (data example from (*31*)).

These three parameters certainly are not the only rheological descriptors that should be characterized, but they are some of the most relevant for extrusion-based printing systems. In mixing systems or systems where the polymer is curing as it is being printed, transience in all of these parameters is important to consider. Tan δ, viscosity, and yield stress may change with time and temperature as the curing or drying reaction progresses, and so characterizing these parameters within the desired operating time and temperature ranges is necessary.

### 1.3.4 Interfaces

Interfaces between soft components are important to consider when printing with multiple materials. During printing, the final strength of the print is tied to how much adhesion each layer has between the next. When the print is stretched, the ultimate tensile strength of the material may decrease with lower surface area contact or less adhesion between layers, so maximizing contact is important to improve strength. In thermoplastic systems, the melted polymer in the layer above can create good adhesion even if the previous layer has already fully cured (cooled). When using thermosets in extrusion systems, careful consideration is needed to ensure that the layered material can either still adhere after the previous layer is cured, or ensure that cure has not reached completion to allow uncured portions to fuse. When using photopolymers in stereolithography systems, good layer interfaces with minimal anisotropy are caused by controlled amounts of uncured portions of the previous layer attaching to the newly irradiated resin (*116*). However, interesting effects occur in photopolymerization systems due to overcuring when the light transfers past the newest printed layer and into the older section of the print. To avoid this, resins can be designed to have a low light penetration depth via increased photoinitiator concentration or inclusion of a dye (*119*).

When printing two or more different fluids, ensuring chemical compatibility of the extruded fluid and the bath can stop the formation of unwanted interfaces (*52*). Interfaces with chemically distinct materials like those between liquid metal and silicone, create difficulties due to the wide variation in chemistry between the liquid

metal oxide skin and the nearly inert, low energy silicone. Liquid metal structures are advantageously created using extrusion techniques because the oxide skin of the metal dominates the fluid structure once the ink is exposed to an oxygen environment. This skin helps stabilize extruded liquid metal ink droplets so 3D structures (*22*), thin upright wires (*23*), and 3D structures (*12*) can be printed. However, liquid metal is generally non-wetting on PDMS unless surface modifications with other chemicals (like gold) are needed (*22*). Wetting properties of one material onto the other can be tested via contact angle analysis. During this test, a droplet of one material is placed on the substrate and the angle the droplet makes with the surface is correlated to the amount of wetting between the two materials. A higher contact angle (less surface contact) means that the material has low wetting. High wetting surfaces have high surface energies and high interfacial tension, overcoming the fluid surface tension and keeping the materials close together (*120*).

Interfacing mechanically between hard and soft components is often required for soft robotics due to the need to incorporate anchors or hard circuits. The best method is when the two separate areas of material are printed so that there is a soft to hard gradient between them, taking advantage of similar material properties to reduce the stress concentration that would otherwise occur at a direct hard/soft interface (*77*). Gradient printing has been performed with higher-end machines like the Connex from Stratasys (*77*), but it is just as possible with lower end machines provided that the resolution is high enough and that multiple materials can be blended together. With extrusion-based 3D printing systems, chemical or structural grading is possible via in-

line liquid or particulate additives (*32*, *41*). Grading in photopolymerization systems (besides PolyJet) is possible by swapping reservoir baths during printing (*80*) or soaking selectively irradiated prints in solvent to remove unreacted monomers before a final cure step (*121*).

### 1.3.5 Final Mechanical Properties

The final mechanical properties of a 3D printed component are dependent on traits like chemical or physical crosslinking of the respective polymer(s), polymer chain length, and chemistry. Elastic modulus, ultimate tensile strength, and ultimate elongation percent are tied directly to quality of bond types between molecules, adhesion between printed layers, and polymer chain length. The most common materials characterization methods in soft robotics are split between the properties of the individual material(s) and the characterization of the component as a whole. There are common but not necessarily standardized methods for actuator characterization, such as the measurement of applied force when the actuator is held at one end and the other end is placed on a force measurement device (blocked force). Free extension, free contraction or bending is measured with the actuator freely moving in space during actuation, with or without a load attached (*53*, *81*, *122*, *123*). Otherwise, the application(s) of soft robot components can be so specific that testing methods revolve around the use case.

Materials testing of the cured polymers and films in soft robotics is much more standardized and allows for soft robot material behavior to be more comparable across use cases. Tensile testing of the materials themselves to failure gives information about the relationship of stress to strain of the polymer at any given time (*72*). These results help bound the operational regions of the component and provide predictive behavior estimates in the case of modeling or simulations. Tensile and compressive testing can be performed on larger samples a few inches in length on machines like the Instron, or on smaller scales of a few millimeters using a dynamic mechanical analysis (DMA) instrument (*49, 51*). When the sample is pulled to break, the ultimate tensile strength (the maximum stress value) and the maximum strain (the percent change in gauge length of the dumbbell shaped sample) can be determined if slippage of the samples in the grips is not occurring. Cyclic tests are also regularly performed to assess the material fatigue with repeated use. The engineering modulus (stress/strain) gives an idea of the stiffness of the polymer. The elastic modulus of the final polymer is important especially when additively manufacturing soft materials like PDMS, because the material may not be able to self-support its own weight even if the printing succeeds (*45*). The area between the loading and unloading curves (hysteresis) gives the amount of energy lost to heat via viscous behavior in the sample, which allows for efficiency of the component to be calculated for soft robot power requirements. Compression testing can be valuable but is not often used in soft robotics because many soft robots are functioning in a state of tension. Tensile and cyclic testing are also valuable for determining any anisotropy occurring in the additively manufactured part due to grain alignment of layers and extrusion paths.

Tensile testing methods can also be used to test behavior of composite samples, such as fabric and silicone, or conductive liquids and silicone paired with resistance measurements (*12*, *63*). This will reveal useful information like multiple moduli regions such as when a reinforcing layer breaks inside the silicone, or the sensing capabilities of the conductive fluid under varying elongation speeds (*63*). Tensile and cyclic testing for pure and composite 3d printed silicone is shown as an example in Figure 13.

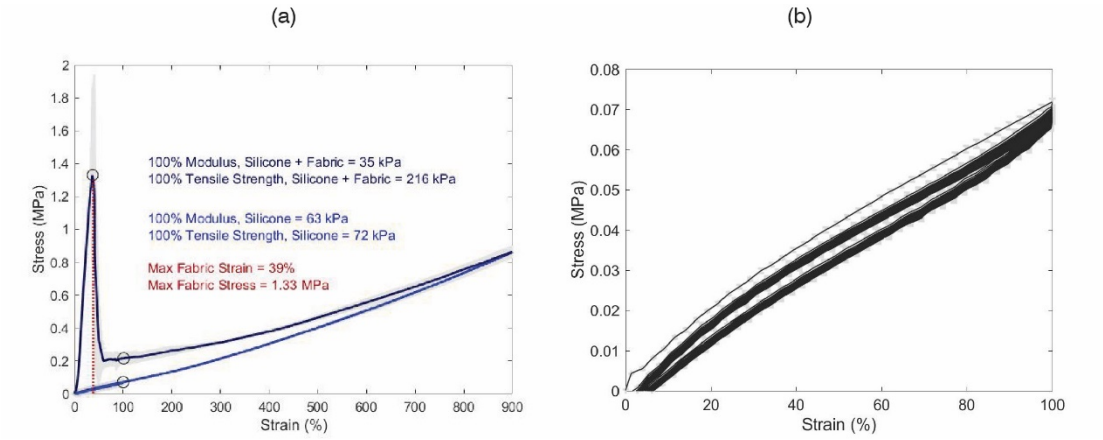


**Figure 13.** (a) Tensile testing is useful for determining the stiffness and ultimate elongation abilities of the materials. This is especially important when using composites, which can significantly change the behavior of the material (seen in the sharp uptick in modulus in the top line versus the smooth transition in the line below) (*124*). (b) Cyclic tensile testing gives information about material fatigue and hysteresis (example from author's unpublished data).

Final properties may vary depending on whether the fluid was printed or molded, so it may be useful to analyze samples from both methods for comparison. This process is especially important for PolyJet printed parts, which can have variations in elastic

modulus and fracture stress depending on the part's orientation on the build plate (*73*). Material properties may also change over time when undergoing repeated deformation, as seen in the Mullins effect in rubbers (*125*).

### 1.3.6 Dimensional Analysis of 3D Printed Parts

As long as the fluid(s) can be extruded through a nozzle, good interface adhesion is expected, diffusion between layers does not occur, and printing layer weight does not exceed the yield stress or the compression limit of the cured polymer there is a good chance of a successful print. Whether or not the printed fluid result exactly matches the expected dimensions of the model is a matter of post-print dimensional analysis of elements like line width, line height, cross-sectional area, and corner accuracy (*29*). G-code optimization to accommodate extrusion speed, volumetric flow rate, and acceleration capabilities of the equipment can be made based on that analysis.

## 1.4 Equipment Choices

### 1.4.1 Equipment for Extrusion Additive Manufacturing

Particularly relevant to this thesis is the use of active in-line mixing to create a 3D printing system capable of creating material gradients and extruding reactive chemistries (*11*, *20*, *32*). These mentioned works mainly focus on PDMS and epoxy formulations, but the concept is applicable for a variety of fluid extrusion systems.

Graded structures can be created via controlled mixing of additives via multiple fluid lines attached to the same extruder.

Additive manufacturing equipment in soft robotics runs the gamut from off-the-shelf commercial printers to completely custom-built printing systems. Typically, it is simplest to combine the two. Using a commercial three axis gantry with a custom extruder head is a common solution. The design for an extrusion system uses syringe needle tips, precision dispensing tips, or custom micron-size inner diameter glass tips to control the fluid's initial extruded filament size. Die swell, or the increase in filament diameter size upon extrusion, may make the filament size of the polymer larger than the inner diameter of the extruder needle. Combinations of multiple single-material extruder tips have been used in tandem to create multi-material prints by starting and stopping fluid flow in successive tips. In multi-material systems, the chambered area just before the nozzle can serve either as a mixer or collector of several fluid lines. In the collection case, the chamber extrudes a single filament composed of several stripes of distinct material (*37*). If the polymers are being mixed, the chamber and interior reamer geometry can be patterned to create enough turbulent flow so that the polymer becomes well-mixed before extrusion (*32*). Multi-material systems can incorporate passive or active mixing systems with each having their own respective advantages. Passive mixing systems don't require additional electronics hookups and power, and, depending on the chemistry of the extruded fluid, can be washed out or disposed of after use. Active mixing systems have been shown to decouple the flow rate of the fluid from the effectiveness of mixing using a more

compact design with an interior reamer. Multi-material print systems can also include vacuum nozzles that lift and place small discrete components such as chips or other electronics (*14*).

Flow control is also important for extrusion-based systems. Beyond programming the pump system to extrude at the proper rate, the flow of certain polymers, such as silicone, may be difficult to start and stop quickly. In our experience, there is a high amount of backpressure required to extrude a high viscosity elastomeric silicone, so the extrusion process is never stopped once it reaches an equilibrium flow rate. Systems using continuous extrusion may have to be use a custom code, such as the path planning for fermat spirals (*126*) which start and end in the same place but do not cross over previously deposited areas in the same layer. Extrusion systems can also benefit from auger-like geometry inside the extruder, small valve placement near the tip of the nozzle, or high yield stress fluids which do not extrude until a certain pump pressure is reached, to control fluid flow.

### 1.4.2 Equipment Choices for Photopolymerization Additive Manufacturing

Equipment choices for photopolymerization printing in soft robotics run from proprietary (PolyJet, Stratasys) all the way to custom made. The working principle of a PolyJet system is a set of inkjet heads which jet small droplets of photopolymer onto a build plate which are then cured via UV light. This process is able to produce parts with accuracy as high as 0.1 mm (*127*), but it is also an expensive system. Other methods to create novel soft robotics, such as digital light projection, are able to use

existing SLA printers with some modification. Completely custom-built printing systems have also been used. A few examples of custom equipment for soft robotics photopolymerization printing are: an existing SLA printer (Ember, Autodesk) with a replaced build window (for easy delamination and slower window degradation) (*72*), a digital light projection 3D printer (Free form Plus 39, Asiga) with a custom-made heat resin bath (*82*), and a custom-built setup (using a projection microstereolithography CEL5500 LED light engine (Digital Light Innovation), a translation stage (LTS300, Thorlabs), stepper motor (SparkFun), and Arduino UNO) (*80*). A thin layer of Sylgard PDMS has also been used as a polymerization inhibitor in a projection stereolithography system where layers are added at the bottom of the resin tank (*81*). These altered or custom equipment systems all rely on the ability of the printer to transmit adequate UV light in the proper wavelength for the specific chemistry. Cure depth, resin penetration depth, and amount of radiation are also considered when designing stereolithography systems (*119*). These parameters are a result both of equipment choices and photopolymer chemistry. In bottom-up projection systems, where layers are formed on the bottom of a resin tank and the part is lifted out of the bath as layers are added, a detachment mechanism has to be built in to the bottom of the tank to ensure that the model doesn't stick. This has been addressed with non-stick coatings such as Teflon as well as the PDMS layer described above.

## 1.5 Review of Motivations of Materials and Fabrication Processes in Soft Robotics

Additive manufacturing of soft robotics, and the material creation and characterization that enables the improvement of soft robot additive manufacturing, are the main focuses of this thesis. The previously described trends in soft robot additive manufacturing are only the beginning of what is possible to improve the material choices and manufacturing methods in soft robotics. The reader will notice that some of the examples are focused on improving additive manufacturing methods and are not necessarily soft robotics-focused. Much of soft robotics research does not necessarily revolve around the development of additive manufacturing processing techniques and their subsequent material characterization and creation, but this inclusion would significantly improve available materials and processing methods for soft robotics technologies. By actively pursuing materials development and additive manufacturing, predictable, high quality, and scalable soft robots are achievable. This work contributes to these solutions by addressing the creation and characterization of materials, individual material additive manufacturing solutions for soft robotics and a multi-material manufacturing solution. These individual works also each produce a functional actuator or actuator system for soft robotics as evidence of success of the methods. The following chapters each outline a project addressing some or all the previously mentioned grand challenge topics.

# 2

# Developing Environmentally Benign and Degradable Elastomers for Soft Robotics (Lamination and UV Curing)

**Notes on Chapter 2**

These papers describe the synthesis of a custom biodegradable elastomer (bio-sourced and bio-based) for use in soft robotics, specifically addressing needs in the soft robotics community for robots that disappear after use (*4*). The ultimate goal of this synthesis (as seen in the second paper in this section) is to create a 3D printable version of the custom polymer via UV curing. Emphasis is also placed on the importance of integrating materials science into robotics labs in order to facilitate the custom creation of materials for soft robotics, as opposed to only relying on out-of-the-box material solutions. Creating custom materials gives a higher level of control over the printability of the part and its final material properties. A secondary goal of these works was facilitating the inclusion of materials synthesis into a robotics lab by simplifying the types of equipment and reducing the number of steps needed to create a custom elastomer.

The first work details the one-pot method of creating PGS-$CaCO_3$, a biodegradable elastomer than can be laser cut and assembled into soft actuators. The second work builds upon the previous by adjusting the chemistry of the PGS to employ a

biosourced and biodegradable crosslinker (itaconic acid) as well as a biodegradable photoinitiator (1-hydroxycyclohexylphenyl ketone) to make the PGS polymer (now PGSI) curable via a UV light source. This UV curing chemistry can potentially be used in an extrusion/UV system in order to make 3D printed soft robots.

## Paper 1 of 2: Using an Environmentally Benign and Degradable Elastomer in Soft Robotics

Steph Walker[1,3], Jacob Rueben[2], Tessa Van Volkenburg[2], Samantha Hemleben[3], Cindy Grimm[3], John Simonsen[1] and Yiğit Mengüç[3]

1. Materials Science, Oregon State University, Corvallis, OR 97331, USA
2. Chemical Engineering, Oregon State University, Corvallis, OR 97331, USA
3. Robotics, Oregon State University, Corvallis, OR 97331, USA

*Published in International Journal of Robotics and Automation, 2017.*

Abstract

This work introduces an environmentally benign and degradable elastomer, poly(glycerol sebacate) with calcium carbonate (PGS-$CaCO_3$), for use in soft robotics. Development of greener materials like PGS-$CaCO_3$ contributes to robot designs that do not require retrieval and can safely degrade in the natural environment. A simplified synthesis method of PGS was used to create elastomer

sheets, which were laser cut/rastered then laminated with cyanoacrylate glue into pneumatic soft actuators. The modified polymer synthesis method is accessible for roboticists and the three chemicals used are non-hazardous and inexpensive. Three accordion-style pneumatic actuators (3, 4 and 5 chambers) were characterized for free displacement and blocked force in both linear extension and curling motions, and an additional four 3-chambered actuators were also tested for leakage and rupture failure. Material characterization of PGS-$CaCO_3$ samples of all ages gave: ultimate tensile strength (UTS) from 48 kPa to 160 kPa, elongation percent at UTS from 157% to 242%, moduli from 45 to 154 kPa, average resilience of 88% at 100 cycles, and maximum compressive force of 246 N at 50% strain. The polymer degraded with an average mass loss of 20% across 12 samples after 7 days in a 50-55°C compost pile. PGS's strength, elasticity, biodegradability and chemical safety make it a desirable option for roboticists looking to leverage environmentally benign and degradable materials. PGS may also prove a potential green alternative for robotics applications in ubiquitous environmental and infrastructure sensing.

## Introduction

Soft robotics as a burgeoning field exploits the new material properties available in elastomers (*128*). Bioinspired soft robot designs rely on these elastomers to actuate, grab, envelop and otherwise deform to perform tasks. The intersection of materials science and soft robotics is especially valuable considering that many already existing elastomers can be incorporated into soft robot production (*129*). Environmentally benign and degradable technology (also called "green technology") has many well-

known benefits including reducing damage to the environment and human health as well as reducing nonrenewable resource use (*130*). Green design for robotics in particular has the additional benefit of introducing a wider variety of robotic materials for a larger array of tasks. Incorporation of degradable materials into a robotic device increases its potential to perform tasks where retrieval of the robot is impossible. High-volume environmental data collection (*131*), microsurgery (*132*), precision agriculture (*133*, *134*), and dangerous location exploration (*135*, *136*) will all benefit from greener materials in robotics. Green elastomer development for soft robotics, however, has been lacking. Soft robotics faces the challenge of finding degradable elastomers that function well under repeated deformation and can be fabricated quickly, in addition to having accessible chemistries for roboticists. Current soft robot materials include off-the-shelf soft silicone rubbers (*128*), polyurethanes (*137, 138*) and acrylic foam tapes (*139*, *140*). In terms of temporary robotics, all have issues with low degradability, difficult customization, or hazardous chemistries if the roboticist wishes to synthesize their own material. Knowing inherent hazards in chemical syntheses as well as degradability of the final polymer are important when creating soft robots designed for temporary use. Silicone elastomers can degrade chemically (*141*), especially at high temperatures (*142*) but are considered non-degradable polymers in medical technologies, where they are commonly used (*143–146*). Ecoflex (Smooth-On) cured silicones are also not biodegradable according to a representative from the company. Polyurethane syntheses can require toxic isocyanates (*147*), and acrylic acid monomers can be explosive (*148*). Incorporation of additives into PDMS to change its final structure has given very interesting results (*149*), but material

possibilities can still be expanded through inclusion of other elastomers in soft robot fabrication. Greener materials have the potential to reduce safety concerns during more in-depth robot material customization while increasing biodegradability.

The transition, however, is not so simple. Making custom elastomers can require investment in chemistry equipment, and have complicated syntheses not necessarily accessible for a robotics lab (*150–152*). The balance of ease of manufacture with green material creation must be struck when incorporating materials science into the more mechanical engineering-focused field of robotics. Nevertheless, there are current synthesis methods that can be performed by roboticists in order to bring customizability and creativity to the elastomer material design, one of those being poly(glycerol sebacate) or PGS.

In this paper we introduce green chemistry techniques for the synthesis and fabrication of a soft robot material (Fig. 1). We select a promising candidate material first introduced as an implantable biodegradable elastomer (*153*), poly(glycerol sebacate) with an additive of calcium carbonate ($PGSCaCO_3$). We outline the materials and methods to synthesize PGS-$CaCO_3$ from its raw constituents with a minimum of equipment and develop fast fabrication techniques for pneumatic actuators. We evaluate actuators and mechanical properties of the green elastomer under static, cyclic and compressive loading conditions as well as discuss the elastomer's degradability.

# Background and Related Research

## Soft Pneumatic Robots

Pneumatic actuation remains the most common actuation mode for soft robots. Pneumatic muscles consisting of a bladder with braided outer shell were first developed by McKibben in the 1960's (*2*, *154*). Strategic placement of where the elastomer will deform defines locomotion. These actuators can mimic biological motion of soft creatures like caterpillars, sea slugs, and octopi as well as tongues and elephant trunks (*155*). Some examples of pneumatically actuated soft robots include quadrupeds (*156*), grippers (*2*, *157*), tentacles (*10*), modular soft robots (*158*, *159*) and muscle forms in general (*160*, *161*). Pneumatic soft robots have also been suggested for medical use like the Colobot (*162*) for colonoscopy surgery, and a swallowing robot for patients with dysphagia (*163*). One limit to the performance of these robots is possible slow expansion, which can be improved by reducing the required volume of gas needed for actuation (through structural geometry) as well as tuning material compliance (*123*) or wall thickness.

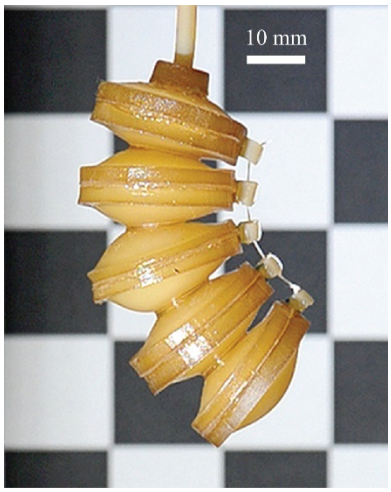


**Figure 1.** PGS-$CaCO_3$ assembled into pneumatic actuators by laser cutting and adhering layers together.

## Degradable Robots

Environmentally-friendly robotics research has employed a variety of degradable materials: a biodegradable miniature gripper for surgery (*132*), biodegradable and edible gelatin actuators (*164*), robotic scaffolds for tissue engineering (*165*), a degradable origami robot (*166*), proposed biodegradable caterpillar robot (*167*), and a microrobot for drug delivery (*168*). While biodegradable rigid materials are relatively well explored, more work is needed in the field of soft green elastomers in robotics. Natural rubber is the most commercially available polymer, but has not seen a lot of use in soft robots.

## Green Elastomers

Biodegradable elastomers potentially used for soft robotics include natural rubber, PGS, polycaprolactone (*169*), poly(vinyl alcohol) hydrogels (*170*), poly(1,8-octanediol-co-citric acid) (*171*), and others. Poly(glycerol sebacate) (PGS) is a tough biodegradable elastomer first introduced for potential applications in medical devices (*153*). The synthesis of this elastomer includes a melt under nitrogen flow and curing step under vacuum with sebacic acid and glycerol monomers (and typically no solvents). Ideal synthesis of PGS produces water and the polymer itself with no chemical waste beyond solvents and/or soap used to clean glassware. Green chemistry principles and analysis suggest that PGS production and use could be more sustainable than current common elastomers (silicones, polyurethanes, acrylic adhesives). PGS monomers come from renewable resources (sebacic acid from the Ricinus communis (castor oil) plant (*172*), glycerol potentially from vegetable fats and oils) (*173*). Though the calcium carbonate additive is likely mined, it is a natural substance that makes up shells and bones and is only harmful when concentrated (*174*). Biodegradation of PGS occurs via “surface degradation by cleavage of ester linkages” (*175*). Under animal skin PGS disappears within 60 days (*153*) . After breakage of its ester bonds, PGS has acidic degradation products (*176*, *177*) that can be toxic to cells. But, sebacic acid has an NFPA hazard rating less than or equal to vinegar (depending on the supplier of the vinegar) (*178–180*), and it is a component of a natural metabolic process in the body (*153*). PGS degradation has not been extensively studied in the environment so it is difficult to say how fast it will degrade, but glycerol components are readily taken up by microorganisms (*181*), and calcium carbonate is already present in the environment (*174*). Inclusion of a basic additive

(Bioglass) (*176*) in PGS has been suggested as an option to lower the toxicity of acidic degradation products through acid/base neutralization. Sebacic acid polymers and glycerol are also approved by the US Food and Drug Administration for medical use (*153*) and have low health, fire and reactivity hazard ratings (*179*, *182*, *183*).

PGS has been polymerized with various additives for: tuning biodegradation (glycolic acid (*184*)), tissue engineering research (gelatin (*152*)) (poly(ethylene glycol) (*185*)), and creating photocurable elastomers (acrylates (*151*)). PGS can also be cured in different amounts of time in order to control crosslinking and therefore mechanical properties (*186*, *187*). Rai et al. (*175*) reports that PGS has an "average tensile Young's modulus between 0.0250–1.2 MPa, UTS greater than 500 kPa, and strain to failure greater than 330%," although even greater elongation at failure, 550%, was observed with an addition of Bioglass (*188*). Bioglass (45S5) is a mixture (by weight) of "45% silica (SiO2), 24.5% calcium oxide (CaO), 24.5% sodium oxide ($Na_2O$), and 6% phosphorous pentoxide ($P_2O_5$) (*189*)." It is a degradable bioceramic (*188*) that bonds with bone and stimulates bone growth (*190*). In Liang, et al. (*188*), it was hypothesized that the calcium carboxylate groups are the primary contributor to the extreme elongation of Bioglass-PGS via ionic crosslinking (*188*). To try to improve elongation of our PGS polymer, we used calcium carbonate as an additive because it is an abundant natural material and safe enough to use as a food supplement (*174*). Calcium carbonate is expected to react with the ends of the sebacic acid to produce calcium ions and carbon dioxide gas, though the extent of reaction between $CaCO_3$ and sebacic acid for was not determined for this paper. The strength

of the final polymer could be improved by such ionic crosslinking. If the robot spends the bulk of its time underwater, the calcium might dissociate, which would reduce the crosslinking effect and decrease the modulus of the polymer (*188*).

## Materials and Methods

### Synthesis of and Assembly of PGS-$CaCO_3$ Actuators

Glycerol (Fisher Scientific) and sebacic acid (Sigma Aldrich, 99%) were melted in a 0.16:0.16 molar ratio with 1 wt% of calcium carbonate (J.T. Baker, 99.0%) between average temperatures of 134 and 139°C in a 250 ml round-bottom flask for 24 hours under approximately 100 ml/min nitrogen flow. Stirring was set to level 1 on the hot plate. The melt (pre-polymer) was then poured onto a clean PTFE-coated liner set in a metal baking pan and cured at average stage temperature of 137 to 143°C in a vacuum oven (50.8 kPa) for 10-11.25 hours (Fig. 2). Crosslinking was not controlled after curing beyond taking the sample out of the oven. Temperature of the melt varied slightly because of changes in room temperature. Because the melt was in a hood, the air flow affected the heat transfer between the aluminum flask holder and the polymer melt.

Samples were coated with corn starch and/or olive oil to reduce stickiness during fabrication. The approximately 3 mm thick sheets were then laser cut and/or rastered into either dumbbell or actuator shapes. Cutting was performed with two passes on a

VLS4.6 Universal Laser Systems Laser Cutter (60 W) at 50% power, 5% speed, 1000 PPI, and with the 2.0 lens, with the laser focused at the bottom of the polymer. Rastering was performed at 50% power, 30% speed, 1000 PPI with the laser focused at the bottom of the polymer. Rastering creates height differences in the actuator pieces for a more defined glue boundary. The focal point of the laser was the bottom of the polymer to accommodate the varying height of the samples (approximately 2.6 to 3.8 mm). Any crosslinking after fabrication was not studied in this work.

The laser cut and rastered circular layers (25 mm diameter) were laminated into actuators using a approximately 1 mm bead of cyanoacrylate gel glue (Loctite Super Glue Ultra Gel Control). The raised edges of the layers reduced the spreading of the glue to undesired parts of the actuator. The rastered away portions of the layers created air gaps for the actuator chambers. Latex tubing was cut into approximately 3 mm long beads and glued to the actuator to make a spine for tying a cotton thread to make a strain-resistant side (Fig. 3). For comparison, three actuators were made out of Ecoflex 00-30 (one of each of 5- 4- and 3-chambered) using a similar process. Ecoflex 00-30 was poured into molds with the same dimensions as the laser cut PGS-$CaCO_3$, degassed for 3 minutes and cured in a 40°C oven for 30 minutes. The components were then laminated together using Sil-Poxy (Smooth-On). Tubing (non-latex) was then attached in a similar way as previously described.

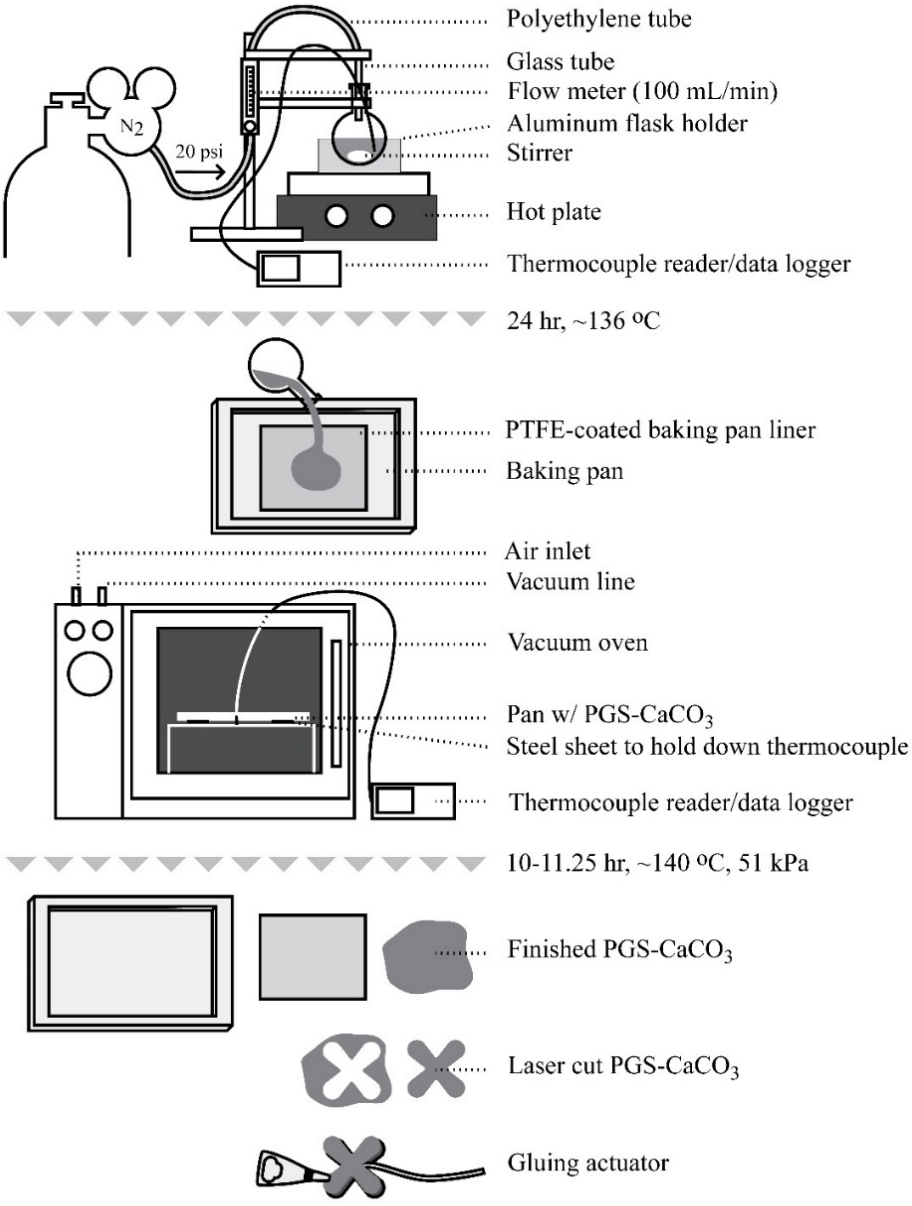


**Figure 2.** Synthesis of PGS-$CaCO_3$ includes a melt step and a cure step followed by laser cutting, rastering and gluing the polymer sheet to create a robot actuator.

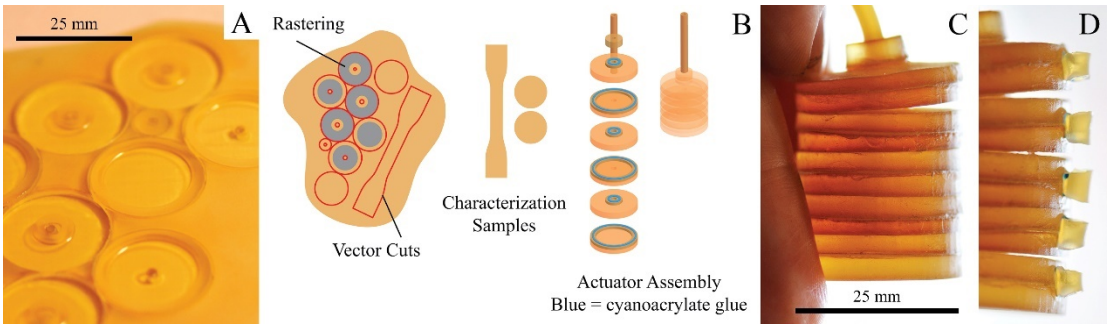


**Figure 3.** (a) The PGS-$CaCO_3$ sheet was laser cut and rastered to create actuator components which were laminated together with cyanoacrylate glue. Rastering the polymer sheet gives control over thickness of the polymer layer and was used to create raised edges for gluing. (b) Diagram of laser cutting plan for each PGS-$CaCO_3$ sheet. Both vector cuts and rastering were used to create 25 mm circular disks for laminating into a 3-, 4-, or 5-chambered pneumatic actuator. (c) A 5-chambered pneumatic actuator in a neutral position. (d) Pieces of 1/8” outer diameter amber latex tubing approximately 3 mm long were glued to one side of the actuator so a cotton thread could be tied to create a strain resistant layer.

Actuator Testing (Extension, Force, Peeling, Leakage)

Free extension for 5-, 4-, and 3-chambered actuators (Actuators A, B and C) was measured under air pressure in 0.34 kPa increments. Inflation pressures were chosen so that leaking or breakage could be avoided for the PGS-$CaCO_3$ actuators. Extension was measured once for both curling and straight actuators. Actuator elongation lengths were measured manually with the pen tool in Adobe Illustrator.

Free extension was also measured for two additional 3-chambered actuators, one actuator for straight extension (Actuator D) and one actuator for curling extension (Actuator E), until leakage and then to failure. Elongation percents and pressures at leakage and break were recorded. Ecoflex actuators were not tested for leakage and failure.

Actuator blocked force was measured once for each actuator for both curling and straight pneumatic actuation using an Ohaus Scout Pro mass balance. One side of the actuator was set against a stationary clamp and the other was lightly set on the scale. For straight blocked force the actuator was placed directly on the scale. For the curved blocked force the actuator tip was placed lightly on the scale. The Ecoflex actuators were also subjected to straight and curved blocked force tests. Mass readings were multiplied by 9.81 $m/s^2$ to get force values. Blocked force and pressure at leakage and failure were also recorded once for two additional 3-chambered actuators (for curling (Actuator F) and straight (Actuator G) blocked force).

Peeling between adhered PGS-$CaCO_3$ layers was tested with 10 commonly available glues. Two 20 mm x 5 mm strips of the polymer were adhered together with one polymer also attached by cyanoacrylate glue to a tongue depressor. Experimental glues were applied between samples and left overnight to dry. Two pieces of wood were cut and adhered with cyanoacrylate glue to the other polymer end where a bag was hung to gather incremental mass increases. The glue that held the most mass before delamination of the two PGS-$CaCO_3$ layers was chosen for fabrication.

Leakage in the actuators was determined by inflating Actuators A, B, and C to their maximum testing pressure with a syringe and clamping the syringe position (6.9 kPa for Actuators A and B and 3.45 kPa for Actuator C). The change in pressure over the first 30 seconds was determined once for each actuator. Leakage is also noted in elongation and blocked force data for Actuators D, E, F, and G.

## Tensile, Cyclic, and Compression Testing

Tensile tests were performed on dumbbell samples using a Mark-10 testing machine (25 N load cell) with extension rates of 100 mm/min and 500 mm/min. Dumbbell samples were based on the dimensions laid out for Die D in ASTM D412 (original parameters from ASTM D412 Die D: height 16 mm +/-9 1 mm, width 100 mm minimum, gauge length 33 +/- 2 mm, large curvature radius 16 +/- 2 mm; parameters from PGS dumbbell vector: height 16.5 mm, width 101.6 mm, gauge length 33.7 mm, large curvature radius approximately 16 mm). The tensile testing speed of 500 mm/min was used to adhere to the lower bound ASTM D412 speed designation. Samples were also run at 100 mm/min to replicate a slowly expanding robot. Sandpaper pieces (approximately 17 mm x 20 mm) were glued with cyanoacrylate adhesive (Loctite Super Glue Ultra Gel Control) to both sides of the ends of the dumbbell shapes to reduce slipping during testing. Stress versus elongation percent data of approximately one day old PGS-$CaCO_3$ samples tested at 100 and 500 mm/min and three older samples at 500 mm/min are plotted. To explore relationships between material properties and processing conditions, moduli and

UTS of samples of all ages (11 total) are plotted versus melt temperature, thickness, and age. Modulus was determined using the average slope of each sample for the first 10% of the stress vs. elongation % graph. Moduli from all approximately one day old samples is plotted versus elongation percent to observe nonlinearities. Tensile tests (500 mm/min and 100 mm/min) were also performed on 4 samples of cured Ecoflex 00-30 and 4 samples of cured natural latex rubber (from Liquid Latex Fashions, poured and dried in air). The same dumbbell size as the PGS-$CaCO_3$ samples was used. One representative curve from each material at both speeds is plotted with PGS-$CaCO_3$ to compare material properties.

Cyclic loading tests were also performed on approximately 1 day old dumbbell samples using a Mark-10 testing machine (25 N load cell) with an extension rate of 500 mm/min. Samples were pulled to 60% elongation and released at 500 mm/min for 100 cycles. Hysteresis behavior is shown in a stress vs. elongation % plot. Resilience (the percent of energy not lost to hysteresis) is calculated using cycle 100 data with areas under the loading curve (AL) and unloading curve (AU) (*191*) (Equation 1).

$$Resilience\ (\%) = (1 - (AL - AU) / AL)*100 \quad (1)$$

Degradation Analysis

Degradability was tested in a cattle waste hot compost (approximately 50-55°C). Samples (25 mm diameter, 4 and 0.5 days old) were sewn into fiberglass (screen door

material) mesh bags with fishing line, weighed (sample,line and bag), and then buried 24 inches deep into the compost. After seven days, each sample was removed from the compost, shaken in a bottle with deionized water for 10 minutes to remove debris, and set in a 35°C oven to dry for 24 hours. A degradation timeline of one week was selected as a starting point in order to get a general idea of degradation in a short time. Samples were dried for one day in order to get rid of excess water that would change the mass of the elastomer. The dried samples in the mesh bags were weighed and mass loss was calculated for each. A fresh polymer sample surface is compared to its "after" photo in the mesh bag. Mesh bags were inspected to ensure that no fishing line had broken (no samples slipped out).

## Results

### Actuator Testing (Extension, Force, Peeling, Leakage)

Images of actuator A, B, and C extensions (straight and curved) as well as measurement methods are presented in Fig. 4. Actuator elongation percents and blocked force values for both curling and straight pneumatic actuation for Actuators A, B, and C are presented in Fig. 5. Results from the characterization of Ecoflex 00-30 actuators are included for comparison.

Elongation percent per pressure input in the PGS-$CaCO_3$ actuators increased as the number of chambers decreased. This could be due to slightly varying material properties across actuators. The PGS-$CaCO_3$ 5- and 4-chambered actuators also

showed a decreasing elongation percent increase as the pressure was increased, seemingly due to reaching the limits of the amount of extendable material (cyanoacrylate glue makes the edges stiffer). The curved PGS-$CaCO_3$ actuators behaved similarly but with elongation percents mostly exceeding the straight actuators. The elongation percents for straight actuators ranged from approximately 39 to 49 elongation percent, and for curved actuators 46- 48 elongation percent. The Ecoflex 00-30 actuators performed in a similar elongation percent range but did not display the extendable material limit behavior shown in the PGS-$CaCO_3$ samples. The Ecoflex samples did show a more linear trend for elongation percents with higher elongation than across most PGS-$CaCO_3$ actuators. This is expected because the Ecoflex 00-30 and Sil-Poxy adhesive actuators are softer overall than PGS-$CaCO_3$.

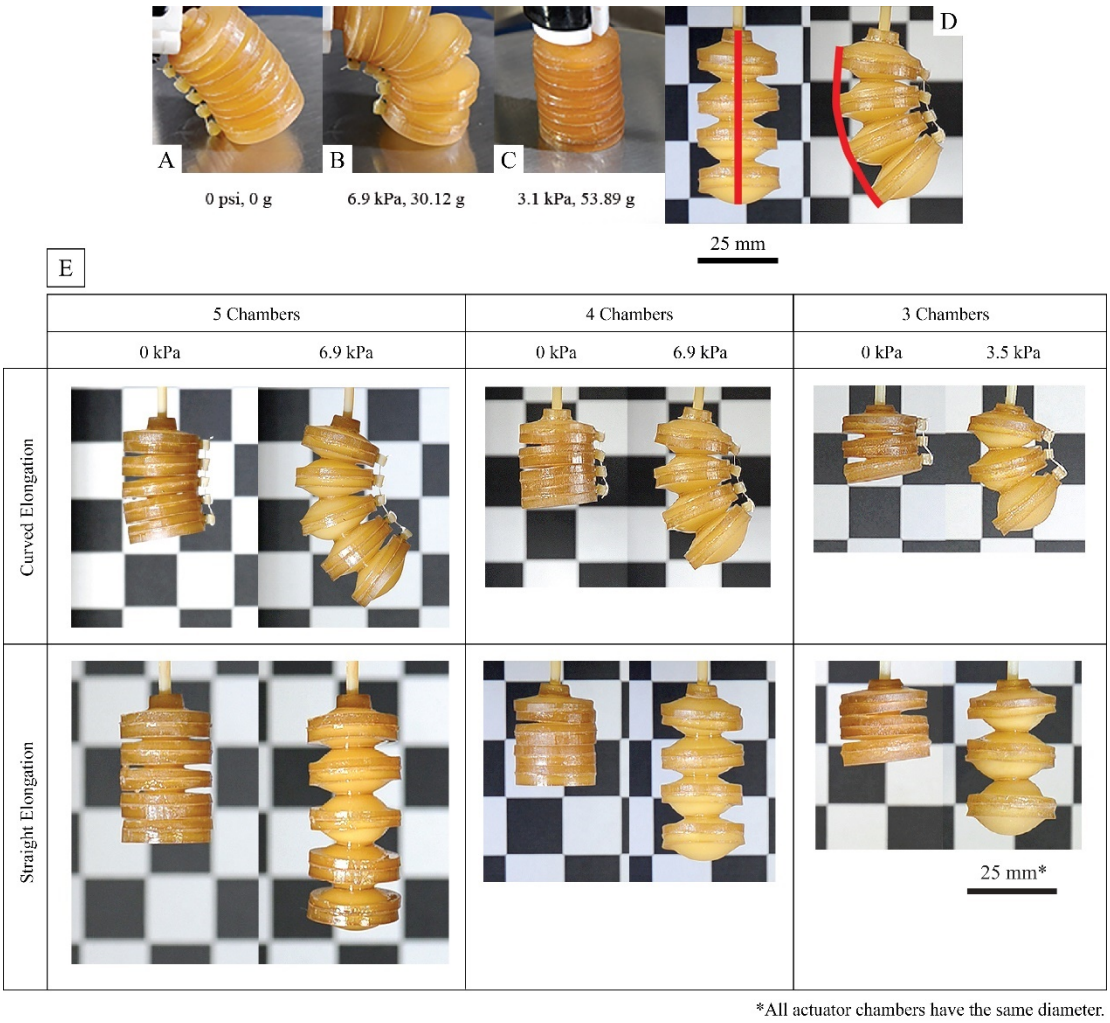


**Figure 4.** (a,b) Placement of the actuator for curved blocked force at 0 kPa and 6.9 kPa. (c) Straight blocked force at 3.1 kPa. (d) Elongation percent was measured using manually drawn line lengths in Adobe Illustrator. (e) Three accordion shaped pneumatic actuators (Actuators A, B and C, respectively) were inflated with 0.34 kPa increments of air and characterized for length of free extension in a straight and curled configuration.

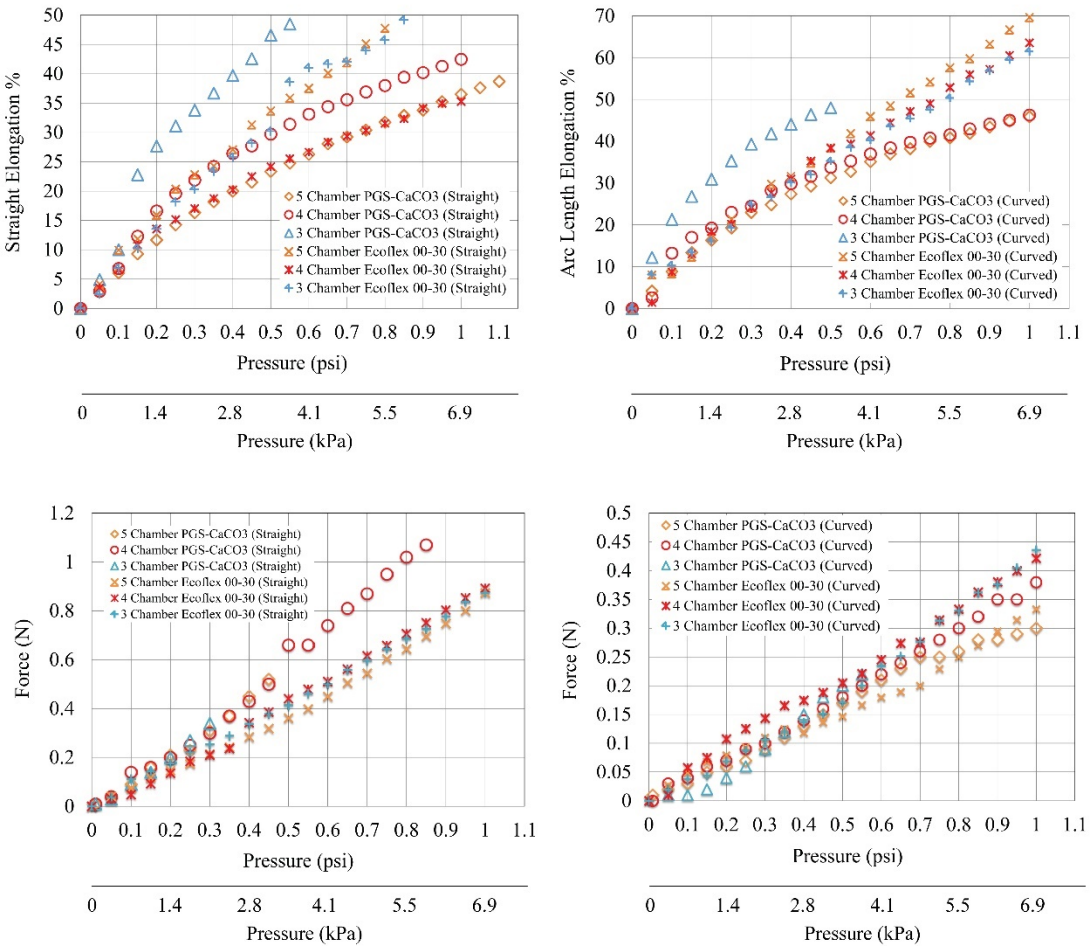


**Figure 5.** (a) Elongation percent of straight free expanding actuators with up to 6.9 kPa applied air pressure. (b) Arc length elongation percent of curved free expanding actuators with up to 6.9 kPa applied air pressure. (c) Blocked force for straight chambered actuators. (d) Blocked force for curved chambered actuators. PGS-$CaCO_3$ elongation shows some stiffening behavior at higher pressures that is not seen in most actuators made using the softer Ecoflex 00-30.

Straight blocked force for all three PGS-$CaCO_3$ actuators overlapped in an almost linear trend. Maximum force of 1.07 N came from Actuator B. Curved blocked force

showed a similar trend up to about 4.8 kPa when Actuator A began to apply less force. This could be from the 5-chamber actuator's ability to expand more in the middle and curl instead of press on the mass balance plate. The maximum force (0.4 N) was again from Actuator B. The straight blocked force was smaller overall for the Ecoflex actuators, especially at the higher pressures. This makes sense from the Ecoflex 00-30 tensile testing data, which shows it has a smaller modulus than PGS-$CaCO_3$. The Ecoflex samples, even when put together with the stiffer Silpoxy adhesive, are still softer overall than the PGS-$CaCO_3$/cyanoacrylate combination. The curved blocked force for the Ecoflex actuators fell in line with the PGS-$CaCO_3$ data, probably due to the actuators having similar geometry, limited expansion space, and the low pressures in testing.

Results for Actuators D, E, F and G tested to leakage and then to failure are as follows. Pressures at leakage of these actuators were 16.9 kPa (straight 96% extension), 12.4 kPa (curved 93% extension), and 12.3 kPa (curved 0.21 N force). The straight blocked force test reached the limit of the scale (1.84 N at 12.5 kPa) before any breaking or leakage was detected. Pressures at failure of these actuators were 19.7 kPa (straight 106% extension), 17.2 kPa (curved 136% extension), and 30.8 kPa (curved 0.064 N force because of slipping). These actuator samples have an average melt temperature of 138°C and an average oven temperature of 141°C.

The best adhesive tested was the Loctite Super Glue Ultra Gel Control. When held together with Loctite Super Glue, the polymer broke before the glue debonded. Leakage for Actuators A, B, and C in the first 30 seconds of inflation was 0.21 kPa, 0.21 kPa, and 0.69 kPa respectively. Leakage occurred at the points where the superglue adhered the two layers of the elastomer together. This was qualitatively observed by placing each actuator in an oil bath and inflating the actuator to approximately the same pressure as during testing. (An olive oil bath was used because the cyanoacrylate glue turned white in water.) Small bubbles came out of both the larger diameter glue zones as well as the smaller chamber connector glue zones. Increasing the glue area on the edges of the actuator chambers could reduce leakage (the annulus for gluing was about 2 mm thick). We believe that the leakage has to do either with not enough surface contact between layers of PGS-$CaCO_3$ during gluing, possible chemical interactions with the elastomer and glue causing delamination, and/or cracking of the brittle glue layer during fabrication. We had some success with a flexible cyanoacrylate glue (Loctite Instant-Bonding Adhesive 4851), but its performance was irregular (layers delaminated upon actuation). More research into glues that are compatible with this chemistry will be worthwhile.

## Tensile and Cyclic Testing

UTS at failure of the dumbbell samples ranged from 48 kPa to 160 kPa. Elongation percent at UTS ranged from 157% to 242%. Moduli in the first 10% of data ranged from 45 to 154 kPa (Fig. 6). Overall, PGS-$CaCO_3$ behaves nonlinearly and some of the 500 mm/min and 100 mm/min samples overlap due to slight differences in

temperature conditions or thickness. For the 500 mm/min tests, samples cut from the same sheet of polymer overlapped, but had different elongation percents at break. The 100 mm/min data had a pair of samples that overlapped from different runs. There is still too much variation within the same testing speed to see any trends based on elongation speed alone. In order to determine possible trends in the data, moduli of all the tensile samples were plotted versus: average melt temperature, sample thickness, and age (Fig. 7).

The differences in moduli seem to be related to melt temperatures and sample thicknesses. Cure temperature and time vs. moduli did not show any obvious trends. Observation of the polymer melt when it is poured into the baking pan shows that higher melt temperatures make the polymer more viscous and more likely to form long strands when poured (more polymer interactions are present).

Sample age did not show any strong relationship to moduli. Moduli of the tensile samples also increase with an increase in strain rate. The range, average and standard deviation of moduli for samples tested at 100 mm/min were: 45-123 kPa, 85 kPa, and 28 kPa, respectively.

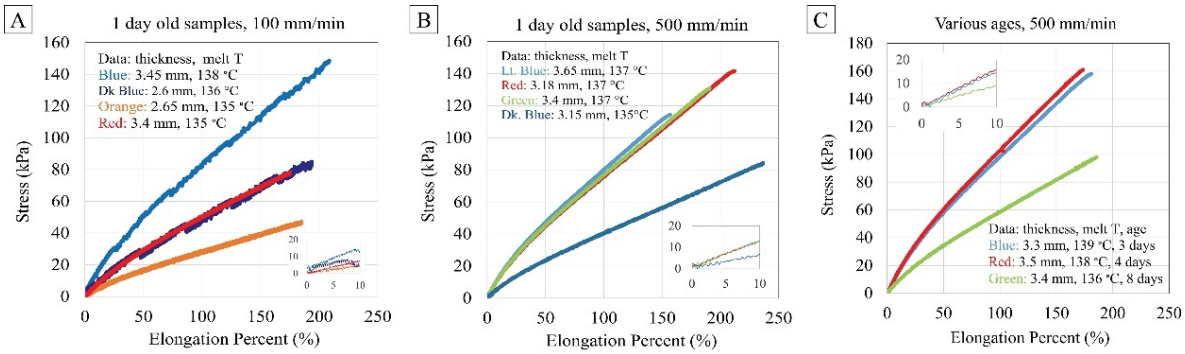


Figure 6: Tensile testing of PGS-$CaCO_3$ samples of slightly varying processing conditions but similar ages (data in Appendix). Tensile tests at (a) 100 mm/min testing speed on approximately one day old samples, (b) 500 mm/min testing speed on approximately one day old samples, and (c) 500 mm/min speed on aged samples were performed. UTS at failure of all dumbbell samples ranged from 48 kPa to 160 kPa. Elongation percent at UTS ranged from 157% to 242%. Moduli in the first 10% of data ranged from 45 to 154 kPa. There is overlap between the 500 and 100 mm/min curves.

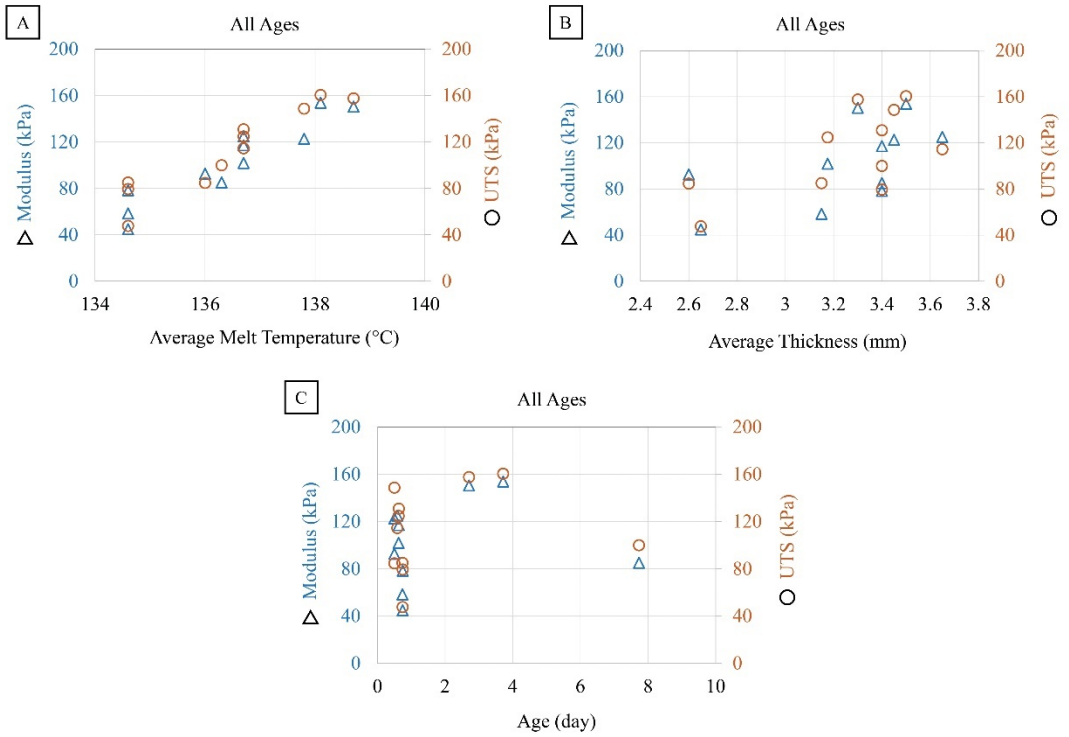


**Figure 7.** (a) Moduli and UTS increase with increased melt temperature. (b) Moduli and UTS increase with increased sample thickness. (c) Age of the polymer does not show any clear relationship to moduli or UTS.

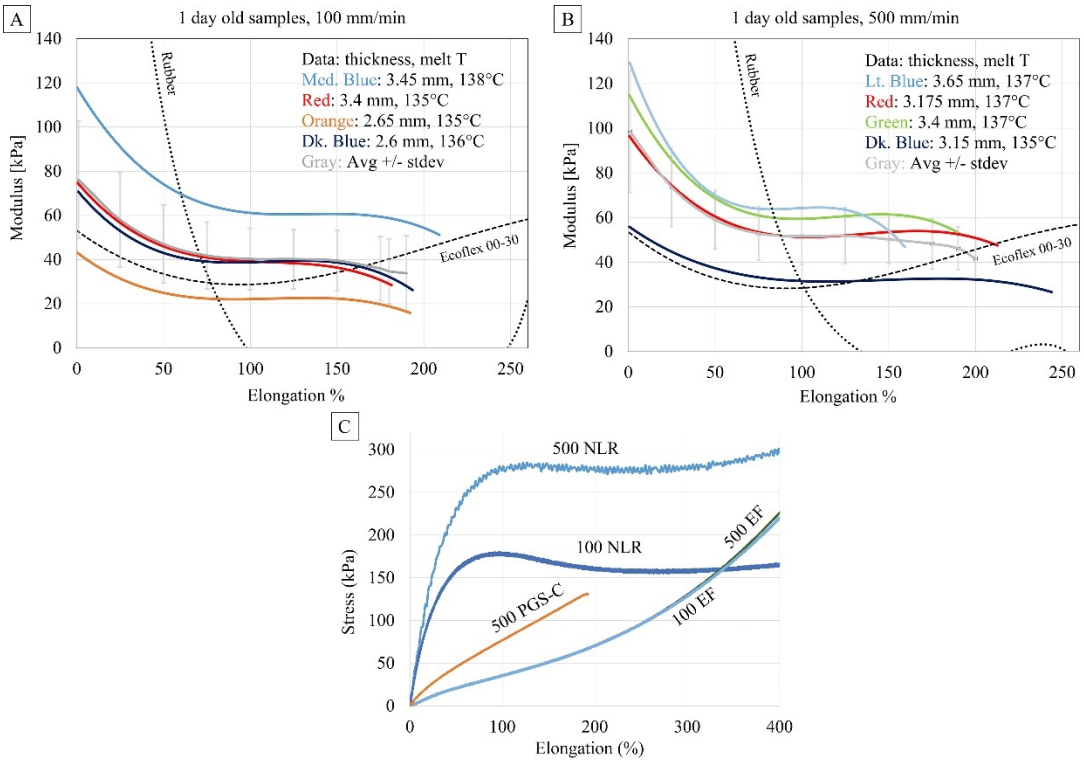


**Figure 8.** Moduli versus elongation percents of PGS-$CaCO_3$ (and Ecoflex 00-30 and natural rubber for comparison) for same age (a) 100 mm/min and (b) 500 mm/min tensile data show the nonlinearity of PGS-$CaCO_3$, but a relatively constant modulus value is reached around 80% elongation and continues until approximately 140% elongation. (c) Tensile testing (500 mm/min = 500, 100 mm/min = 100) of PGS-$CaCO_3$ samples (PGS-C) compared to Ecoflex 00-30 (EF), a common silicone used in soft robotics, and natural latex rubber (NLR). PGS-$CaCO_3$ behavior is nonlinear. Ecoflex samples tested at different speeds overlap at these elongation percents. Natural latex rubber shows plastic deformation starting at around 100% elongation. Ecoflex 00-30 within 200 % elongation has lower moduli than most of the PGS-CaCO3 samples. Rubber's maximum and minimum moduli are out of the range of the PGS-$CaCO_3$ samples.

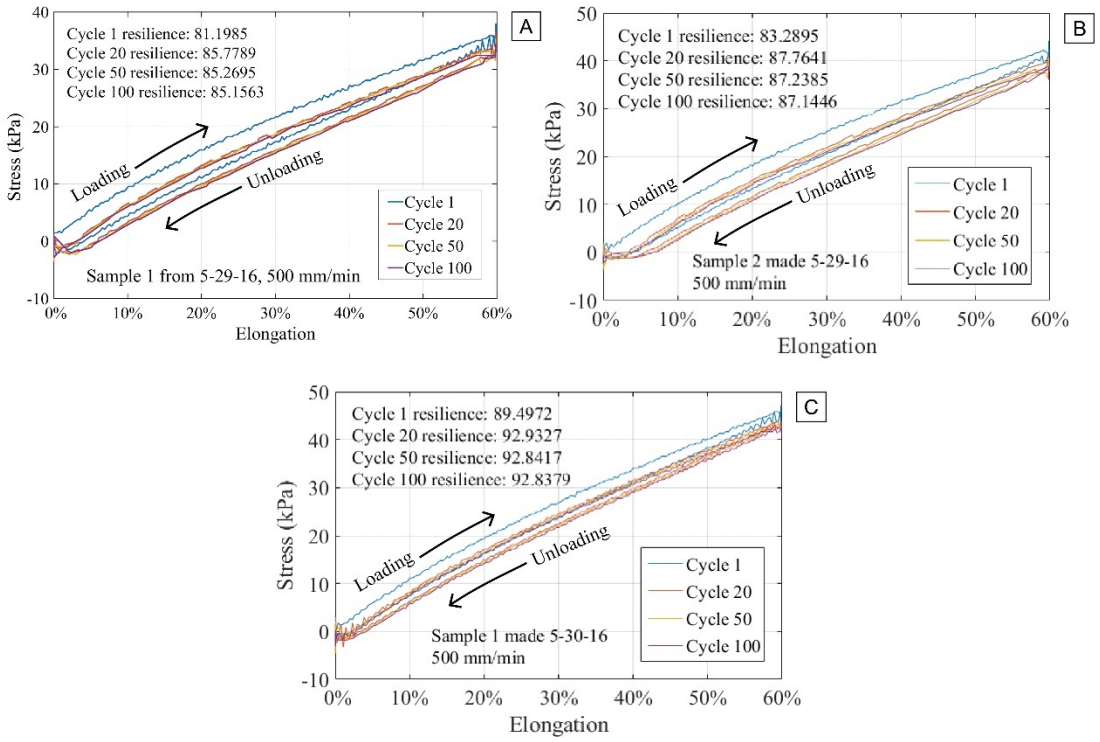


**Figure 9.** (a,b,c) Cyclic testing data from 3 samples less than a day old. Average resilience of the 100$^{th}$ cycle for the 3 samples tested was 88% with a standard deviation of 3% standard deviation of moduli for samples tested at 500 mm/min were: 58-154 kPa, 113 kPa, and 32 kPa, respectively.

PGS-$CaCO_3$ tensile testing modulus curves all have a similar structure where a higher slope occurs within the first 50% of elongation and then a bend occurs, moving towards a lower and more constant modulus (Fig. 8a, Fig. 8b). In plots of modulus vs. elongation %, a relatively constant slope is reached between 80% and 140% elongation. Tensile testing results for Ecoflex 00-30, natural latex rubber, and PGS-$CaCO_3$ are compared in Fig. 8c. Natural latex rubber is stiffer than PGS-$CaCO_3$ and has a large plateau where plastic deformation takes place. Only the 500 mm/min sample of PGS-$CaCO_3$ data was included because 100 mm/min and 500 mm/min

PGS-$CaCO_3$ tensile tests gave overlapping data. Ecoflex 00-30 is less stiff than PGS-$CaCO_3$ and also more nonlinear.

Figure 9 shows three data sets from cyclic loading of PGS-$CaCO_3$ samples. The average resilience was 88% for the 100th cycle from all 3 samples tested with a standard deviation of 3%. Hysteresis occurs, showing that the polymer has some viscoelasticity. In the first cycle, the polymer is permanently deformed and then by the 20th cycle the polymer starts to settle into a repeating loop.

Degradability Analysis

After seven days in the compost, some polymer samples had almost completely disappeared and some were relatively intact. Average mass loss across all samples was 20% with a standard deviation of 22% (Fig. 10e). Mass loss could be even greater in some samples if less wood and dirt became embedded in the polymer. Amount of compost contact could have been low for the intact polymers, as there was no way to ensure identical compost contact for each sample once they were buried. Also, even though there may have been anaerobic pockets in the compost, the degradation is expected to be aerobic. Further degradation testing will clarify degradation type. The best (70% loss) and worst case (4% loss) scenarios are shown in Fig. 10d (Sample 6 and A).

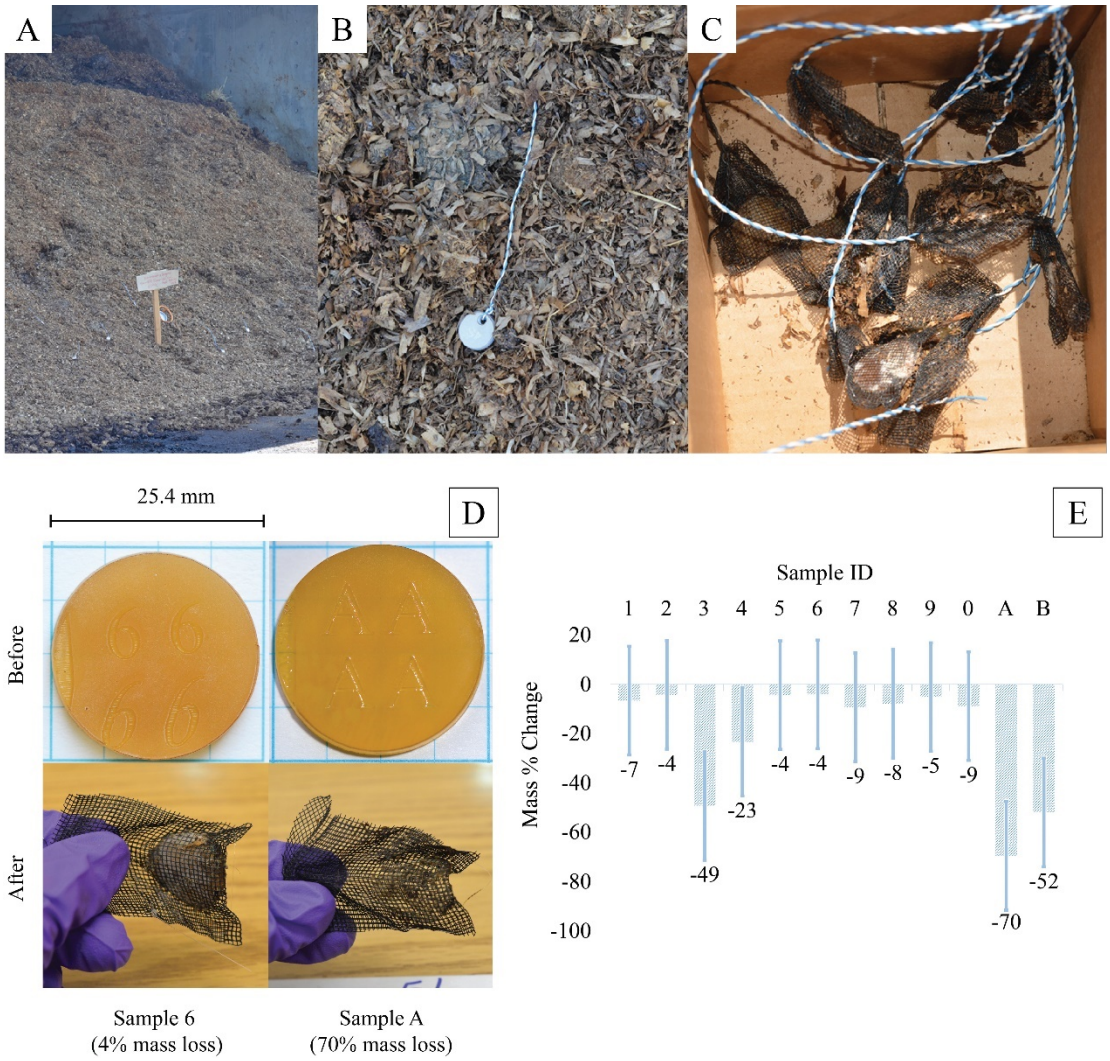


**Figure 10.** (a) Location, (b) burial, and (c) packaging of samples for degradation.(d) Polymer samples 6 and A had the minimum (4%) and maximum (70%) mass loss after being taken out of the compost. Sample A was almost completely gone from the mesh bag. (e) Average mass loss across all samples was 20%, with a standard deviation of 22% and a maximum and minimum value of 70% and 4% loss. The mass loss might have been greater for some samples if debris from the compost were not embedded into the sticky polymer.

## Possibilities for Assembly, Motion, and Application

Lamination possibilities for PGS-$CaCO_3$ can include entire bodies of robots where the pneumatic actuators facilitate simple animal-like locomotion or simple grippers (Fig. 11a, Fig. 11b). A frog robot with a small hydraulic or pneumatic source could swim down onto a river bottom and sample the soil for heavy metals. A gripper could be attached to a caterpillar-like robot to help it grip and climb trees and rocky faces. Application possibilities for robots made of PGS-$CaCO_3$ include those that can apply towards the DARPA VAPR and ICARUS programs (*192*) that seek to develop self-destructive electronics and vehicles that vanish after critical supply deliveries. A PGS-$CaCO_3$ robot would degrade into the natural environment after being used as a component in a delivery vehicle, provided that the other components (electronics, power supply) could also disappear (Fig. 11c). PGS-$CaCO_3$ could also be applied to environmental sensing. As an example, the caterpillar-like robot that climbs trees could sense gases or contaminants in the air. At the end of its life cycle, it would fall to the ground and degrade into the soil. PGS-$CaCO_3$'s potential in medicine has been described in previous work, and by reducing acidic byproducts it may be possible to expand the range of PGS-$CaCO_3$ robots to apply to medical technologies like swallowable robots that deliver medication, for example.

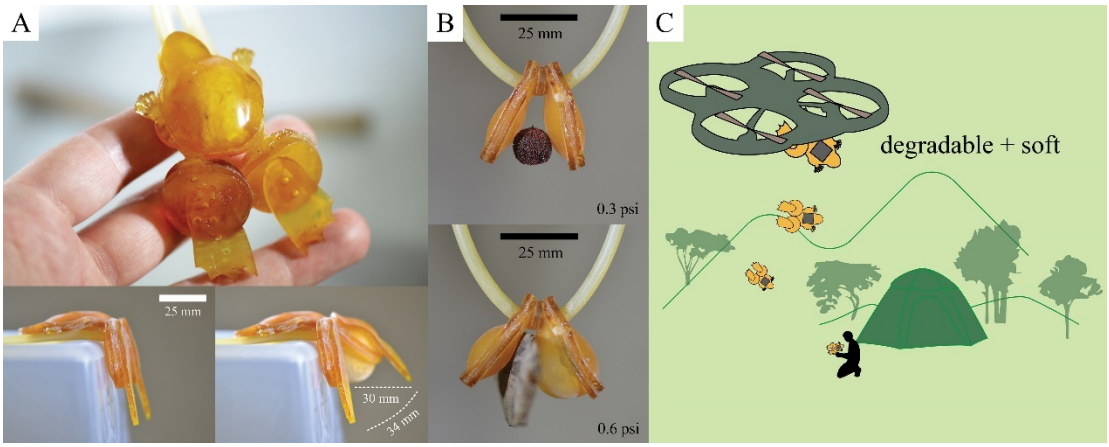


**Figure 11.** Possibilities for fabrication include (a) frog legs and (b) gripper actuators. (c) A possibility for application of a PGS-$CaCO_3$ robot fits well into the ideas laid out in the DARPA ICARUS program where a vehicle disappears after delivering critical supplies. Here we have used the frog as an example of a soft robot that can be dropped with a package and travel to a specified site, then degrade.

## Discussion

PGS-$CaCO_3$ seems to be a promising candidate for further exploration into soft robotics materials science. Both the actuator testing and tensile testing showed that PGS-$CaCO_3$ material properties are in the same ranges as commercially-available Ecoflex 00-30. While PGS-$CaCO_3$ is an exciting candidate to develop further, there are some issues to improve upon.

Settling of a thin layer of what is assumed to be calcium carbonate sometimes occurred after pouring the prepolymer melt, and cracking sometimes occurred during

tensile testing at the CaCO3-dense polymer bottom, so quicker cure times (to prevent the filler from settling after stirring stops) or less CaCO3 would improve homogeneity. Filler composition will be explored in future work. The baking pan warped slightly during use, which could have partly caused the varying height of the sheets. Slight variations in polymer melt temperature are suspected as another cause of varying sheet thicknesses (due to varied viscosities and polymer chain lengths/structures). We also assumed that the thin layers of olive oil and corn starch coatings did not affect bulk material properties.

Elongation percent values of approximately 200% are desirable for soft robots, and PGS-$CaCO_3$'s tensile data fall between natural latex rubber and Ecoflex 00-30 values, but the actuation pressures of PGS-$CaCO_3$ need to be gentler than those made with high elongation silicones like Ecoflex because of PGS-$CaCO_3$'s lower elongation % at break. Variations in PGS-$CaCO_3$ stress/elongation % data seem to originate from slightly varying melt temperatures and thickness differences between samples. More PGS-$CaCO_3$ replicates should be run in a tightly controlled temperature and cure time range to narrow down moduli and elongation percent values. PGS-$CaCO_3$'s extension is close to smooth muscle (300%)(*129*) and could function well as a biological tissue mimic in a robot.

Uneven oven temperature distribution, inhomogeneity of filler, or pre-straining while pulling the polymer off the mold could have also caused mechanical properties to vary within each sample. Using a larger vacuum oven or smaller sheet size would

reduce effects of uneven temperature distribution. Resilience results suggest that the polymer would still function well after 100 cycles of deformation, but hysteresis needs to be taken into account when designing pneumatic power systems. Viscoelastic effects, as evidenced by the hysteresis loop, cause the polymer to release energy as heat. The permanent stretching in the first few actuations of PGS-$CaCO_3$ will also need to be programmed into the robot control system. The tensile properties also appear to be strain rate dependent.

Once cured, we can see that the polymer is changing its opacity over a period of weeks, and this could be an indication of some further property changes. In the current state, the polymer is expected to perform during the time window of 8 days shown in the aged tensile data, though more replicates to confirm this are desired. From a control standpoint, the polymer property changes should be further characterized in the long term to make control of a robot made from PGS-$CaCO_3$ straightforward. Actuator construction can still be improved through automation (3D printing with some alterations in chemistry) and potential molding techniques. Manually making the actuators is not ideal and can introduce errors in gluing. More actuator testing is needed to fully understand the repeatability of the manual process. The glue cracking issue needs to be resolved through more involved study of interactions between glue and PGS-$CaCO_3$ chemistry. The cyanoacrylate glue was also too stiff for the PGS-$CaCO_3$/glue boundaries. More environmentally friendly and flexible glues will be explored.

To address any questions about the release of CO2 (a greenhouse gas) during the synthesis of PGS-$CaCO_3$, a calculation has been performed assuming all $CaCO_3$ reacts. While dissociation of calcium carbonate in reactions with the sebacic acid can produce carbon dioxide, a roboticist can make 1000 small actuators out of PGS-$CaCO_3$ in exchange for driving one less mile in a small car (calculation in Supplementary Information).

## Future Work

Further chemical, polymerization and mechanical testing will be performed to clarify appropriate operation parameters for PGS-$CaCO_3$ robot use, long-term degradation, and time to failure. FTIR (Fourier Transform Infrared Spectroscopy) will give a molecular footprint of the polymer. Polymer characterization – DSC (Differential Scanning Calorimetry) and DMA (Dynamic Mechanical Analysis) will help explain any melting points and glass transition temperatures as well as further explain viscoelastic behavior. Static light scattering will identify the average molecular weight of the pre-polymer (before curing) for comparison to literature and other elastomers. A three-neck flask and condenser setup for the melt step will determine completeness of reaction. Degradation will be characterized via surface erosion behavior with SEM (Scanning Electron Microscopy). Biodegradation can be tested more thoroughly with gas capture techniques. The potential material changes over time need to be further characterized. Other additives and syntheses will also be explored. We suspect that PGS will combine well with several additives and copolymers. Decreasing energy use and testing more environmentally friendly molds

are also priorities. Alongside material characterization, PGS-$CaCO_3$ soft robotic designs will be created that utilize single-mold body shapes and more complicated structures.

## Conclusion

In this work we have introduced the first prototypes of an environmentally benign and degradable soft robot actuator leveraging a biodegradable elastomer. The material synthesis is accessible for those without much experience in chemistry or polymer science, and, elasticity can be varied using the same three chemicals as opposed to buying different formulations of prepared polymers. Also, PGS has been demonstrated in the literature to be fully biodegradable (*175*), so hazardous and long-lasting waste from robot designs is no longer an issue. PGS-$CaCO_3$ will deform and recover under gentle actuation and could be used in biological robots as an organ, muscle, limb or even full body. A green chemistry approach to PGS-$CaCO_3$ synthesis will make workers safer and reduce waste and energy use. Our PGS-$CaCO_3$ synthesis can be performed by roboticists without much prior knowledge of polymer science and improved even further through processing technique and additive exploration, including those that would facilitate 3D printing of the polymer. With the potential to increase soft robot use in data collection, environmental science, and medical technology, PGS-$CaCO_3$ is worth exploring further. We hope that this research inspires other labs to delve into the materials science of their robots to reduce the amount of waste created by this field and explore fascinating impermanent options for robot design.

Supporting Information

## A.1 Equipment

Equipment: Regulator: Smith, for Nitrogen tank

Flow Meter: Dwyer RMA-150-SSV

Hot Plate: IKA C-MAG HS 7

PTFE-coated liner: Linden Sweden–Jonas of Sweden

Metal baking pan: Nordic Ware

Vacuum oven: VWR Scientific 1410

Thermocouple Readers: Amprobe TMD-56

Aluminum reaction block: Scilogex

## A.2 Tensile Testing Dimensions

Tensile and cyclic loading were performed with dumbbell shaped PGS-CaCO3 samples of this size. Sheet thickness of PGS-CaCO3 ranged from approximately 2.6-3.8 mm.

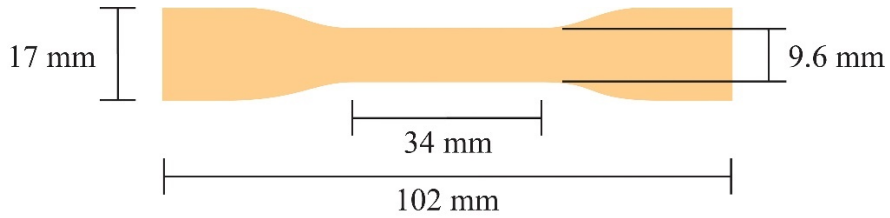

## A.3 Leakage and Failure

Failure tests for Actuators D, E, F, and G. Extension at failure ranged from 106% at 19.7 kPa to 136% at 17.2 kPa, and failure for force applied ranged from 1.84 N at 12.5 kPa to 0.064 N at 30.8 kPa due to slipping of the curved actuator.

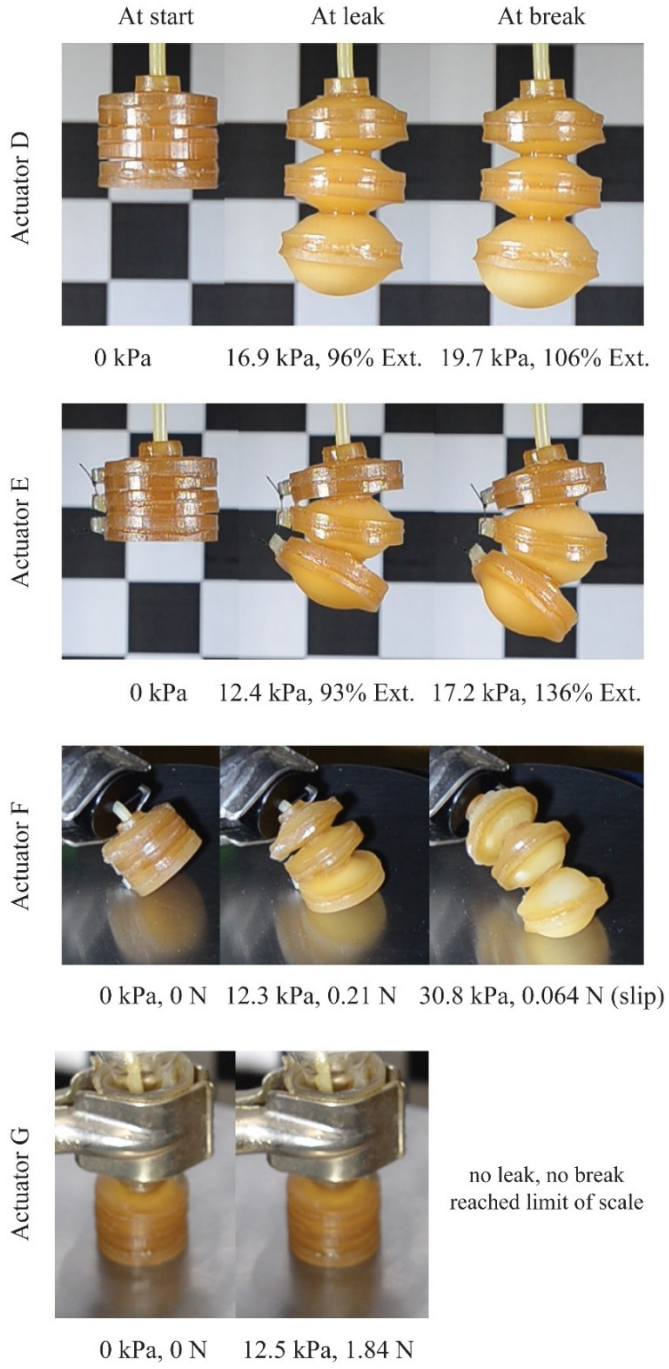

### A.4 Motion Capture

Motion capture markers were placed on two of the four chambers of Actuator B, two markers per chamber. The grid was drawn by hand with a permanent marker and a ruler using 0.5 cm spacing. The actuator's pressure was increased from 0 to 6.9 kPa evenly across 22 seconds using a syringe controlled by hand. The motion was recorded both by a four-camera OptiTrak system and a Nikon D7000 camera looking down towards the sample. The locations of the markers in the 2D camera image were found automatically; the grid points were located manually on every 30th frame. The 2D data was aligned to the 3D data by solving for the camera location using the known 2D and 3D locations of the OptiTrak markers, and initial depth of the 2D grid by approximating the actuator's geometry with a cylinder. The 3D data was mapped to a canonical cylinder by finding the rigid body transformation that minimized the difference between the OptiTrak points and canonical matching points on the cylinder. Bend was calculated by taking the angle between the two markers on the bottom chamber and the two on the top; bend is the angle along the cylinder axis. Extension was calculated by taking the average between each of the points on each chamber and then taking the midpoint between the two separate chambers. The motion capture data for Actuator B is plotted. All data is plotted with respect to the pressure. The sharp slope at approximately 1.4 kPa is due to the slippage of the actuator on the table. The elongation of the actuator is slightly nonlinear with increasing pressure, but this could be due to the slipping of the actuator or uneven air flow from the pushed syringe. Motion captured data of (a) the bend and (b) extension

vs. pressure for a four-chambered actuator. The sharp slope at approximately 1.4 kPa is due to the slippage of the actuator on the table.

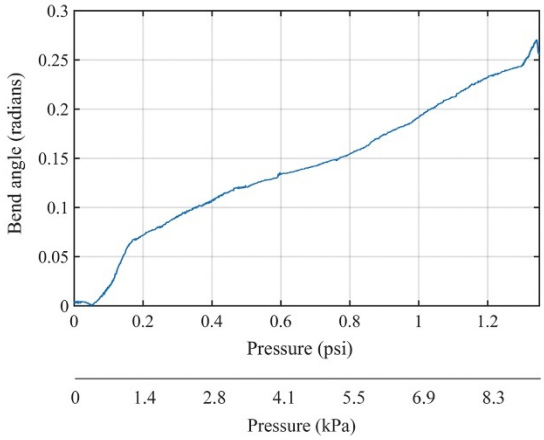


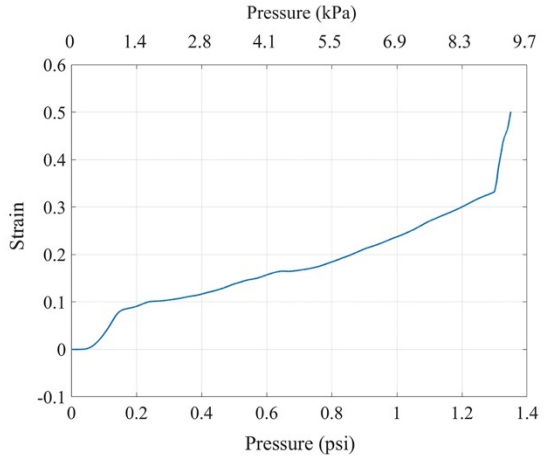


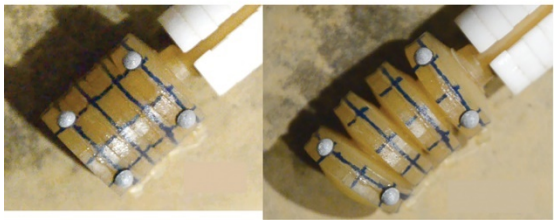

## A.5 Compression Testing

Compression testing was performed on 20 mm diameter circular samples using the Mark-10. Samples were placed on top of sandpaper slightly larger than 20 mm in diameter on top of the bottom compression plate. The top compression plate applied force at a constant rate of 3 mm/min until the center of the sample was reached and then traveled upwards at 3 mm/min to complete one cycle. The first three cycles of compression per sample are plotted. Compression testing is shown in the figure below. The three samples represent the overall spread of data. The samples overlapped and reached force values from 170 N to 246 N at 50% strain.

Compression testing for three samples of different processing conditions and ages. Each sample underwent three compressive cycles at 3 mm/min to 50% of the polymer height. These three samples represent the overall spread of data, and reached from 170 N to 246 N.

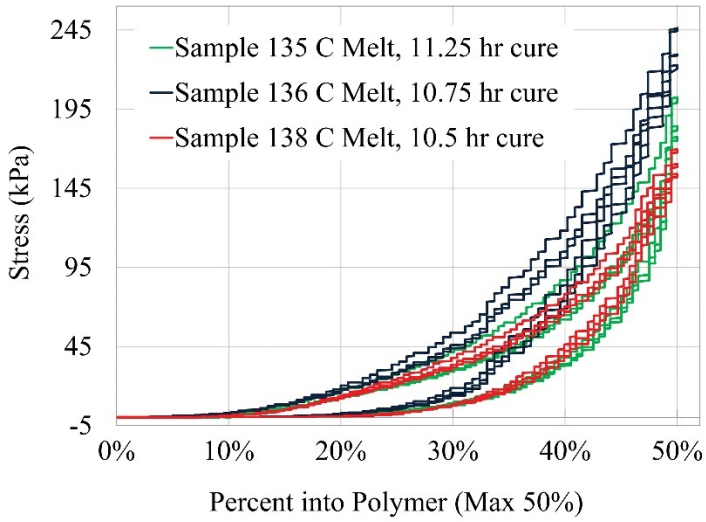

### A.6 CO2 Calculation

Calculation of CO2 release should all CaCO3 dissociate:

Molar mass CaCO3 = 100.0869 g/mol

Ideal mass of CaCO3 going into melt = 0.476 g

0.00476 moles of CaCO3 in = 0.00476 moles of CO2 out = 0.2095 g CO2 out

"19.64 pounds of carbon dioxide (CO2) are produced from burning a gallon of gasoline that does not contain ethanol"

(http://www.eia.gov/tools/faqs/faq.cfm?id=307&t=11)

19.64 lbs CO2/gal burned = 8909 g CO2/gal burned

Assuming your car gets 30 miles/gallon, burn 297 g/mile

297 g/mile / 5280 ft/mile = 0.05625 g/ft

0.2095 g CO2 from polymer/0.05625 g/ft = 3.724 ft

1000 sheets of polymer (approximately 1000 small actuators) = 3724 ft = 0.705 miles

### A.7 Preparation of Natural Latex Rubber and Silicone Tensile Samples

Natural rubber centrifuged latex (in water) from Liquid Latex Fashions (clear) was poured into a sheet mold and left to dry for 5 days. The rubber sheet was then laser cut with the same laser settings as PGS-CaCO3 and in the same size dumbbells as the PGS-CaCO3. The rubber sheet thicknesses ranged from 1.4 to 1.7 mm. 50 wt% Part A and 50 wt% Part B of Ecoflex 00-30 were mixed at 2000 rpm for 30 s and then 2200 rpm for 30 s in a Thinky. The mixture was then poured into the same dumbbell shaped molds as the rubber samples (after mold cleaning) and intermittently vacuumed for 15 minutes in a vacuum chamber to remove any bubbles. The samples

were then placed in a 60°C oven for 20 minutes. After being taken out of the oven, sandpaper was glued to the edges of each dumbbell on each side to reduce slipping during testing. The Ecoflex dumbbell thicknesses ranged from 2.3 to 2.9 mm. There was a slight lip on the outer edges of the dumbbell where the silicone met the acrylic mold, so dumbbell thickness was determined using the center of each sample.

## Paper 2 of 2: Developing a UV-Curable, Environmentally Benign and Degradable Elastomer for Soft Robotics

Jacob Rueben[1*], Stephanie Walker[1*], Stephen Huhn[1], John Simonsen[1], and Yiğit Mengüç[1]

[1]*Oregon State University, 204 Rogers Hall, Corvallis, OR 97331, U.S.A.*

**authors did equal work*

*Published in MRS Advances 2018.*

Abstract

This paper introduces preliminary work on a UV-curable, environmentally benign and degradable elastomer, poly(glycerol sebacate itaconate), or PGSI, for use in soft robotics. A one-pot, solvent-free synthesis route using safe and inexpensive chemical reagents was developed to enable easy adoption into soft robotics labs. Material characterization of non-aged PGSI samples gave: ultimate tensile strength (UTS) ranging from 134 to 193 kPa with moduli ranging from 57 to 131 kPa and elongations at break ranging from 105 to 137 % (12 samples from 6 batches tested), and resilience

values ranging from 73 to 82 % (3 samples from 3 batches tested). FTIR analysis showed a possible decrease in carbon-carbon double bonds after UV curing, evidencing a decrease in itaconic acid methylene groups from photoinitiated free radical cross-linking. NMR on the pre-polymer suggested incorporation of itaconic acid into the main polymer chain and evidence of heterogeneity of the polymer backbone resulting from glycerol bonding. An example molded soft pocket pneumatic actuator is created and briefly characterized. With further development, PGSI can be a degradable material to incorporate into temporary soft robots.

## Introduction

Soft robotics relies on the material properties of elastomers to generate vastly different motion profiles than existing stiff robots (*140*, *193*) and can be used for grasping delicate objects (*194*) or squeezing through small spaces (*195*). The material space for soft robotics, however, has mostly been limited to elastomers that do not degrade. Designing for robot degradability opens soft robotics to new industries reliant on the temporary properties of the elastomer and its components, including environmental or human safety (temporary sensing or medicine), and military stealth technologies (DARPA's ICARUS). Biodegradable and renewable elastomeric materials have recently become a larger area of interest due to their applications in medicine (*171, 196*), and more recently, soft robotics (*197, 198*). Biodegradable polymers of interest include natural rubber, poly(1,8-octanediol-*co*-citric acid) (*171*), alginate-based supramolecular ionic polyurethanes (ASPUs) (*199*), and poly(glycerol sebacate) (*200*). Poly(glycerol sebacate) (PGS), was used as a degradable polymer in

SPA manufacturing due to its relatively simple synthesis process and favorable mechanical properties (*197*, *200*). PGS has been made into a UV curing polymer, poly(glycerol sebacate) acrylate (PGSA) (*201*), enabling fast fabrication from stereolithography (SLA).

However, PGSA uses multiple hazardous solvents along with acryloyl chloride, an acutely toxic chemical, in order to UV Cure (*201*, *202*). The use of hazardous solvents alongside acryloyl chloride introduces health risks to workers synthesizing the material, while also increasing the amount of volatile organic compounds (VOCs) used. Therefore, avoidance of these compounds would increase both workplace and environmental safety of the synthesis. In this work we introduce preliminary work on a UV-curable, degradable, and renewable elastomer for use in soft robotics, poly(glycerol sebacate itaconate), or PGSI, via a one-pot solvent-free synthesis. Itaconic acid, a biobased (*203*) dicarboxylic acid with a terminal alkene (*204*), is compatible with commercial free-radical photoinitiators like 1-hydroxycyclohexyl phenyl ketone (HCHPK), which is used in this work due to its low health risk and 80% biodegradability (*205–207*).

Experimental Details

Glycerol (Fisher Scientific) and sebacic acid (Sigma-Aldrich, 99%) were melted in a 0.16:0.195 molar ratio at ~ 135 to 140°C in a 250-ml round-bottom flask for 20 hours under ~ 100 ml/min of nitrogen. Mixing was maintained at level 1 on the hot plate (IKA C-Mag HS 7). At 20 hours, itaconic acid (Sigma-Aldrich, 99%) was

added to the heated flask in a 0.035:0.16 molar ratio to sebacic acid. At 23 hours, HCHPK (Sigma-Aldrich, 99%) was added (0.89 wt% of the final melt). At 24 hours the melt was poured into the dumbbell mold, a borosilicate glass base with an acrylic layer glued to the top, and scraped to achieve even sample thickness. The UV curing chamber was made with two antimicrobial UV lights with 254 nm wavelength (LSE Lighting) inside an aluminum foil-lined box. The filled mold was left to cool at room temperature for approximately 15 minutes before being placed in the UV-curing chamber. Dumbbells were cured for 1 hour, actuators cured for 2 hours. Each dumbbell was placed on a PTFE baking sheet (Linden Sweden) for storage. The dumbbell shapes were based on ASTM D412 in all dimensions but sample thickness. A pocket actuator was made by sandwiching a PTFE sheet between two poured layers of polymer. Inflation elongation versus pressure is shown for three pocket actuators.

## Tensile and Cyclic Testing

Tensile testing was performed on dumbbells on the same day of creation using a Mark-10 Tensile Tester (25 N load cell) at 500 mm/min. The average modulus in the first 10 % of elongation was calculated. PGSI was compared to a tensile test result of Ecoflex® 00-30 (Smooth-On), a platinum-cure silicone. Cyclic testing was performed on one sample at 500 mm/min and pulled to one third of the average elongation at break of the two tensile samples from the same batch for up to 100 cycles. Hysteresis behavior was analyzed via a stress vs. % elongation plot. The resilience was found using the last full cycle before break. Resilience is the percentage of the energy not lost to hysteresis (area percentage under the loading curve minus the hysteresis loop) (*208*).

## FTIR and NMR Analysis

Fourier-Transform Infrared Spectroscopy (FTIR) was performed on the prepolymer and cured polymer in attenuated total reflectance (ATR) mode using a Nicolet™ iS™ 10 spectrometer (Thermo Scientific). Resulting spectra were compared to identify differences in chemistry pre- and post-curing. All NMR spectra were acquired on a Bruker AVANCE III 700, with an UltraShield Plus Cryostat. A 5mm DCH (Double tuned $^{13}C$ and $^{1}H$) with Z gradient cryo probe was used to acquire Proton, $^{13}C$ with CPD, HSQC, COSY, HMBC and NOESY data. Forward Complex Linear Prediction was employed on the 2D data sets and Backwards Linear Prediction was incorporated in the $^{13}C$ experiments to remove sine-type baseline artifacts in the spectrum. Methanol d4 was acquired from CIL and used as solvent for all samples. Samples containing pure HCHPK were run in amber NMR tubes to prevent photo degradation. Proton and $^{13}C$ decoupled spectra were acquired on two PGSI samples. Standards for chemical shift reference were made for sebacic acid. glycerol, itaconic acid and HCHPK and a mass scaled mixture of the four compounds were all dissolved in d4 methanol and typical proton and $^{13}C$ spectra were observed. All chemical shifts were reference to 3.31 ppm in the proton and 49.15 ppm for $^{13}C$.

# Discussion

## Tensile and Cyclic testing

UTS values of dumbbells ranged from 134 to 193 kPa, and elongations ranged from 105 to 137% at break (Fig. 1-I). Calculated modulus values in the first 10% of

elongation ranged from 57 kPa to 131 kPa. The variance in the tensile and cyclic testing could stem from the varying temperature of the melt or from molding conditions. Cyclic tensile tests of three dumbbells from different trials show hysteresis, with resilience values ranging from 73 to 82%. The hysteresis curves show evidence of viscoelasticity, with permanent deformation occurring during the first cycle (Fig. 1-II).

## FTIR and NMR Analysis

FTIR analysis was conducted on both the uncured pre-polymer and the cured polymer of four PGSI batches. Results from one trial is shown in Fig. 2 for simplicity. The main difference between the uncured and cured spectra is the loss of a small peak at 1635 $cm^{-1}$. This peak aligns with the stretching vibration peak of a carbon-carbon double bond (*209*). The decrease in peak intensity at this wavelength suggests that carbon-carbon double bonds are being broken during the curing process. Because itaconic acid is the only chemical used with a carbon-carbon double bond, and the photoinitiator used attacks points of unsaturation via radical activation (*204*), it is likely that the depleted peak seen in Fig. 2 is a sign of the photoinitiator radicalizing the itaconic acid methylene groups in the process of free radical cross-linking. The strong carbon-oxygen double bond can most likely be linked to the peak at 1750-1700 $cm^{-1}$ adjacent to the possible C-C double bond peak (between 1680 and 1600 $cm^{-1}$) (*209*).

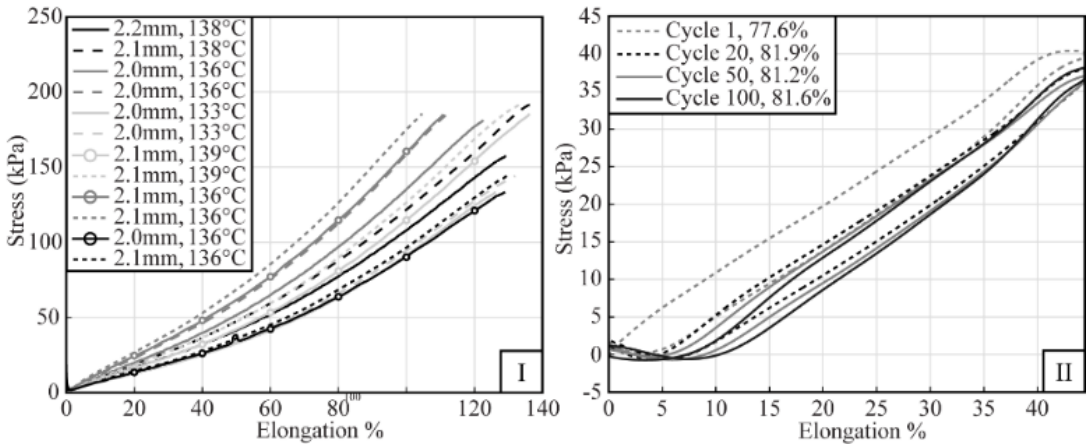


**Figure 1. I:** Tensile tests of six PGSI trials, each with two dumbbells. Trials of the same batch are the same color. All data were filtered using a moving average with a span of 5 points. Legend lists (in order): dumbbell thickness, average temperature of run. **II:** Example cyclic test result with 100 cycles on one sample. Legends list (in order): cycle number, % resilience. All cyclic data was processed with a 4th degree Butterworth filter.

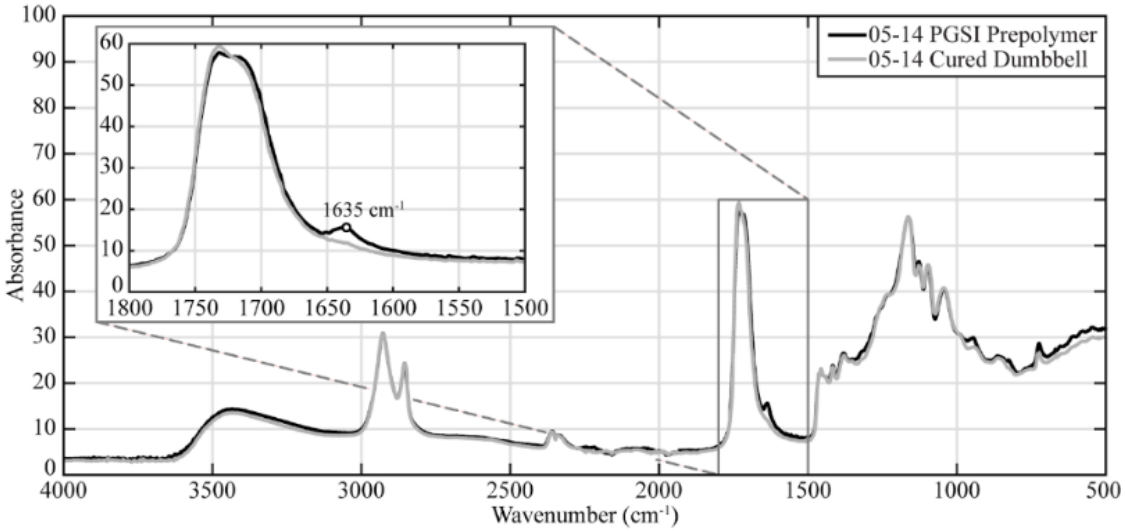


**Figure 2:** FTIR analysis of an uncured pre-polymer sample and a cured polymer sample. The most notable difference between the spectra, the peak at 1635 $cm^{-1}$, is labelled in the inset.

The carbon-oxygen double bond peak contributes to low peak separation in the area of interest, making it difficult to draw definitive conclusions on the uncured and cured structure of PGSI with FTIR alone. A snapshot of the NMR analysis is shown in Fig. 3. The vinyl carbon and proton resonances of itaconic acid are both in non-overlapped spectral regions and resolved to baseline, corresponding to a pair of doublets at 6.28 ppm at 5.74 ppm respectively (lower spectrum Figure 3A). The resonance at 5.74 ppm occasionally appears as a quartet depending on shimming. The protons correlate to a 128.93 ppm $^{13}C$ resonance in the $^{1}H^{13}C$ HSQC (Hetero-Nuclear Single Bond Correlation) (data not shown). These values are in good agreement with published NMR spectra (*210*) and with our own determination from the neat itaconic acid in d4 methanol. In Sample 1 and 2 of PGSI we observed two new resonances at slightly lower frequency – 17 hz for the signal at 6.28 ppm and 25 hz for the signal at 5.74 ppm.

We assign these signals as vinyl protons incorporated into the PSGI. We can then directly determine the amount of itaconic acid incorporated into the polymer chain to the amount of unreacted material. The ratios are approx. 0.61 for the PGSI-1 and approx. 0.82 for PSGI-2. This data is in good agreement with the processing and starting mass for each sample. The $^{13}C$ spectra in Figure 4B show that Sample 1 and 2 both contain a series of new $^{13}C$ resonance signals that do not occur in any of the starting materials. As the chemical shift in the region of the $^{13}C$ spectra is frequently associated with C-O bonds, we assign these new peaks as evidence of heterogeneity of the polymer backbone resulting from the incorporation of glycerol.

Actuator example

Pocket actuators were created to show PGSI in a soft robotics context (Fig. 4). Under pneumatic actuation from 0 kPa until break, elongation reached over 200% from the flat actuators and pressure at break exceeded 15 kPa. This is promising for future applications in soft robotics.

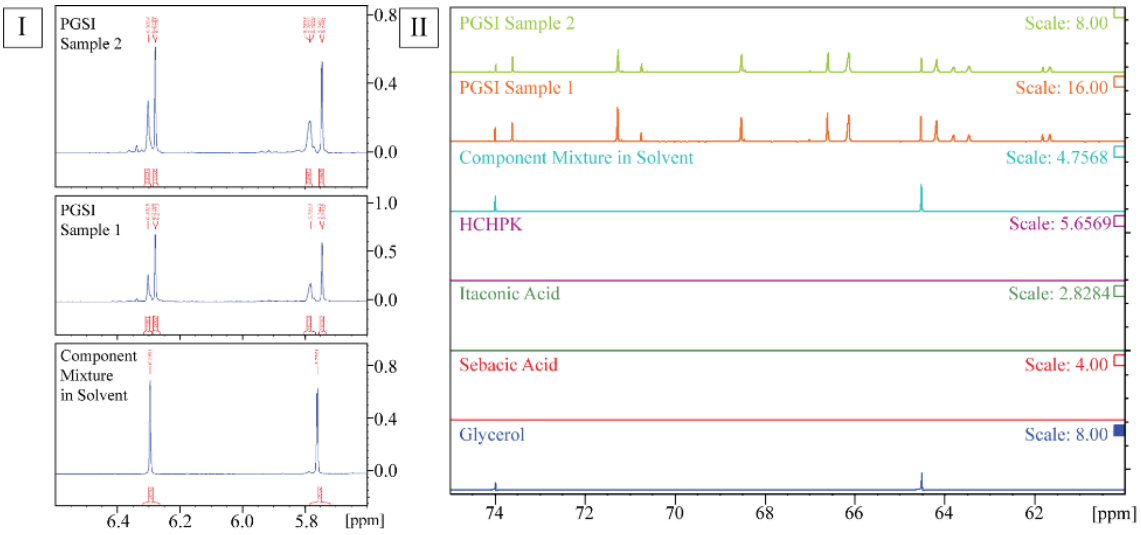


**Figure 3. (a)** NMR results show ratios of the amount of unreacted itaconic acid to the amount included in the polymer chain (approx. 0.61 for the PGSI-1 and approx. 0.82 for PSGI-2), and (b) evidence of heterogeneity of the polymer backbone that is resulting from the incorporation of glycerol.


**Figure 4.** Example actuator for use in soft robotics with brief characterization of 3 actuator elongations with air pressure.

Conclusions

UV-cured PGSI shows promise as an alternative for similar UV-curing biodegradable elastomers such as PGSA with a 0.20 degree of acrylation synthesized by Nijst et al. (*201*). The use of itaconic acid drastically reduces the potential hazards of the monomers (*202*, *211*). Variations in the mold and melt temperature may account for variability in the data which will be improved in future work. Changing the degree of acrylation and assessing the molecular structure further in PGSI is planned. Degradation testing will be performed to elucidate the byproducts of degradation and confirm biodegradation specifically. Exploration of solvents to reduce the viscosity of the polymer for ultimate uses in 3D printing is planned. In this work we have introduced a UV-curing, degradable, and renewable elastomer, PGSI, and have characterized it for use in SPAs. Further work in analyzing strain in the actuators is planned. This research was prompted by difficulties in similarly formulated thermoset materials (*197*), and health concerns in similarly formulated UV-curing materials (*201*). Soft robotics will benefit from the one-pot synthesis method and simple equipment assembly. We hope that this work encourages materials scientists to develop more biodegradable elastomers for soft robotics.

Acknowledgements

The authors thank Dylan Sures for equipment training, and Mari Domingo for her help running the synthesis.

# 3

# Zero-Support 3D Printing of Thermoset Silicone via Simultaneous Control of Both Reaction Kinetics and Transient Rheology

**Notes on Chapter 3**

This work discusses how the use of transient material properties can advantageously be used to create better 3D printed soft robots. Characterization of both rheology and curing kinetics in a silicone elastomer allows for better understanding and control of our custom-made silicone printer. Direct extrusion of a curing silicone fluid requires the knowledge of how fast the silicone is curing and at which point the silicone may clog the system. In this printing system a syringe pump is chosen that can handle the forces required to extrude the high viscosity silicone through fluid lines ending in a high resolution nozzle (below 500 μm). This system uses an in-line mixer that takes fluid Part A and fluid Part B of a platinum-curing silicone formulation. Once the two silicone fluid parts begin to mix, curing takes place. This curing is also accelerated via increase in temperature.

The understanding of transient material properties in the curing silicone can improve print quality via (1) optimization of the stiffness of the silicone before the next layer is deposited, and (2) improving print quality by ensuring that the curing silicone does

not clog the mixer or the nozzle. Here, the material characterization is integral to proper functioning of the additive manufacturing system. By determining the yield stress ($\sigma_y$), the elastic modulus ($G'$) via rheological testing and the heat flow of the curing fluid via differential scanning calorimetry a general model is created to bound the printing times of the custom silicone formulation at the printing temperature (30°C). These methods can be applied to many curing thermoset systems to determine and improve printability. These methods have not yet been used within the soft robotics community.

Authors:

Stephanie Walker[1,2]*, Uranbileg Daalkhaijav[3], Dylan Thrush[4], Callie Branyan[2], Osman Doğan Yirmibeşoğlu [2], Gina Olson[2,4], Yiğit Mengüç[5]

1. Oregon State University, Materials Science, Corvallis, OR, 97331, USA.
2. Oregon State University, Collaborative Robotics and Intelligent Systems (CoRIS) Institute, Corvallis, OR, 97331, USA.
3. Oregon State University, Chemical, Biological, & Environmental Engineering, Corvallis, OR, 97331, USA.
4. Oregon State University, Mechanical Engineering, Corvallis, OR, 97331, USA.
5. Oregon State University, currently at Oculus Research, Redmond, WA, USA.

*Submitted to 3D Printing and Additive Manufacturing. Under Review.*

Abstract

This paper presents a framework for using isothermal curing kinetics and transient rheological data to 3D print a curing thermoset silicone without support. These data

are used to determine time and temperature boundary conditions for amount of curing during extrusion and layering of the print. From the time of mixing, rheological data show how the elastic modulus and yield stress grow as the number of crosslinks increases. The kinetics data show changes in the rate of curing of the silicone. Time boundaries for stages of transient curing are reported from heat flow, yield stress, and G' at the printer operating temperature. These times are used to prevent clogging of the mixing nozzle and ensure layering of unsupported elastomeric silicone. Several models are 3D printed to show the successes and drawbacks of the method within equipment limitations. This framework can be applied to help bound the printable region of other reactive thermoset materials in mixed extrusion systems. By printing without support, this method can produce complex hollow structures which require minimal post-processing.

## Introduction

Direct extrusion 3D printing of silicones enables the creation of customizable soft devices. Several previous solutions in direct extrusion 3D printing of silicone have been developed for research purposes (*11*, *20*, *21*, *31*, *32*, *34*, *62–66*, *70*) and commercial products/services (*50*, *57–61*). Silicone elastomers provide the benefit of inert chemistry once cured and potentially highly stretchable behavior depending on formulation. 3D printing as a fabrication method enables customizability, and with a wide range of material properties to choose from, especially with 2-part room temperature vulcanizing (RTV) silicones, optimizing these printing systems to take advantage of these properties is desired.

Ultimately, the properties that make silicone thermosets desirable for soft devices (high elasticity, low stiffness) also make direct extrusion 3D printing with these silicones difficult. Their inherent softness can make the layers deform during printing. One solution for the softness or low viscosity is to print these fluids with sacrificial support material or in a support bath (*13*, *43–45*, *50*, *212*). But, development of printing strategies without the use of a bath is important in situations where enclosed air voids are needed, or where drainage of the bath material may be difficult or impossible. 3D printers have also been designed that mix multiple materials together while extruding (*11*, *20*, *32*, *213*). These methods can make the printing process additive both in chemical and physical composition. In this work, mixing is used to incorporate reactive silicones into the 3D printing process.

For 3D printing of structured fluids like silicone elastomers, emphasis is placed on tailoring the rheological properties of the extruded material to achieve the desired processability and print fidelity (*214*). Yield stress $\sigma_y$, elastic modulus $G'$, and shear thinning characteristics are commonly characterized as key parameters describing viscoelastic fluid behavior. To our knowledge, no curing kinetics characterization exists for the transient material properties of the popular Dragon Skin silicone system from Smooth-On, especially for a 3D printer with a mixing extruder. Previous research has also not revealed methods for controlling the transient curing properties of these two-part RTV silicones to make better 3D prints. Characterizing the amount of cure versus rheological properties like $G'$ and $\sigma_y$ makes it possible to ensure fluid-like behavior as the material is being extruded and solid-like behavior after extrusion

in a reactive polymer system. Ensuring solid-like behavior after extrusion enables 3D printing of complex models with overhangs and hollow features, without the use of support.

However, the characterization of transient curing and structural properties for reactive materials in mixed extrusion systems has been limited. Using a heated build chamber for increasing stiffness in a fluid print is noted as a solution to prevent collapse of the structure (*215*). However, characterizing transient rheological properties that occur when 3D printing a curing material have not been the focus of previous work. A common strategy is to increase the cure time of the silicone via cure retarding additives or plan to extrude quickly before material properties change (*21*, *63*, *213*) . But, by tracking and using the transient curing behavior inherent in these two-part RTV silicones, longer print times and more stiffness during printing can be achieved. While reactive fluids are curing, especially in a heated environment, their $\sigma_y$ and $G'$ will vary based on time and (potentially) temperature because of the development of crosslinking in the polymer(s). Characterizing this transience better describes the behavior of heated thermoset polymer(s) while printing and creates opportunities for better print quality.

In this work, we present a framework for determining the optimal time and temperature boundaries for a 3D printing system with mixed thermoset silicone. This framework is built upon the translation of rheological and curing kinetics data into time and temperature boundary conditions for a reactive thermoset silicone printer. A

two-part platinum cure silicone elastomer is 3D printed at a high resolution comparable to current thermoplastic printing technology (approx. 500 μm). Our printer environment is temperature controlled with an in-line mixer just before the extrusion nozzle. We utilize rheological characterization to determine the transient growth of the thermoset polymer's $\sigma_y$ and $G'$ then compare this behavior to isothermal curing kinetics to bound the time and temperature ranges for the best amount of crosslinking in our custom 3D printer. Resulting printed sample geometries are used as a demonstration of the applicability of the framework for soft components and actuators. Using kinetics and rheology helps bound the space for equipment needs, speed of extrusion, and if needed, temperature variation to print objects with overhangs, high aspect ratios, and hollow cavities. This method also opens up opportunities for internal void patterning and bulk material elasticity control.

## Materials and Methods

### Formulation

The silicone formulation used by weight was: 87.3% Part A (or B), 0.98 % Thi-Vex, 9.8% Silicone Thinner, and 1.96 % Silc-Pig Dye (all from Smooth-On). Figure S1 (Supporting Materials) gives more information about the development.

### Curing Kinetics Characterization

Isothermal curing kinetics experiments were performed on a DSC Q2000 (TA Instruments). Part A and Part B components were mixed in a 1:1 by weight ratio a Thinky AR-310 Planetary Centrifugal Mixer for 15 seconds at 2000 rpm and then 15

seconds at 2200 rpm. Each mixed sample was then loaded via syringe into an aluminum hermetic pan and sealed with a lid. Sample masses ranged from 10.4-13.1 grams. The sealed sample was placed into the pre-heated furnace at approximately 2 minutes from when mixing ended because of the time taken to load and clamp each sample. The chamber environment was flooded with a nitrogen atmosphere at 50 mL/min. Each sample was heated until the heat flow signal did not change for at least 3 minutes. Three samples were run at each temperature (25°C, 30°C, 35°C, and 40°C) and their resulting heat flow versus time data were averaged per temperature. To connect the curing behavior to the heat flow results from the DSC tests, it is assumed that each bond releases the same amount of energy in an exothermic reaction and that heat flow is proportional to the number of crosslinks being formed (*95*). The baseline for each heat flow curve was determined via the average value of the last three minutes of data for each temperature.

## Rheological Characterization

All rheological characterization was performed on an AR2000ex rotational rheometer (TA Instruments). Preparation of the mixed silicone was the same as the curing kinetics tests described above in order to ensure similar starting points for reactivity. The sample was prepared and spread in-between the pre-heated 40 mm parallel plate geometry by approximately 2 minutes from the end of mixing. The curing tests were performed as oscillatory shear tests with 0.5% strain and 10 rad/s angular frequency. Cure tests were run in triplicate at each temperature (25°C, 30°C, 35°C, 40°C) until the G′ and G″ data began to plateau.

The following rheological tests were run at a smaller temperature range (30°C, 35°C) for our custom 3D printer system. $\sigma_y$ was determined via a stress growth test at a constant 0.02 $s^{-1}$ shear rate. Time windows for 30°C and 35°C $\sigma_y$ tests were approximately 140 and 180 seconds, respectively. The tests were started at increments of 1 minute up until the sample data did not show yielding. Each incrementally larger start time test used a fresh sample. $\sigma_y$ is reported as the first local maximum in oscillatory shear stress before test completion. The sample was not sheared until the specified start time was reached.

Normal force was tested by loading a mixed sample into the rheometer, bringing the geometry down to a 1 mm gap, and compressing the sample at 1 μm/s until a gap height of 900 μm was reached. This test was started at different times (increments of 1 minute up until the normal force neared the limits of the machine). The sample was not compressed until the specified start time was reached. Layer height held above a deposited portion of silicone was calculated using the normal force data by translating the information into a height of silicone using geometry (40 mm wide disk with height of 1 mm) and average density. Density (1.06 g $cm^{-3}$) was calculated by averaging the reported densities from each component's technical document based on weight percent of each component in the formulation.

Printer Setup

Part A and Part B were each loaded into a separate syringe, placed in the syringe pump, and connected to the fluid lines. The mixer was removed and cleaned and the syringe pump was run at 1 mL/min for approximately 3 minutes. Then a new nozzle was attached and the flow rate on the pump was brought to 0.2 mL/min for 2-8 minutes followed by a 0.0385 mL/min equilibrium flow rate. Measurements of the flow rate coming out of the nozzle at 30°C were performed multiple times and averaged to estimate an actual flow rate of approximately 0.063 mL/min. The printer consists of a Taz 6 (Lulzbot) gantry inside of a heated chamber. The custom extruder attaches to the Taz 6 thermoplastic extruder. The reamer is a mixture of auger and vertical indentation geometries. The bottom of the mixer accepts the two silicone inputs and mixes them together using the reamer turned by a small DC motor. Adequate mixing was determined when two contrasting colors blended with no streaking.  Plans for building this custom machine are available via our lab website.

The silicone was tested in the extrusion system at operating temperatures from 30°C to 35°C to determine the maximum operating temperature. Temperature in the enclosure was measured via a thermocouple attached to the printer gantry near the middle of the enclosure. Testing consisted of trying to extrude the silicone with the mixer running once the printer had reached the set temperature. Maximum operating temperature was determined when the flow of the silicone was smooth and consistent, without the filament extruding in irregular shapes due to over-curing.

Printed Line Characterization

Line width and height characterization were performed on a ZeScope Optical Profilometer at 5x magnification. The boundary where the scan did not reflect was assumed to be the start of the silicone filament edges, and the height was determined via maximum z value. Filaments were printed at 600mm/min approximately 1 mm above the glass plate to ensure no deformation took place from the nozzle pressing into the lines. For each temperature, the heated chamber, build plate and glass plate were at the set temperature for at least 20 minutes before printing. Filaments were extruded at temperatures of 26°C, 28°C and 30°C to ensure no clogging would take place.

## Spanning characterization

Spanning characterization was performed by printing filaments across a 5 mm high triangular rig. The speed of travel of the extruder head was 600 mm/min. The rig was placed so that the filaments were printed at a 90° angle from the base of the rig. The triangular gap of the rig ranged from 1-30 mm. Each filament was measured for spanning distance across the gap and vertical depression from the top of the rig.

## Demonstration Prints

Demonstration prints shown increase in difficulty and include hollow and overhanging geometries. First, an overhang test for overhang angles from 25° to 70° is performed similar in scale to the rest of the demonstration prints. Then, an octopus, a licorice-shaped cylinder, a pyramid with a 30° overhang angle, a hollow eggshell, and a hollow bellows are printed. To print these geometries, the model's sizes were increased (and so each layer time in the model was increased) until a successful print

was completed. A demonstration pneumatic actuator was also printed at 30°C. A pneumatic tube was glued into the model and the actuator was inflated from 0-23.6 kPa. The resulting curvature of the actuator was determined by fitting a circle to the interior curve of the actuator and noting the radius.

## Results

### Optimal Printing Windows

**Figure 1** outlines the overall method to print a thermoplastic silicone. First, a silicone was created that held its shape even if freshly mixed, had a yield stress, and was able to be extruded through a high resolution (335 μm inner diameter) nozzle (Figure 1a). More detail is available in Supporting Materials (**Figure S1**). The size of the nozzle is comparable to sizes of thermoplastic 3D printers.

The cure rate and rheology results for an expected range of operating temperatures (Figure 1b) give important information to immediately eliminate two operating temperatures based on print time. At 40°C, the cure rate is increasing quickly and $\tan(\delta)$ decreases rapidly around 4 minutes. Since the mixer has a residence time of approximately 3.4 minutes, this operating temperature will lead to clogging. At 25°C, the time for each layer to fully cure is too long (almost 40 minutes to total cure at the cure rate baseline), so this option is omitted. From this initial narrowing of temperatures, 30°C and 35°C are worth testing in the printer.

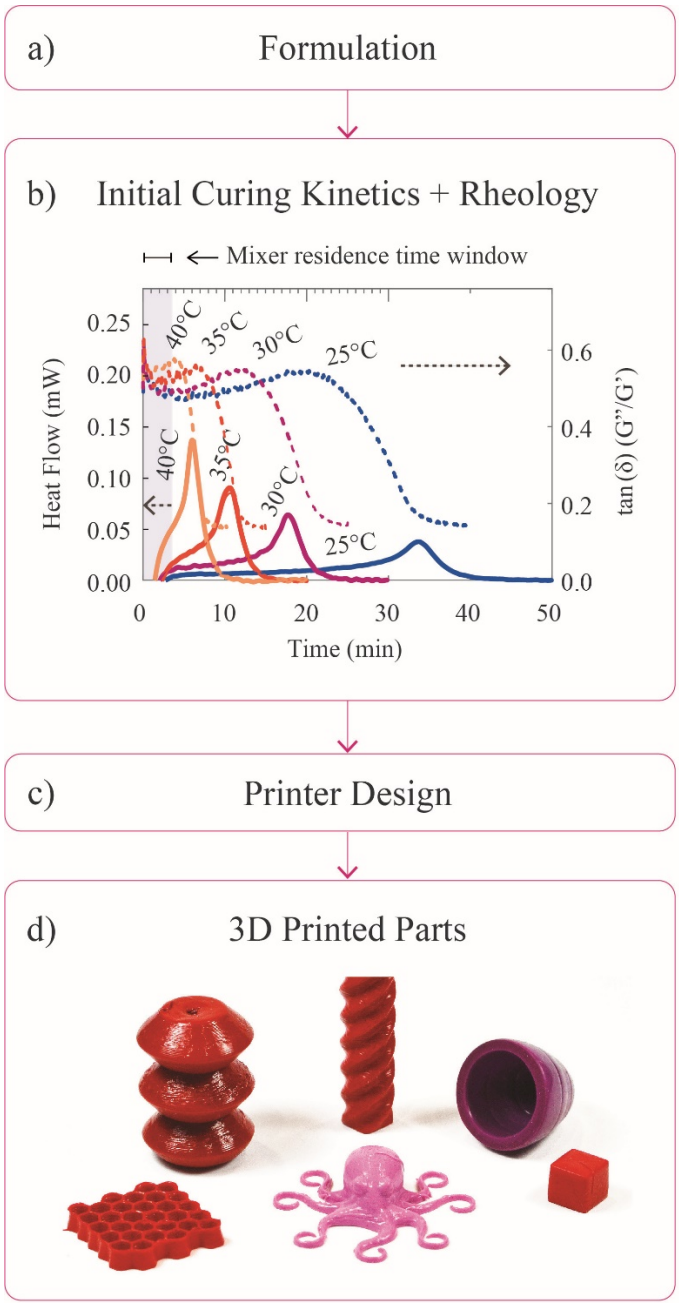


**Figure 1.** Rheological and curing kinetics data is advantageous to use for custom isothermal printer development to determine the highest operating temperatures possible for the machine. Here a flow chart is presented of how rheology and curing kinetics were implemented during the printer development process. First, a silicone formulation was created that could be extruded through a high resolution nozzle and

that also clearly had a yield stress that would keep filament structure after extrusion. Second, isothermal curing kinetics and rheological testing was performed to get an idea of how the silicone properties change with time. Operating at the highest possible temperature when extruding a thermally curing material decreases print time by increasing the number of crosslinks (and therefore silicone stiffness) while layers are deposited. This increase in stiffness correlates to a higher likelihood of complex geometries (hollow and overhanging without support) being achievable with the system. Third, a printer design was created to accommodate the need for in-line mixing, isothermal heating, and pumping of high viscosity polymers. Lastly, because of all this preparation and characterization, 3D prints with overhangs and hollow regions are possible at resolutions close to traditional FDM printers (~335-500 μm).

The printer design was created to extrude the high viscosity silicone formulation through a 27 gauge nozzle (Figure 1c). When test printing the silicone at 30°C, it readily flows out of the nozzle and the material retains sufficient stiffness for overhangs and layering. When printing above this temperature, the extrusion is irregular, with clogging occurring more quickly than at 30°C. Therefore, the printer was only used at 30°C for all printing experiments. This is partly due to the mixer size, as mixer designs with a smaller volume can extrude more quickly, and therefore potentially operate at higher temperatures. Both the material characterization and the printing tests are important for demonstrating why this temperature works well for this system. At 30°C, hollow structures were printed with overhanging geometry and zero support (Figure 1d).

Analyzing the curing kinetics and rheological characterization at 30°C (printer operating temperature) and 35°C (for reference) gives insight into the transient nature of structural growth of the curing silicone for narrowing of printing time windows (**Figure 2**). Seen in Figure 2a, the cure state of the printed layer can be estimated by calculating the amount of time each layer will take before the next is deposited. This same method can be used for the whole print to determine which region of the print is cured, curing, or uncured. There are several important points from the data that are used in this work to bound the optimal time of extrusion and layering. Briefly, $t_1$ is the residence time of the mixer, $t_2$ is the boundary for solid-like growth in the silicone according to tan(δ) data, $t_3$ is the boundary at which the silicone no longer shows a yield stress in rheological testing in the curing fluid, $t_4$ is the point of maximum heat flow during curing kinetics tests, and $t_5$ is the point of full cure assuming very little or no additional reactivity.

The data from 30°C is analyzed for relationships between the previously stated points of note and time. In order of increasing time, the first notable point is $t_1$, the residence time of the mixer. The residence time of the mixer is calculated using the flow rate and the inner volume (from the level where silicone enters the lower mixer all the way to the tip of the nozzle). The residence time of the mixer should allow the silicone to be extruded before the second point $t_2$, the boundary for solid-like growth in the silicone (from Figure 2b). This point is the maximum value of tan($\delta$) ($G''/G'$) occurring before tan($\delta$)'s rapid decrease. tan($\delta$) is a ratio of the viscous to elastic

behavior of the silicone. When the value is less than 1, the silicone behaves more like a solid than a liquid. In this formulation, the silicone is G′ dominated even in the beginning of the curing process, but the rapid decrease in tan($\delta$) during curing describes the rapid growth of G′ over G″, a signal for the increase in stiffness via acceleration of cure. Data on the growth of G′ compared to G″ during curing for all temperatures tested is shown in **Figure S2**. While good for holding structure of a 3D print after extrusion, a quick decrease in tan($\delta$) should be avoided during mixing and extrusion, where uncured behavior is needed for the silicone to flow through the nozzle. Our mixer residence time is 3.4 minutes, which gives plenty of opportunity for extrusion without a fundamental change in silicone behavior. After $t_2$, difficult prints are more likely to succeed as time goes on due to the silicone's growing crosslinked network. Figure 2c displays the percent growth of G′ after the point of extrusion from its initial value to its value at the end of the curing test. Before $t_2$ there is little to no change in the stiffness of the silicone. The leveling of G′ as time goes on also signifies a near full cure, and matches well with the heat flow baseline data. The growth of G′ also affects spanning behavior. In this system, the spanning lengths of the filaments are limited because G′ stays in a similar range until $t_2$ (11.1 minutes). For 2 – 12 mm gaps, the polymer has a 0.2 mm – 1.7 mm sag distance from the horizontal (**Figure S3**). Sag distance can be designed based on the acceptable range of deviation from the STL model.

Points $t_3$ through $t_5$ are useful to know depending on how much stiffness is needed before the next layer is deposited. Each time interval between extrusion and full cure

can serve different purposes depending on the print. Shorter prints, prints with large wall thickness, and prints with vertical walls are able to stack effectively right after extrusion due to the ability for the silicone to self-support with surrounding layers, and the ability of the silicone to hold a few centimeters of vertical height right after extrusion (Supporting Materials, **Figure S4 and S5**). As prints get more complex, especially with overhangs, calculating the time each layer takes to reach an adequate amount of cure is useful to ensure that cure is past the last $\sigma_y$ so that minor disturbances due to the nozzle and filament pressing on the layer do not affect the unsupported 3D shape.

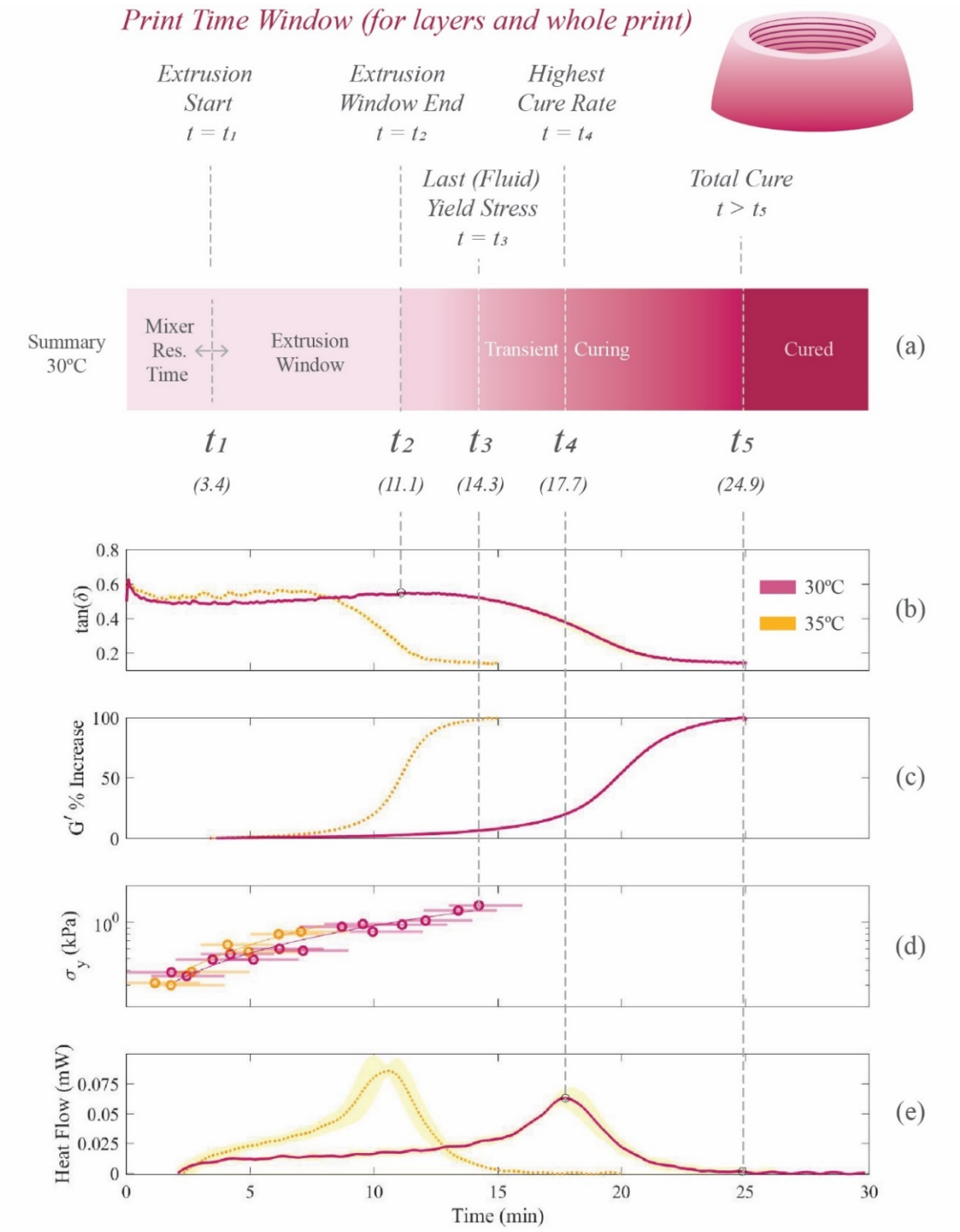


**Figure 2. (A)** The amount of crosslinking in the silicone can be controlled by operating the printer within specific temperatures and times bound with rheological and curing kinetics data. A summary curing gradient for 30°C shows the important

points. From extrusion to cure, several types of prints are possible. Prints in this work were able to hold structure between $t_1$ and $t_5$, with layer time increasing with increasing amount of overhanging geometry. Important points of note are the mixer residence time $t_1$ the point just before the decrease in tan($\delta$) $t_2$, the point of last yield stress $t_3$, the point of fastest cure rate $t_4$, and the final cure time $t_5$. **(B)** The curing rheological data show the behavior of tan($\delta$) after extrusion to cure. The time period just before the decrease in tan($\delta$) ($t_2$) is a good time to extrude the polymer because the G′ does not change much during this time. After this point, the G′ starts to increase and so extrusion will become more difficult because of crosslinking in the silicone. **(C)** The percent change in G′ from its value after mixing is calculated from the point of extrusion to cure. **(D)** The yield stress value of the curing fluid grows as the silicone cures, with the last point representing the last test that showed a yield stress in the curing fluid. The horizontal bars represent the test time range for each yield stress data point. **(E)** Heat flow is directly proportional to rate of cure, with the highest cure rate occurring at the peak in the data. The baseline of the heat flow data occurs when the silicone is cured assuming little or no residual reactions take place.

$t_3$ is the time of last $\sigma_y$ (Figure 2e) of the silicone in the uncured/fluid state. This is the point at which the silicone no longer shows a yield stress during rheological testing of the curing fluid. Detailed $\sigma_y$ data is shown in **Figure S6**. Each data point before $t_3$ in the plot is the yield stress value of the silicone for that specific test start time. So, depending on the print structure, it can be possible to print before $t_3$ if the stress from the deposition of silicone above the previous layers does not exceed the yield stress at

that time. $\sigma_y$ is the stress at which the uncured silicone will begin to deform under shear. $\sigma_y$ measurements can apply to the flow of the fluid through a nozzle, deformation caused by the dragging of the nozzle and extruded filament across the previous layer, and also the sideways flow resulting from the weight of additional layers. Past this point, the silicone is cured enough so that it no longer exhibits yielding behavior. For this reason, once the time of last $\sigma_y$ is passed, the print will have greater success with overhang or high aspect ratio geometry because it is less likely to move under the typical forces applied by the nozzle and silicone weight.

The time of highest rate of cure, $t_4$ (from Figure 2e), is a good time to move onto the next layer if the print needs to be mostly but not fully cured during printing. This could be used in a case where stiffness is needed but a slightly uncured state is required for molecular adhesion between uncured layers. At point of full cure, $t_5$, the cure rate reaches a baseline near the end of the curing kinetics data assuming there are no residual reactions (Figure 2e). The best layer stiffness will occur here before another layer is deposited because the silicone is a solid elastomer. This total cure point is more likely to apply to a region of the previously printed layers than to one layer itself due to the long time until full cure (24.9 minutes). With larger models, this curing window can be quickly exceeded within the first few layers. Overall, this analysis can also be applied to other thermoset materials, so that those designing printing systems can take advantage of the material's transient curing behavior.

Printed Models

3D printing the thermoset silicone formulation was performed between $t_1$ and $t_5$. Within this time at 30°C, increasing stiffness in the silicone occurs via increasing number of crosslinks during curing. The overhang test print gave the limit of overhanging geometry as approximately 35° before sagging takes place that would create unreliable print quality **(Figure 3)**. The print demonstrations display a range of features possible and some of the limitations **(Figure 4)**. The octopus has complex outer features but a small height, and can be printed right after $t_1$. The prints are shown in order of increasing difficulty (Figure 4a) and are also qualitatively compared to their STL models (Figure 4b). The model's G-Code settings are based on line dimensions from profilometry (**Figure S7**). Overhang geometries work well up to about a 35° angle from the vertical as predicted from the overhang test. The pyramid has an approximately 30° overhang which shows no sign of sagging in the model. When viewing the interior cross-sections of the prints, the eggshell and bellows (most difficult) models show that once this angle threshold is passed the print quality can be unpredictable (Figure 4c). Close-up views show good quality surface finish (Figure 4d). Print time for each model is shown (Figure 4e) to compare to the time chart from the rheological and curing kinetics in Figure 2. The transient cure state of both the individual layers and printed model regions can be estimated in order to achieve desired quality within printer limitations. The print quality of more difficult models can be improved by increasing the amount of surface area per layer or pausing between layers. A 3D print of a hollow pneumatic actuator (**Figure 5**) is also shown,

requiring only a glued tube and cutting a few stray strands. The radius of curvature decreases in an approximately linear trend.

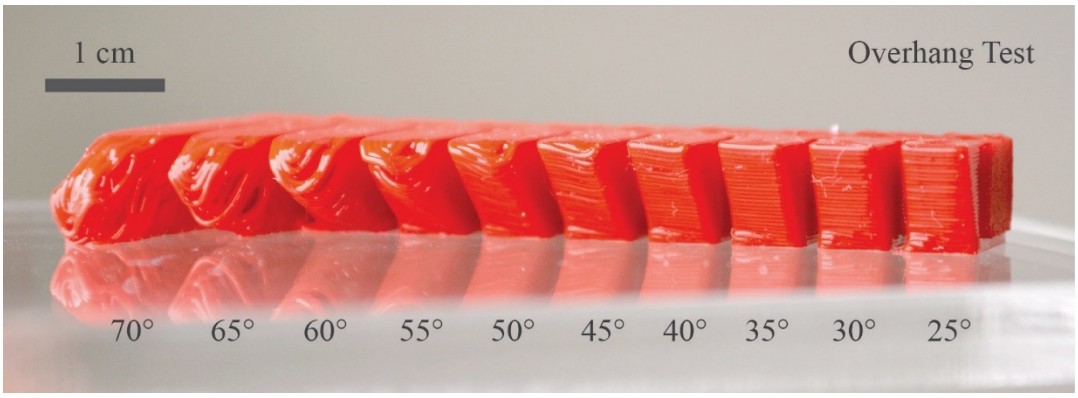


**Figure 3.** The overhang test print shows that at around 40° the print starts to sag slightly with a more obvious sagging at 45°. Beyond this, the silicone does not hold overhanging features at this print size. This data can be used to help determine the limit of printability for overhang geometries in this system.

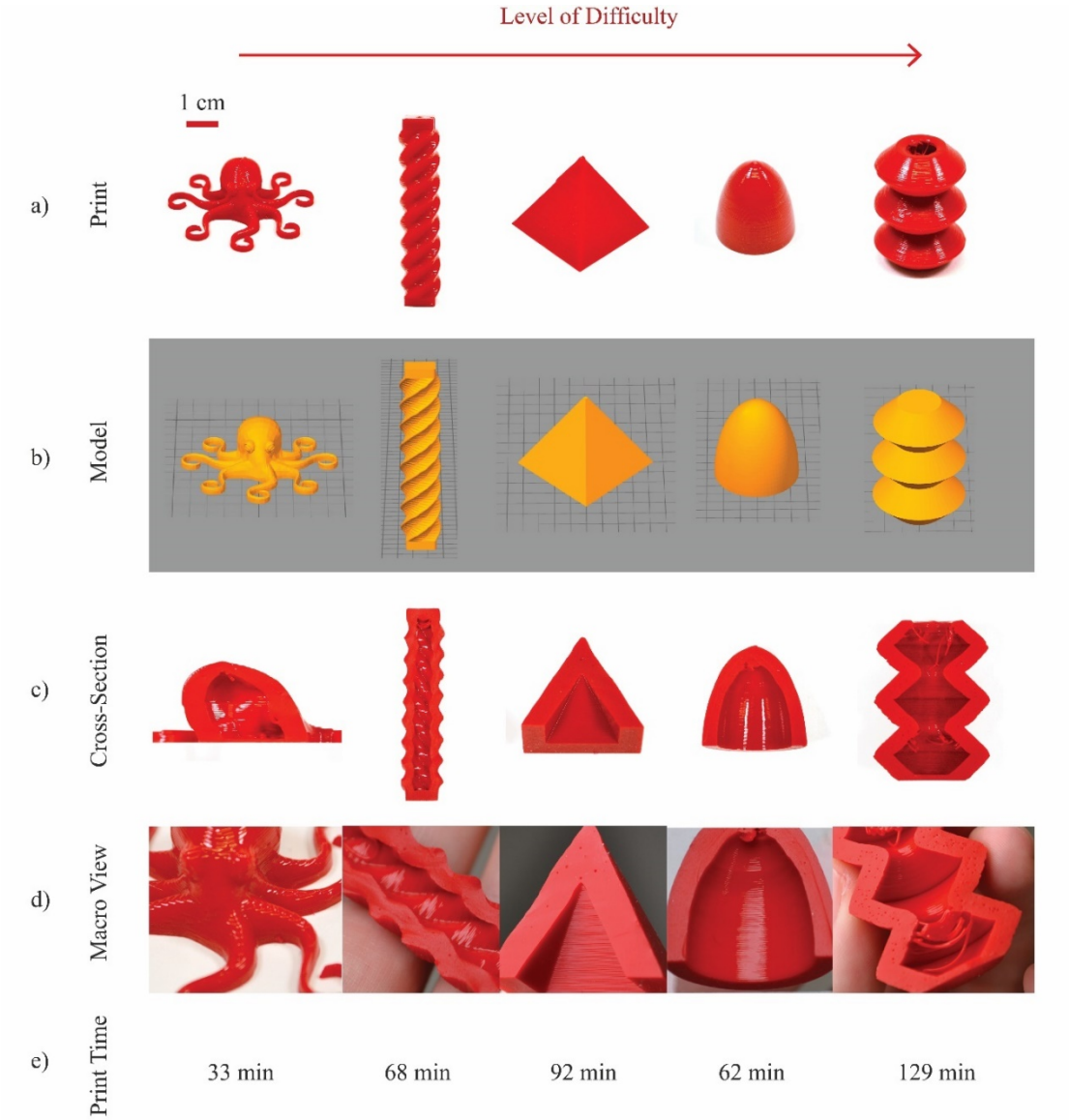


**Figure 4. (A)** Tall, hollow, and overhang prints are possible when working within the time and temperature boundaries specified by rheology and curing kinetics. **(B)** The 3D CAD models are sliced according to line profilometry estimates for the dimensions of the filaments once cured. **(C)** Cross-sections of prints show that overhang and hollow geometries work well up to about a 35° angle from the vertical as predicted from the overhang test. For example, the pyramid has a 30° overhang which holds up until the structure is finished printing. Once the angle threshold is

passed, or if the material does not have enough stiffness due to cure, sagging occurs in the unsupported filaments and the structure collapses. This is especially evident in the bellows structure with its 45° angle overhangs and high spanning lengths on the top of the model. Though the 45° angle is possible to print with some sagging, the results are unpredictable. The licorice and eggshell shaped prints show the same behavior where there is a high overhang angle, where spanning is needed, or where the low surface area in the layer does not give the previously deposited filament enough time to cure before using it as a support system for new filament. **(D)** Macro views show closeups of the print quality. The resolution on this printing system (~ 335 – 500 μm) is comparable to traditional FDM printers. **(E)** Print time for each model is shown to compare to the time chart from the rheological and curing kinetics in Figure 2. As each model is printed, there are areas which are uncured, have transient curing, or are fully cured. To successfully print difficult models with overhangs, the amount of curing either in the layer itself or in the many layers below has to have enough stiffness to prevent deformation due to the weight of the newly deposited silicone.

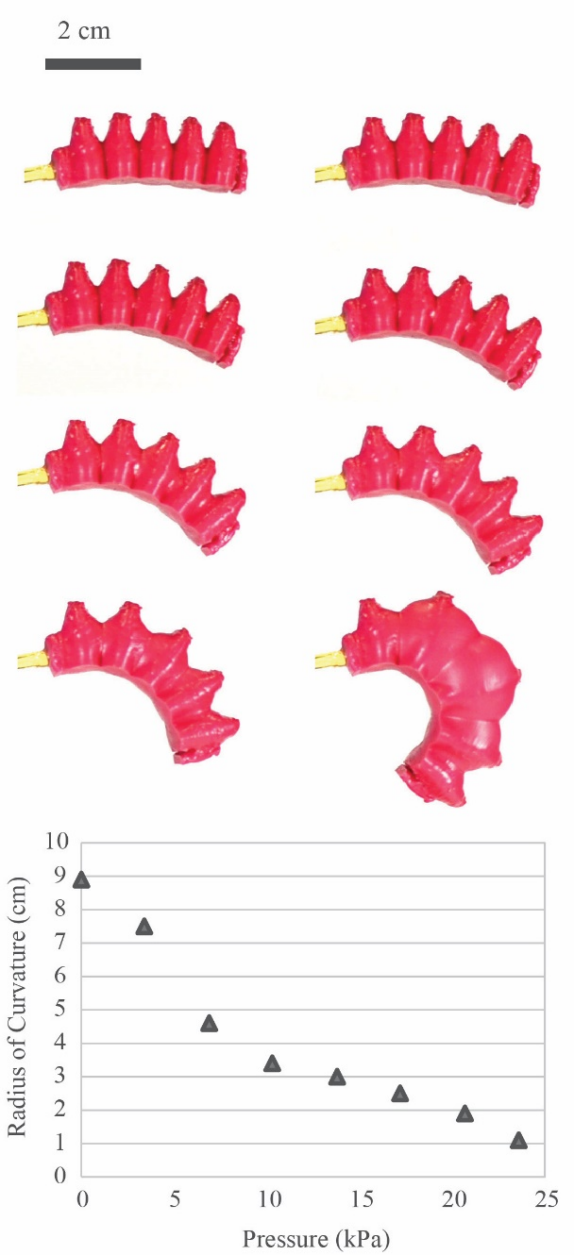


**Figure 5.** Hollow actuators can be 3D printed without the use of support. Here a brief characterization of pressure versus radius of curvature (R) in a bellows-shaped actuator is shown. This actuator is made of a single material and the only post-processing is to cut a few stray strands of cured filament and glue a tube into one side.

## Discussion

The importance of analyzing the transient rheological and curing kinetics behavior of these types of materials for additive manufacturing cannot be understated. Exploring the transient behavior of these materials is integral to the success of the print and to further improvements to the printer system, including the prevention of clogging, sagging, and poorly executed prints in general. To improve the system, a smaller mixer can be designed to decrease the residence time of the silicone for operation at higher temperatures. Future work on this printer will include a full parametric study of overhang angle versus wall thickness, as well as aspect ratio limit tests. The hope is to more fully characterize the geometrical print limits so that the printer can become an open-source plug-and-play system. Currently the transient curing between the $t_1$ and $t_5$ data points is not modeled via a predictive equation and so modeling the curing and correlating it to the resulting print geometrical parameters is also desired. The open-source model, including both the hardware and printing methods, leaves room for continuous improvement and further definition of printer limits for collaborative development in the soft device community.

## Conclusion

In summary, we report a framework for how to 3D print a thermoset silicone by using its transient material properties during curing. This framework is built upon rheological and curing kinetics characterization to determine boundaries for time and temperature in the development of crosslinking in the silicone. Using this method,

several models are printed with a custom Dragon Skin 10 Very Fast formulation which have hollow and overhang geometries without the use of support. This framework expands upon previous work by facilitating the 3D printing of soft elastomeric structures that do not require support material or a fluid support bath. These methods can be applied to several material chemistries to further elucidate the role of rheology and curing in transient material systems for additive manufacturing.

## Acknowledgements

The authors would like to thank the members of mLab for their continued support and production of prototype 3D models for this work. This work was supported by the Office of Naval Research Young Investigator Program (ONR YIP N00014-16-1-2529; P.O. Tom McKenna).

## Supporting Information

### Formulation

The formulation was developed to ensure that the silicone behaved like a gel right after mixing. In addition to the Dragon Skin 10 Very Fast silicone itself, which was chosen because its cure rate at ambient conditions was the fastest available in the Dragon Skin family without the addition of an accelerator, other Smooth-On additives were used to ensure desired behavior. The first additive was a thickener and thixotropic additive (THI-VEX), used at maximum recommended concentration in

the mixture to ensure yield stress characteristics. The second additive was a thinner (Silicone Thinner) used to reduce viscosity and ensure flow through a high resolution nozzle. One might ask: why would both a thickener and thinner be used? An explanation of the qualitative behavior of the formulation is available in Figure S1. When thinner was used in the mixture without THI-VEX, the silicone would flow too rapidly to retain filament structure when printing. When THI-VEX is added with thinner, the formulation still benefits from the lowered viscosity but retains structure after mixing. Without thinner, the silicone is difficult to print with high resolution nozzles. Though the exact chemistry of the silicone formulation is proprietary, this formulation functions well for 3D printing this highly elastic material.

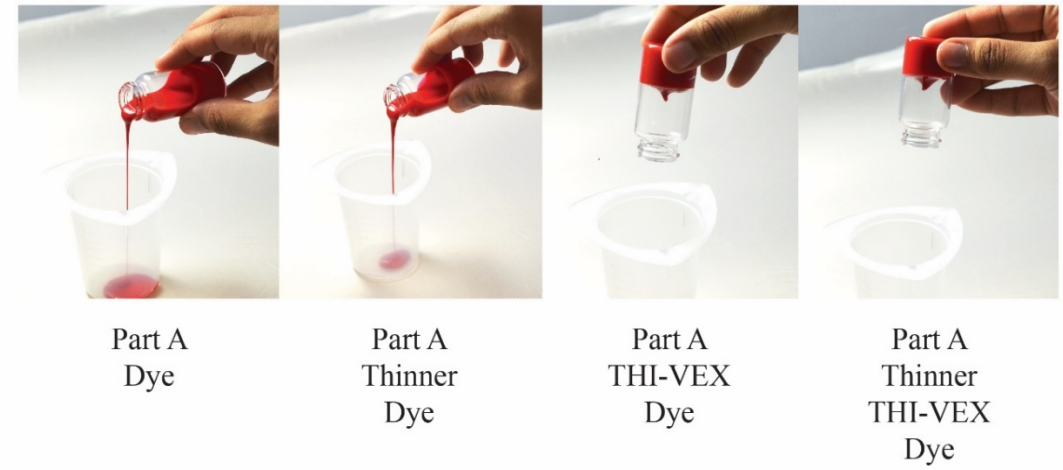


**Figure S1. Formulation differences.** Qualitative differences between additives are noticeable when trying to pour the formulation. THI-VEX serves to increase the gel state of the silicone, and Silicone Thinner is meant to reduce viscosity for extrusion.

Viscous and Elastic Modulus Behavior During Curing

The formulation of the silicone fluid helps retain structure in the print in addition to the temperature increase because the silicone is elastic modulus dominated throughout the printing process. This means that even if the silicone is extruded after short periods of time, the mixture is a gel that will allow for some stacking of layers. The growth of the elastic modulus G′ over the viscous modulus G″ is shown in Figure S2. The growth of G′ over G″ is tracked through tan(δ).

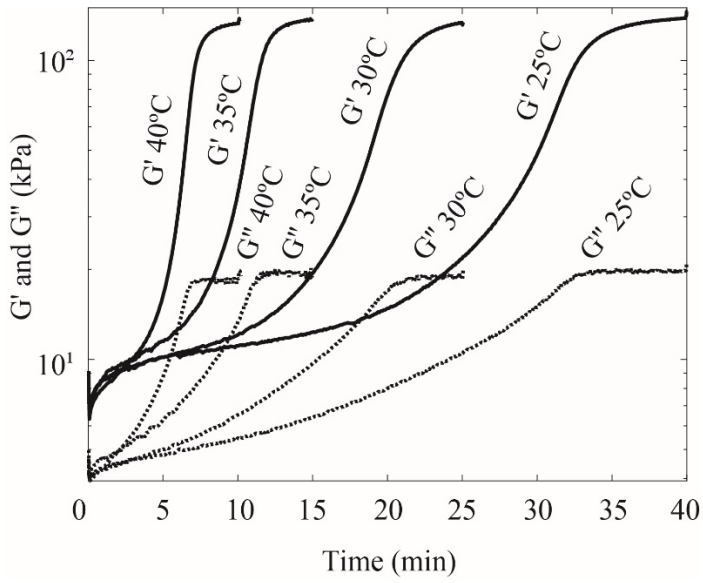


**Figure S2.** The silicone is G′ dominated throughout the curing process, but the structure in the silicone for layering starts when G′ starts to grow faster than G″.

Spanning Tests

Spanning tests were performed within the temperature boundaries of our custom printer (Figure S3). Because the G’ of the silicone between 25°C and 30°C is the same up until the 10 minute mark, the spanning is expected to be similar because the

residence time of the mixer is 3.4 minutes and the silicone is sure to be extruded by 10 minutes. The equation used for this comparison comes from Smay et al. 2002 (*216*). As seen in the figure below, spanning behavior overlaps for all three temperatures. The length of span can be estimated by solving for L in the model.

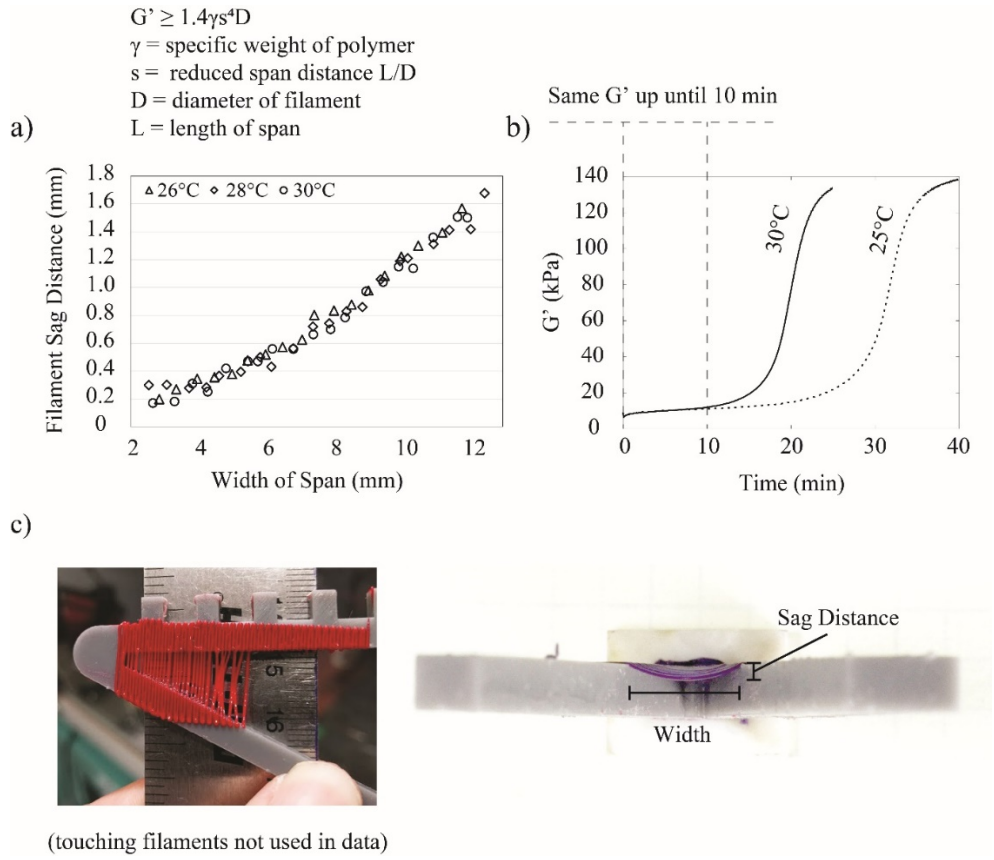


**Figure S3. (a)** The spanning characterization confirmed the assumption that when G′ is the same (here, across 3 temperatures), and the filament dimensions are the same, the spanning results will overlap. (b) The G' value for 25°C and 30°C does not change for the first 10 minutes of testing. (c) Filaments were printed on top of a 5 mm tall spanning rig (photo is an example only, spanning filaments used for data did not touch).

## Normal Force Methods

Normal force testing was performed up until 10% deformation (Figure S4), but 1% deformation is used as an acceptable amount of deformation in a print (Figure S5). In Figure S5, the data points are the value of the equivalent silicone height (calculated from normal force) at 1% deformation, and the dotted lines are the growth of the silicone height values up to that each data point. The purple data is at 30°C and the orange is at 35°C. Polynomial trend lines are shown as predictors of layer height. By the time that the start of the test passes the 8 minutes after mixing mark, in approximately 10 seconds after the start of the test, the amount of silicone that a deposited layer can hold plateaus for 30°C around 10 cm.

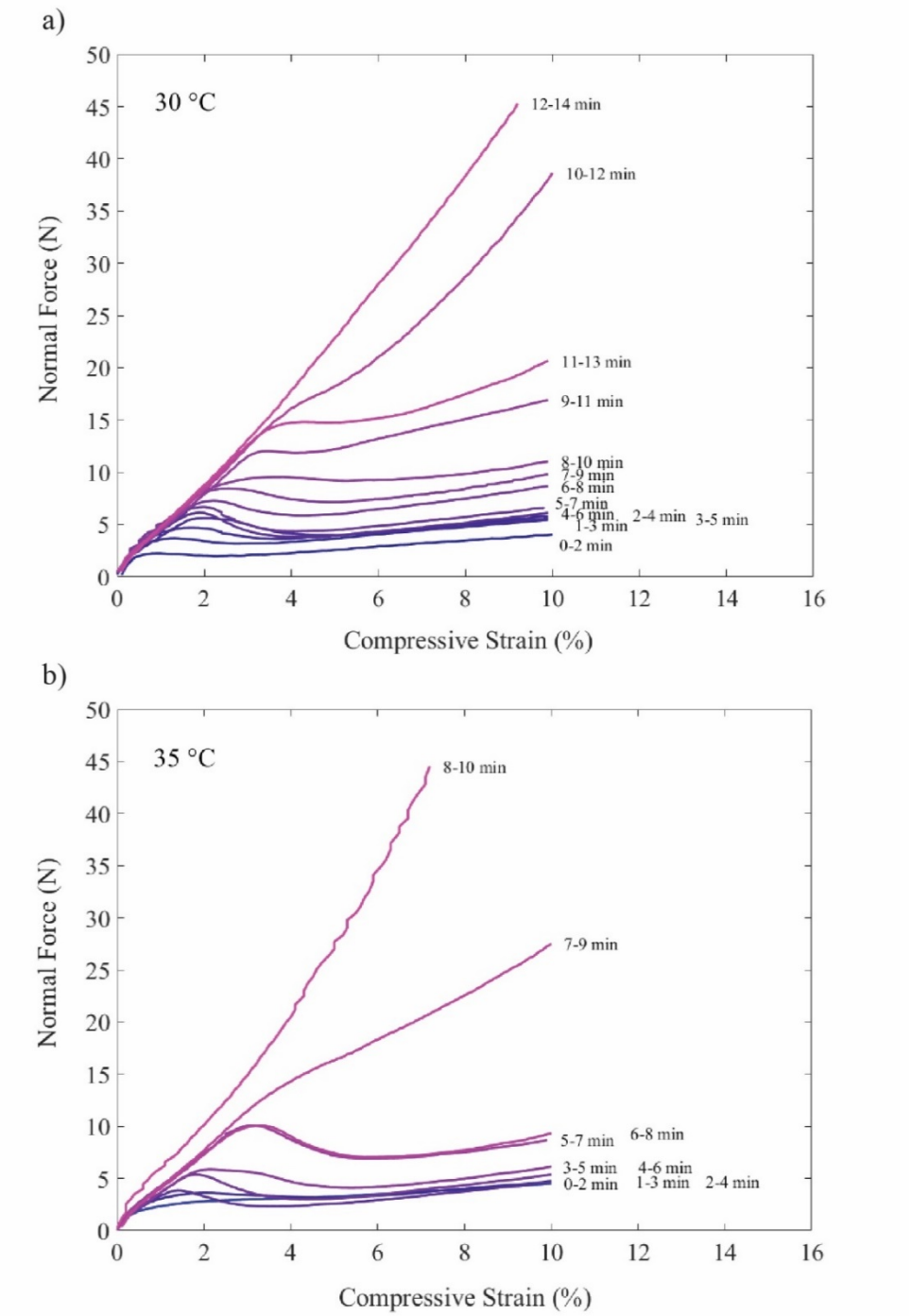


**Figure S4.** Normal force data for 30°C and 35°C tests. Darker colors are tests started closer to mixing, lighter colors are tests started farther from the mixing time. The 25°C and 40°C temperatures were not tested because they would not work well with the printer system.

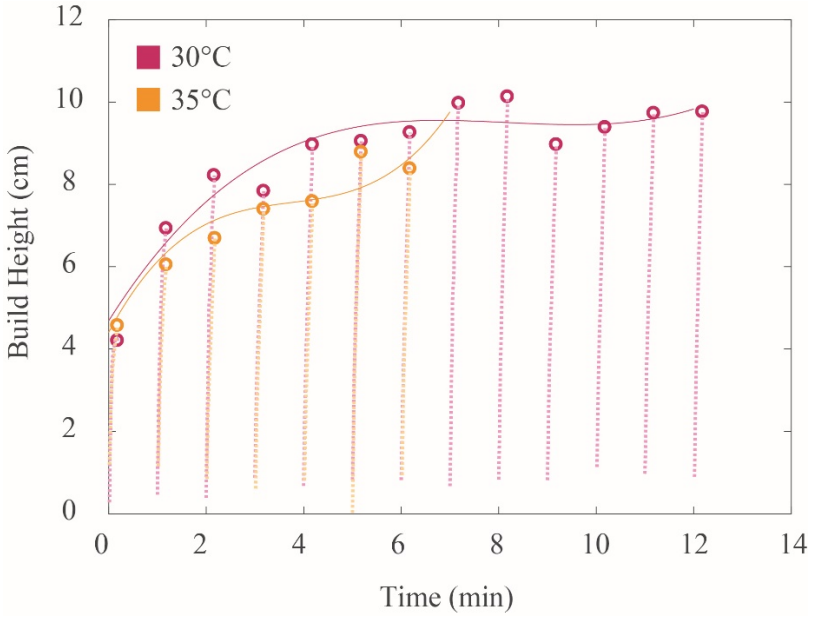


**Figure S5.** Silicone height held based on normal force. Normal force values were translated into silicone height held above the sample via geometry and density calculations described below. The normal force values used in the calculations are from the zero to 1% of deformation (0-10 µm) range in the test. Trend lines were overlaid in attempt to serve as a predictor of weight a layer could hold at these time ranges. The area is the area of the 40 mm diameter parallel plate rheometer geometry. Density is estimated to be 1.06 g/ml based on data from technical document and density averaged by volume percent of each element in the formulation.

$$Build\ Height = \frac{F\left(\frac{kg*m}{s^2}\right))}{g\left(\frac{m}{s^2}\right)} * \frac{Vol\ (m^3)}{mass\ (kg)} * \frac{1}{Area\ (m^2)} * \frac{100\ cm}{1\ m} \qquad \text{(Equation S1)}$$

Yield Stress Methods

Yield stress was determined to be the first local maximum in a stress growth test. Data from 30°C and 35°C is shown in Figure S6. The yield stress values are noted in the data with a star. Samples that did not yield are not shown in the main manuscript.

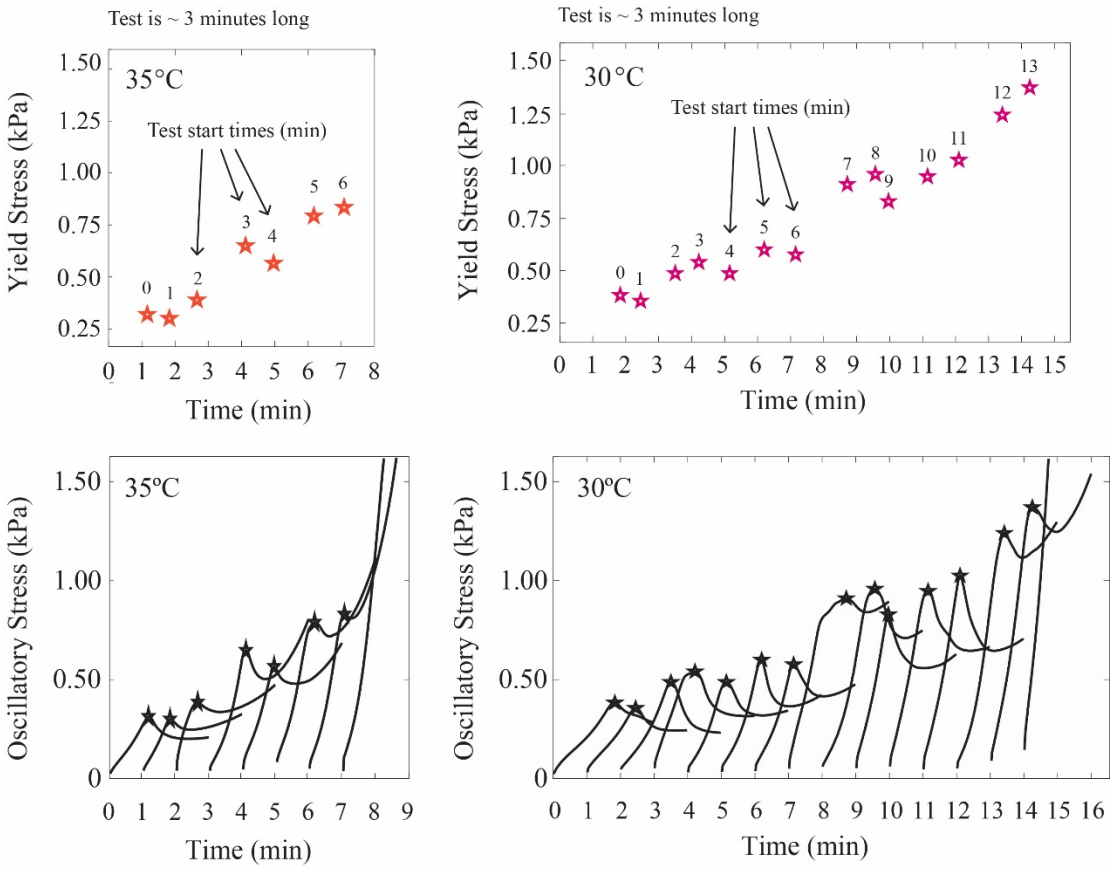


**Figure S6.** Yield stress data was taken using a rotational rheometer for 35°C and 30°C after determining that the silicone would cure too quickly at 40°C for the printer system and at 25°C curing would occur too slowly for practical print times. The yield stress was determined using the first local maximum of the stress curve (starred

points). These data also display the transient nature of oscillatory stress growth in the curing silicone.

Equations for Yield Stress and Silicone Height Graphs

Equations for predicting yield stress and silicone height at a certain time of cure are determined by fitting a polynomial curve to the maxima data. The following equations can be used to help predict the stress or height (normal force) for the system based on manufacturing needs:

Y = yield stress (kPa), x = time (min)

$y_{30} = 0.076042x + 0.16909$

$y_{35} = 0.095912x + 0.16406$

y = Silicone Height (cm), x = time (min)

$y_{30} = 0.0096774x^3 + -0.23719x^2 + 1.8815x + 4.686$

$y_{35} = 0.049379x^3 + -0.55416x^2 + 2.2246x + 4.4062$

Line Height Profilometry

Line profilometry on the silicone shows increasing height with increasing temperature (**Figure S7**). This is indicative of the silicone retaining structure at higher temperatures due to increased cure percent after extrusion. The silicone also tends to flow slightly faster in warmer temperatures, which, along with mechanical vibrations

in the printer, can lead to slight variation in filament diameter when deposited. Unoptimized printed hollow eggshell models in Figure S7 demonstrate the improvement of print fidelity as operating temperature is increased when using the same G-code file. The CAD model is presented for qualitative shape comparison. The hollow egg prints are difficult to print near the top of the model due to the relatively thin wall (2.5 mm) and reduced time between layers which means a more uncured state. However, with further optimization, model geometries and printer paths in G-code can overcome these limitations.

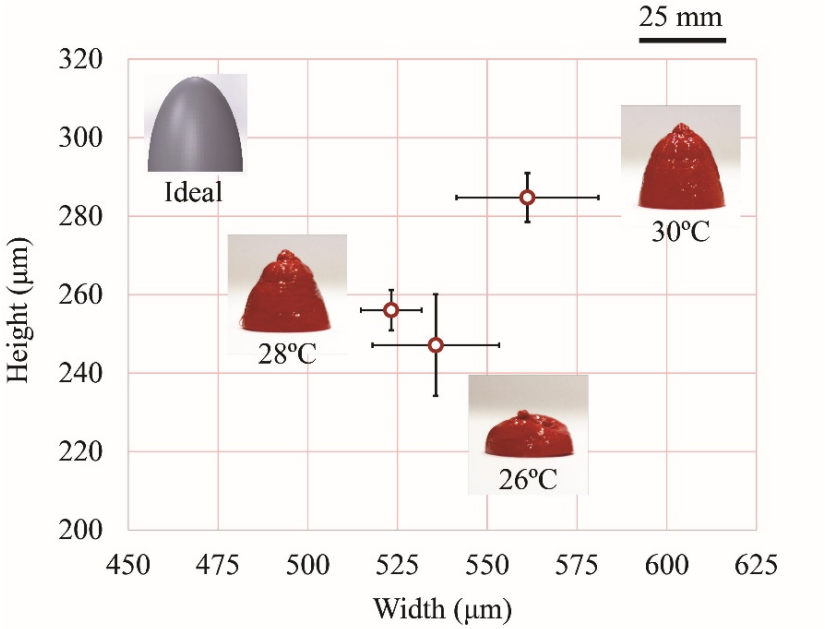


**Figure S7.** Line profilometry performed on silicone extruded onto glass at the same speed (600 mm/min) at 26°C, 28°C, and 30°C show that at 30°C the filament height increases. Width is variable but differences are not statistically significant. This could be due to small mechanical oscillations in the extruder and slight flow variations possible when heating the uncured silicone. These values are used as a basis for starting to choose G-code parameters for filament extrusion width and height. Non-optimized hollow eggshell models were printed with the same G-code parameters as a demonstration of the role that increased temperature plays in improving print quality.

Slicing and G-code

Because this is a continuously extruding material, the extra travel paths where material would retract in a thermoplastic filament system prove troublesome if not

handled properly. 3D structures created with purposeful manipulation of G-code (the computer commands that direct the operation of the 3D printer) ensure that little extra material is deposited on the print and layer height and width are appropriate to the short-term equilibrium position of a printed filament determined via line profilometry testing. Ideally the printing paths of the extruder do not pass over previously printed areas within the same layer.

Printer Setup

The main printer components are divided into the environmental control box and heater system, pump, 3D gantry, custom extruder/mixer, and camera (**Figure S8**). The environmental control box keeps the entire printer environment as isothermal as possible to enable us to match the isothermal characterization data with the resulting print layer behavior. The syringe pump flow rate is constant and is not controlled by any mechanism to start or stop flow. Options to start and stop flow rate or control the path planning in order to improve print quality are left to future work. The 3D gantry is an off the shelf model (Lulzbot Taz 6) with slight alteration of the firmware to accommodate the extruder and nozzle of slightly different size for homing in the z axis. The custom extruder/mixer files are meant to be extremely user friendly and easy to assemble. All of the components are available on our mLab Github site. The camera is a Grasshopper 3 from FLIR and is used as a tool to view high resolution images and videos of the filament as it comes out of the nozzle and spreads onto the print. With the camera it is easier to diagnose print problems (slowing of flow due to clogging, improper alignment, improper layer height, etc.).

(a)

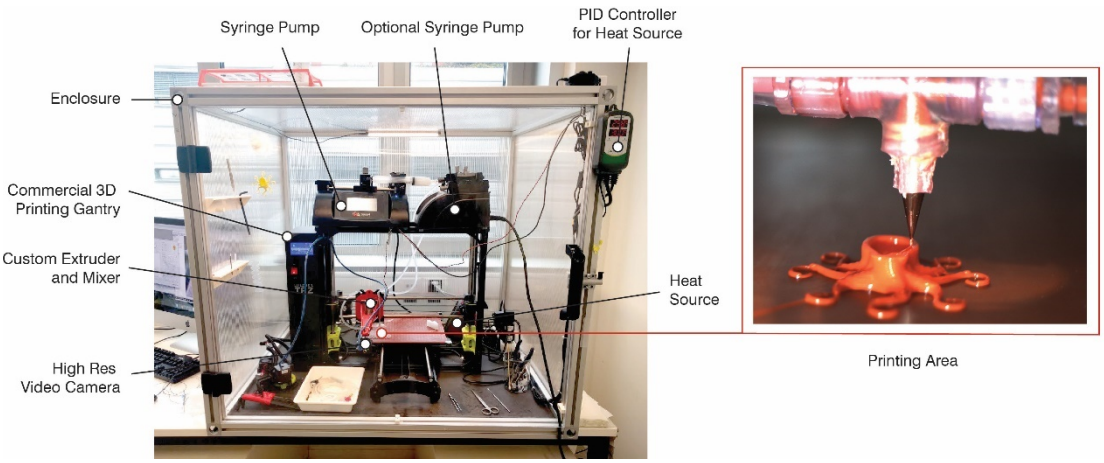


(b)

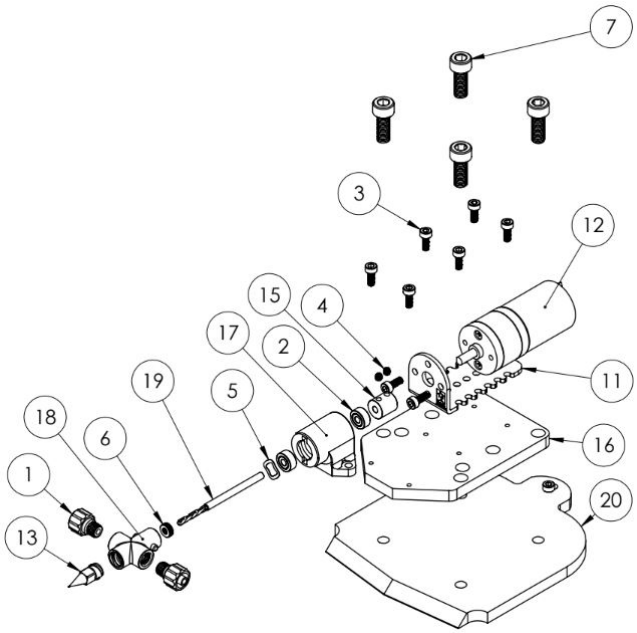


**Figure S8.** General printer appearance (a) and custom extruder design (b). More information, including how to build the entire system, can be found at mlabrobotics.com.

# 4

# 3D Printed Motor-Sensory Module for Facial Rehabilitation

**Notes on Chapter 4**

This work outlines a novel 3D printed multi-component wearable system created for facial rehabilitation, and how that wearable requires custom development of actuator testing methods in order to be applicable on a complex surface (the face). Using our custom silicone 3D printer and improving our understanding of extruded filament possibilities, we are able to print a fully functioning facial sensor-actuator wearable within four hours with minimal post processing. The main focus of this work was to show that a direct extrusion system can be integrated with both discrete parts (such as fabric) as well as other materials (like fluid conductors) to create a fully soft working device. The secondary focus is the required development of a custom actuator testing surface in order to mimic the highly complex motion and material behavior of the face. In this case, facial rehabilitation was chosen as the application because these devices will need a high degree of customization for force, contraction, and geometry behavior due to the high degree of uniqueness between human facial structure and rehabilitation needs. 3D printing allows for relatively fast iteration, starting with a base actuator and sensor model to achieve a custom fit per patient need. The on-body

system also requires no special rooms or visual equipment to perform therapy exercises.

The actuator went through several iterations that relied on numerous trials of differently shaped vacuum chambers. Ultimately, a rectangular shape was chosen due to the ease of printing silicone into thin vertical walls versus walls with overhangs. Incorporation of the fabric was also required in order to get the force application of the actuator to be high enough for facial force requirements (1-7 N). The rectangular shape made this fabric incorporation process easier. In the future, materials with a higher tensile modulus and/or an incorporation of reinforcing fibers into the silicone printing system will also improve the results. The custom designed skin and bone modular testing surface (SB-MTS) can also be used for other complex skin/bone morphologies. More complex behavior can also be added to the surface membrane, like looseness or tightness of the skin depending on location.

Authors:

Stephanie Walker[1,2], Amir Firouzeh[3], Matthew Robertson[3], Yiğit Mengüç[2,4], and Jamie Paik[3]

1. Materials Science, Oregon State University, Corvallis, OR 97331 USA
2. Collaborative Robotics and Intelligent Systems (CoRIS) Institute, Oregon State University, Corvallis, OR, USA
3. Reconfigurable Robotics Lab, École Polytechnique Fédérale de Lausanne, Switzerland

4. Currently at Facebook Reality Labs, Redmond, WA, USA

*Planned submission to the journal Soft Robotics*

Abstract

This work demonstrates the first 3D printed wearable motor-sensory module for facial rehabilitation, focusing on facial paralysis. The novelty of the work lies in the creation of a complete system, consisting of a connected actuator and sensor with a control system to translate signals from smiling on the healthy of the face to actuation on the paralyzed side of the face for augmented physiotherapy. Fabric and a sensor fluid are integrated during the silicone printing process to create a multicomponent wearable ready to use with minimal post-processing. The actuators' force and vertical contraction results under a 0.98 N and 1.96 N load are able to meet the 1-7 N requirements needed for smiling. A novel modular surface is designed to simulate the interaction of skin and bone using 3D printed hard plastic (bone) and a silicone sheet (skin). The actuator is tested on top of four different repeatable and standardized surface morphologies and results reveal that the actuator force application will vary based on topography and hardness of the facial surface. Demonstration of the complete system on the face while collecting sensor and pressure data serves as a proof-of-principle, and motivates potential applications in rapid customization of highly specialized soft wearable orthotics, prosthetics, and rehabilitation devices.

## Soft Wearables for Facial Rehabilitation

Wearable robotics and the rapid manufacturing methods that create them are two frontiers for technology development (*19*). Rehabilitative technologies in particular hold immense potential for human augmentation and increased quality of life. Research into exosuits [2,3], gloves (*219–222*), and joint rehabilitation technologies (*222–227*) is reflective of a desire to keep the human body functioning for as long as possible, while reducing mental and physical pain in the process. For soft wearables specifically, improved manufacturing methods are being explored to make the production less expensive and more customizable for individual patients and their medical conditions. Multi-component and multi-material 3D printing are particularly well-suited manufacturing methods for these wearables because of the possibility to integrate diverse and multiple soft elastomers and conductors for actuation and sensing in the same device.

One in 60 people will be affected by Bell's Palsy (producing facial paralysis) in their lifetime according to a study based on the population in the United Kingdom (*228*). More solutions are needed to ease their suffering when possible. While there is much research into rehabilitative wearables for exosuits and joints, there is a gap in the understanding of how soft devices can support facial movement. This gap is likely due to the complex nature of facial movement and the size limitations of current actuator solutions. There is a high degree of variability between human faces (*229*) which makes use of a generic size difficult. The few recent facial actuator solutions currently focus on restoring motor function of the face when one side has been

paralyzed (*230–234*). Rehabilitative facial devices have previously been created with cable-driven/shape memory alloy hard helmet systems (*230*), and shape memory alloy helices with discussion on optimal placement of soft actuators on the face (*231, 232*). They have also been created as training systems for rehabilitation (*233, 234*). However, some previous works rely on the pulling of wires from a single source moving across the face (*230–232*). These devices are not modular enough to enable complex force application in areas of the face like the corner of the eye or from the chin to lower cheek. The other previous works rely on a hard origami fingers requiring complex manufacturing, preventing easy customization (*233, 234*).

Facial paralysis introduces asymmetric expressions that can be embarrassing and physically restricting for the patient. Reasons for facial paralysis can stem from Bell's Palsy (*228*), stroke, tumors, or other neurological conditions (*235*). Some results of this paralysis are the drooping of the eyebrow and the corner of the mouth as well as difficulty closing the eye and the mouth (*228*). Restoring facial movement is key for ensuring that those with the condition do not suffer embarrassment due to their asymmetrical expression and are able to eat, drink, and speak normally (*236*). Along with prescribed medicines, facial exercises have shown promise for improving the condition in some cases (*228, 237*), including cases where patients need further rehabilitation after not fully recovering from Bell's Palsy (*238*). Facial movement rehabilitation practice can consist of enhancing desired facial muscle movements or reducing unwanted facial muscle movements (*239*). Physiotherapy for this condition involves exercises performed using the palsied side of the face, such as smiling, which mimic the healthy side to achieve symmetry (*236, 240*).

Achieving symmetry for patients with facial paralysis is critical to reducing their pain and stress levels, but it is difficult to achieve in patient healing. The ability to sense the motion of the healthy side of the face and translate that to identical movement in the paralyzed side of the face would augment and potentially increase the effectiveness of facial physiotherapy. Having the wearable give informational feedback to the user can be a valuable tool for sustaining motivation (*241*). Additionally, if the wearable has the capability to connect with game-based rehabilitation exercises, the potential for patient adherence to the rehabilitative protocol is increased (*242*).

A wearable device designed to encourage symmetry via existing healthy facial movements can help improve patient outcomes. For this type of device, several tasks need to be achieved: (1) facial movement needs to be measured and quantified, (2) the device needs to actuate, (3) the device needs to be placed in alignment with muscles for optimal actuation in the correct direction, and (4) manufacturing needs to be able to create a customizable and cohesive system. Preferably, this wearable needs to have dimensions based on individual feature sizes as well as customizable actuation behavior based on the severity of the patient's condition. No diagnostics currently have these qualities, as current physiotherapy relies on coarse and subjective methods. Actuators and sensors currently exist that could fulfill these needs, but no comprehensive solution exists.

In this work, a soft facial wearable motor-sensory module containing a paired vacuum actuator and embedded strain sensor is created via multicomponent 3D printing with silicone (Figure 1). The novelty in this work lies in the system-level device creation. The actuator is characterized for force and deformation under vacuum, and force behavior over 4 irregular curvatures covered in a skin-like membrane. The sensor is characterized for resistance under strain. As a paired system, the sensor can read strain from the healthy side of the face and the circuit can translate that strain into contraction force from the actuator. As an assistive device, the actuator is capable of contracting with 1-2 N of force (in the range of facial muscle). A demonstration on a healthy subject's face shows the ability of the module to perform a matching smiling motion when a smile on the opposite side of the face is sensed. Lastly, several actuator examples are created as a demonstration of customizability of the module via 3D printing.

The contributions of novelty in this work are:

1. The creation of a complete soft system for wearable actuation and sensing on the face
2. Addressing the need to measure and quantify patient progress in facial physiotherapy
3. The need to actuate on the face to augment physiotherapy exercises
4. The ability to position actuators over distinct muscle groups for specific rehabilitation
5. Addressing the manufacturing challenges for wearable robotics

This work is also transferrable to existing literature and platforms, such as adding sensors to existing actuator designs via 3D printing.

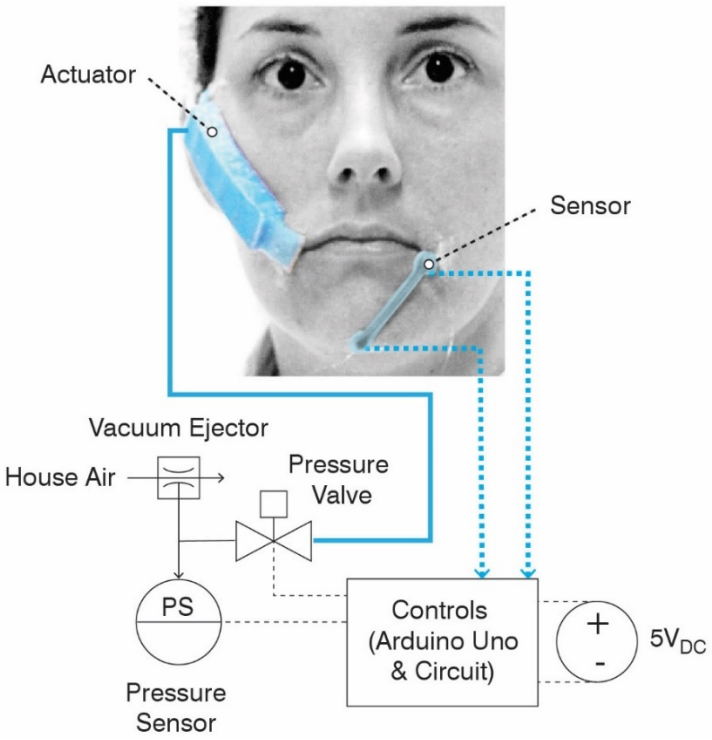


**Figure 1.** This novel comprehensive system can help augment physiotherapy via direct placement over specific facial muscles. This wearable can also help quantify patient progress in physiotherapy by tracking required pressure needed to actuate a paralyzed area of the face to match the healthy side. The vacuum actuator is designed with fabric inclusion to increase force output while still being comfortable on the face. The sensor/actuator pair communicate through a control board to translate sensor tensile strain on the healthy side of the face to vacuum actuator contraction on the side of the face with paralysis.

## Methods

The design and fabrication of this work stem from the need to create a wearable as a complete system. Because of the high level of variability in human faces, it is important that the system be quickly updatable based on improved design iterations. While the manufacturing method for this system is currently based in 3D printing, which allows for customization and iteration for anyone having this printer, other rapid manufacturing methods can potentially be used. Because the novelty of this work lies in the creation of the system itself, the exact actuator and sensor solutions are arbitrary, and the choice of other actuator and sensor solutions can be left to the person fabricating the system.

### Design for Biomechanics

Despite the potential benefits of wearable devices for facial rehabilitation, current availability to patients is limited and can lead to discomfort (from physical to psychological) while waiting for recovery (*239*). Giving the patient a wearable device that they can use at home (*243*) that is inexpensive, easy to use, and productive in alleviating their symptoms has the potential to reduce this discomfort and provide the patient with an active way to manage their healing. The possible reason for such lack of research into wearable rehabilitation for the face may stem from the complexity of both its active and passive motion. The high variability in topography and skin material properties and texture from person to person make the idea of designing an actuator system for the face quite daunting. For example, previous work in actuator

design for the face has used the ear as a stationary attachment point with the other side of the actuator attached to the cheek area (*230–232*), most likely to reduce the amount of undesired motion in the actuator, because almost all areas of skin will move when pulled. Directly mounting a soft wearable onto the face, while providing an increase in comfort due to compliance, brings up additional issues such as a moving mounting surface with graded mechanical properties (the skin). However, 3D printing provides an advantage for this use case as a manufacturing method. Customizing the actuator in morphology and mechanical behavior makes the overall production process low cost and fast on an as-needed basis. This allows for multiple iterations to be made to get the perfect fit for the patient, even with highly variable properties from person to person.

One of the most impactful facial movements is the smile, and so loss of the smile causes distress amongst facial palsy patients. Not only because those are some of the muscles used in eating and drinking, but also maintaining a “normal” facial appearance. To design an actuator that mimics facial movement, it is useful to look at the face’s muscular structure. The muscles that move during smiling are mostly the zygomaticus and the orbicularis oculi (*244*), but focusing on the zygomaticus contraction fits the movement of the corner of the mouth towards the cheekbone during smiling. Because this is arguably the most obvious motion one notices from a smiling person (as opposed to a squinting eye from orbicularis oculi contraction), designing an actuator for smile rehabilitation can start with the zygomaticus area. When designing actuators for the movement of the mouth during smiling, it is also possible to simplify the motion profile to a single linear direction (*245*). There is also

existing data which give the range of forces required to smile which further help bound how to design a wearable actuator (*245*).

Valuable benefits come from using this 3D printing silicone method for wearables. These benefits are directly in sync with The Wearables for Good Challenge produced by UNICEF and include: cost effectiveness, rugged and durable performance, and scalable implementation (various communities and environments) (*246*, *247*). Silicone materials have a variety of material properties (*111*) such as a high elongation, a relatively low elastic modulus, insulative behavior, and 3D printability. Numerous works have used silicone as an embedding matrix, either as a structural support during 3D printing to hold deformable and functional liquids (*15*, *51*, *52*, *248*) or as an encapsulating layer for deformable devices produced via molding or photolithography (*218*, *249–251*).

Because the face has delicate features such as the eyes and mouth that can be easily damaged, vacuum actuation is an appropriate solution because of the higher safety factor than positive pressure actuation. With vacuum actuation, the force is limited to the pressure that can be evacuated from the actuator, vacuum actuators fail in a neutral position. When a positive pressure actuator fails due to overpressure, parts of the actuator have the potential to hit those delicate areas. Vacuum actuation presents a viable option for facial robotics because the actuators can also be soft, lightweight and powerful (*122*, *252–254*). The patterning of buckling geometry has previously enabled muscle-like contraction with high forces (*122*, *252*) and motion control (*255–*

*257*). This safety factor is also needed when designing strain sensors for the face. The enclosed resistive element either needs to be a low-hazard resistive fluid or a solid elastomer to prevent injury from leakage of fluids onto the skin. Low hazard fluids such as glycerol are well-suited to this purpose, with conductive yet low hazard particle additives (*63*, *258*) for resistance measurements.

Evaluating a facial wearable module is also challenging due to the variability in facial features and skin behavior, so development of a unique test setup is needed. The face in particular has many different material properties (*259*, *260*) and designing a testing rig to approximate these properties, as well as the inherently uneven facial surface, is needed to give a more accurate representation of the performance of the wearable.

## Design and Fabrication

The advantage of using 3D printing to create wearables is the high level of customizability possible for both soft and hard components. In this work, one example is shown to illustrate the functionality available for smiling physiotherapy, though many other examples are possible. This process will also eventually be fully automated, requiring no manual assembly. In order to demonstrate the potential result of automation without needing to augment the current 3D printer system, fabric and hard components are placed by hand. The conductive fluid is also extruded by hand into the sensor reservoir.

3D printed actuators were designed to be fully compliant when adhered to the face. These were made out of silicone (Dragon Skin 10 Very Fast (Smooth-On) with Thi-Vex and Silicone Thinner additives) and polyester mesh fabric on a custom-built 3D printer. The silicone formulation and silicone printing method is detailed in previous work (*111*). The actuator designs (Figure 2a, 2b) were based on previous successful vacuum soft pneumatic actuators (SPAs) using rectangular geometry(*252*) to achieve force around 1-2 N needed for facial movement (*245*). Because the printing method relies on continuous extrusion of silicone, thin single-line paths of the 2D actuator shape are drawn in Illustrator, extruded into a 3D model in SolidWorks, and then sliced in Simplify3D to force the G-code to follow the specific path and to ensure that no pathways overlapped. More complex pathways can be developed with custom algorithms (*126*). The tabs were designed using extruded rectangles in SolidWorks. The length of the actuator (80 mm including tabs) was based on the length from the corner of the mouth to the cheekbone area of the author. This length is meant to cover the zygomatic muscle group, the principle muscle group responsible for the movement of the corner of the mouth. The height was kept at 12 mm to keep a low profile. One millimeter thick and 17 mm long silicone tabs were added to both ends of the for testing and for adhesion to the face, with the tabs centered at both ends to reduce anisotropic contraction.

Fabrication decisions for the actuator and sensor were made based on the need to adhere to a movable soft surface and retain enough strength for repeated use. As shown in Figure 2a and 2b, three areas of the actuator are reinforced with polyester

mesh fabric. To embed the fabric into the actuator, the first layer of the model is printed and the extruder tip is moved away. Then a piece of polyester mesh is rolled into the uncured layer, creating a composite, and the print is resumed until the layer just before the tabs is reached. After that section of the print is complete, a second 10 mm wide strip of polyester mesh is lightly pressed into the top of the print to adhere to the two ends and the middle chamber areas. Two hard plastic rectangles are also put next to the ends of the actuator to serve as support for the tabs, and then the print is resumed. The next section prints all the way up until just before the top encapsulating layers, and then the extruder moves away and a third piece of polyester mesh is pressed lightly into the top of the just printed section, making sure not to have the fabric extend over the print boundary; extending the fabric over the print boundary creates avenues for air to leak out. After the third piece of fabric is placed, the top encapsulating layers of the model are printed. About 10 minutes after the print is finished, the print is fully cured and can be removed from the build plate. To reinforce the tab areas, polyester mesh pieces are cut to match the size of the tabs and the end surfaces, leaving about a 10 mm strip empty on the lower side of each tab for adhesion to the face. The polyester mesh pieces are then glued to the tabs with Sil-Poxy. The air inlet tube is added by cutting a small slit in one side of the actuator and pressing the silicone tubing in, then gluing it in place with Sil-Poxy. Photos of this process are available in the Supporting Materials.

This sensor type was chosen to display the capability of the 3D printing system to enclose both fluids and hard components. The difficulty when creating soft sensors is

the incorporation of fluid components as resistive elements. The ideal sensor would not drift and should have repeatable resistance data versus deformation. However, fabricating custom sensors moves the result away from this ideal, especially when fabricating the sensor via a mixture of 3D printing and manual construction. The manual syringing of fluid into the silicone reservoir was not controlled for volume because of the difficulty of overcoming the surface interactions between the carbon/glycerol fluid and the silicone when filling the reservoir, as well as the small size of the fluid reservoir. Sensors in general are difficult to create, and there are enough difficulties in sensor production to fill a full time research schedule. So, the solution presented here is meant as an example and should not be considered as an exclusive option. The novelty in the sensor is based on the requirements of the wearable system and not necessarily the exact component. The sensor models are a hollow dumbbell shape with a cavity for conductive fluid and two electrodes on each end for 4-point resistance measurement (Figure 2c, 2d). The electrodes were fabricated by rolling the end of each wire into a small spiral (2 turns) and then melting solder onto the spiral, forming a small ball. Two electrodes were melted into an oval-shaped thermoplastic anchor to help them stay in place after encapsulation. Sensor reservoirs were fabricated by printing most of the dumbbell (all except the top encapsulating layer) in silicone and then moving away the extruder. After the silicone reservoirs were printed, the anchors were pressed lightly onto the silicone on each end of the sensor. The wires were then pressed lightly through the still-wet silicone ends until about halfway down the model. After about 5 minutes, the conductive carbon solution was pipetted into the reservoir until the liquid level reached the top of the

reservoir (solution composition by weight: 14.3% Carbon Powder (99%, ABCR.de), 85.7% Glycerol (99%, Sigma Aldrich)). Then the top cap of the sensor was printed to encapsulate the electrodes and the solution.

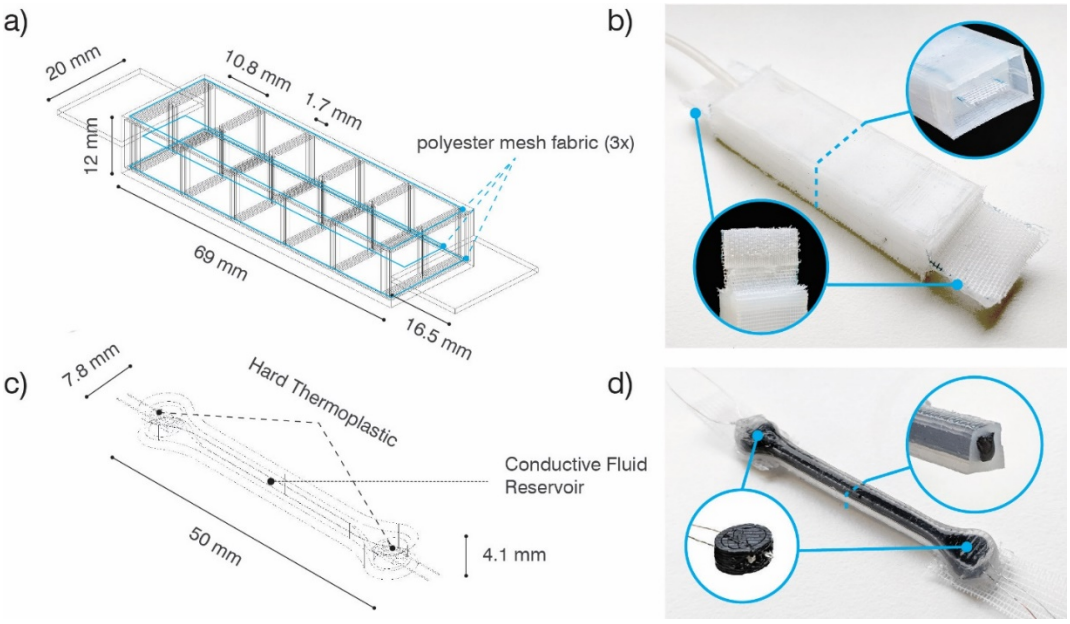


**Figure 2.** (a) Wire frame of actuator model and (b) resulting printed actuator after adhesion of reinforcing polyester mesh and Velcro in the tab areas. Velcro is only attached to the tab areas for characterization, not for attachment to the face. (c) Wire frame of sensor model and (d) resulting printed sensor after attachment of polyester mesh tabs for characterization.

## Module Prototype Characterization

The following tests were performed to simulate and characterize the performance of the integrated system on the face. The soft movable membrane attached over a hard

bone-like surface enabled characterization in more realistic use conditions than blocked force or contraction alone.

Actuator contraction was tested at facial forces in the range of 1-2 N and a slow frequency (6 cycles/min) to mimic the time periods possible during physiotherapy sessions. Actuator contraction was determined via application of a cyclic vacuum pressure while one end of the vacuum actuator was fixed and the other was connected to either a load of 0.98 N or 1.96 N for 10 cycles. The vacuum pressure was applied in 5 second on / 5 second off intervals to operate within a time range reasonable for physiotherapy and complete repressurization of the actuator. Actuator contraction data (lift distance versus time) was recorded via video and processed with Tracker software (Tracker specifications are available in Supporting Materials).

Sensor extension was tested based on approximate facial deformation conditions. Sensor signal response was determined using a custom DAQ connected to LabView 2016 software in a 4-point resistance measurement. The sensor extension, 17 mm, was estimated as the distance difference between the corner of the author's mouth at rest versus the corner of the author's mouth during a smile (more information in Supporting Materials). The sensor was tested for 100 cycles with the following protocol for each cycle: extend to 17 mm at 1000 mm/min, hold for 5 s, release at 1000 mm/min to 0 mm, hold for 5 s.

To simulate the behavior of the actuator on the face, a custom skin and bone modular testing surface (SB-MTS) was created out of hard thermoplastic (representing bone) and a silicone membrane (skin) (Figure 3). The custom curvature peg board was 3D printed with hard thermoplastic using a Stratasys uPrint SE Plus. The base was designed with a 9 x 9 grid of depressions to hold a set of modular pegs with 12.7 mm diameter spheres on top. The sides of the base were also printed with holes for heat set threaded brass inserts. The heat set inserts were sunk into the holes using a soldering iron. The maximum difference in peg sizes (12.7 mm) was chosen based on measurement of the approximate difference in the authors sunken cheek area and cheekbone. The peg heights above the base are 5.8 mm, 12.2 mm, and 18.5 mm.

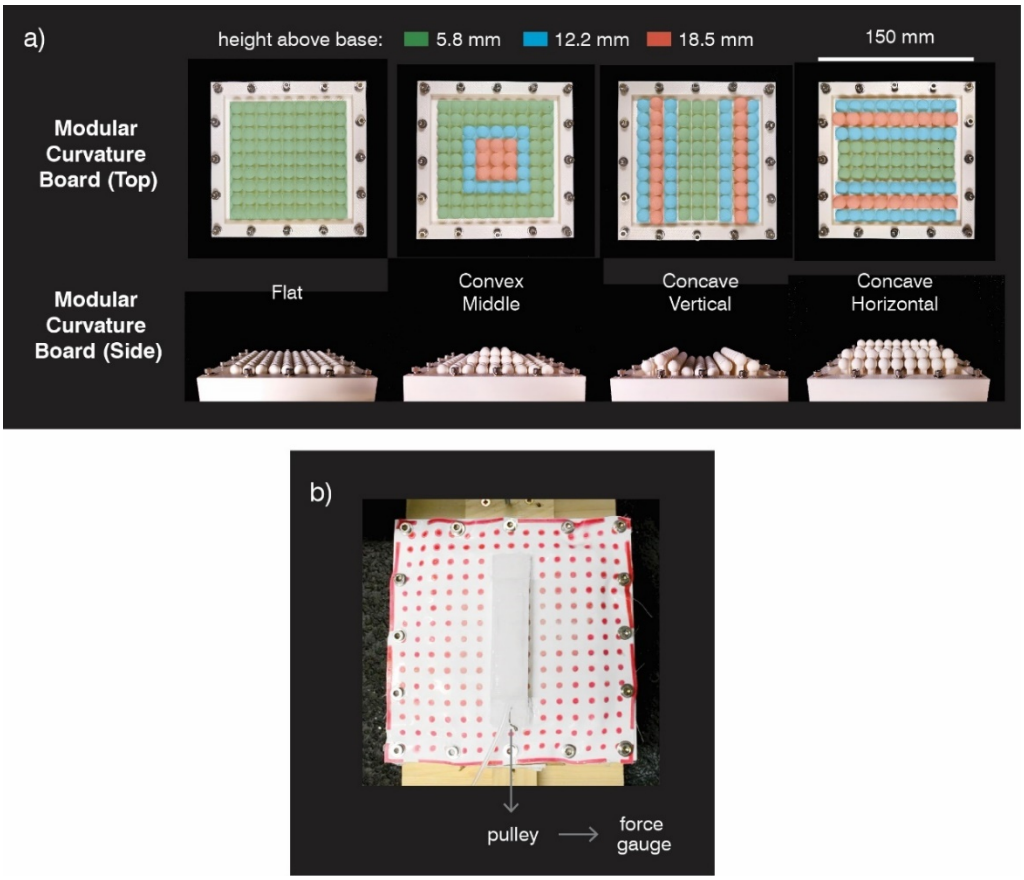


**Figure 3.** (a) The tested structures of the SB-MTS are flat, convex middle, concave vertical, and concave horizontal. The pegs are 5.8 mm, 12.2 mm, and 18.5 mm above the base, making the max difference in height 12.7 mm. Four surface curvatures are created using these pegs: (1) flat (all 5.8 mm pegs), (2) convex middle (center of nine 18.5 mm pegs surrounded by a square of 12.2 mm pegs with the rest as 5.8 mm pegs), (3) concave vertical (column height from left to right as 12.2, 18.5, 12.2, 5.8, 5.8, 5.8, 12.2, 18.5, 12.2 mm), and (4) concave horizontal (same configuration as the concave vertical rotated 90 degrees). (b) The membrane was attached to the surface with machine screws and washers. The actuator was attached at Velcro points on the membrane and hooked up to a pulley leading to a force gauge.

The membrane base was created with a film spreader and consists of a 1 mm thick Dragon Skin 30 membrane (0.8 wt% Silc Pig White dye, 10 wt% Silicone Thinner, balance Dragon Skin 30 Part A and B in equal amounts) airbrush-painted with a thin layer of Psycho Paint (Smooth-On) (2.8% Silc Pig White dye, 69.4% NOVOCS Matte solvent, balance Psycho Paint Part A and B in equal amounts) through a laser cut stencil, forming a dot pattern that stretches with the membrane. The outer edges of the membrane are glued with Sil-Poxy to an approximately 12 mm wide polyester mesh fabric strip to reinforce the membrane. Then holes are cut through the silicone and fabric to attach the membrane to the peg board with machine screws and washers. The silicone membranes were made to approximate the deformation of facial skin with a tensile modulus that falls within skin's Young's moduli range. Young's moduli of human skin range from 0.05 to 20 MPa depending on test method (*260*). There are existing tutorials for creating suture practice skins which mimic skin with multiple layers (*261*), but because human skin mechanical performance changes due to age and hydration (*260*), and its overall behavior is complex (anisotropic, nonlinear, and viscoelastic (*262*)) a simplified single-layer membrane solution was chosen to not overly complicate the experimental setup with unknown correlations. In biomechanical tests, skin also shows homogeneous behavior (*260*).

The SB-MTS board is placed into a pulley rig and bolted to the bottom of an Instron. One side of the actuator is hooked to the force gauge through the pulley using a Trilene 100% fluorocarbon fishing line and a small metal hook. To try and decouple

the force values from the role of any adhesive attaching the tabs to the membrane, one part of a two-part Velcro is glued with epoxy to the membrane and the other side of the Velcro is glued with Sil-Poxy to the actuator tabs. Both tabs are then attached to the membrane in line with the pulley. After the actuator was attached, the pulley line was pre-loaded with 0.5 N of force to hold it taut and vacuum was then applied to the actuator from -86 kPa ( for 5 s) to atmospheric pressure ( for 5 s) for a few cycles. Video was taken of the actuator next to a ruler and the amount of extension in the membrane for each of the four surfaces was determined. The extension of the membrane during full actuation on the flat surface was approximately 3 mm in 1 s. The concave vertical, concave horizontal, and convex middle extension values measured using the same method were 4 mm, 1 mm, and 1 mm respectively. The speed of extension on the first sheet (180 mm/min) was used to input into the cyclic membrane calibration tests described below using the separately determined membrane extension distances. To separate the force results of the actuator from those of the sheet, calibration was performed before each actuator surface curvature test with the fishing line threaded through two hard plastic tabs with holes, with one tab allowing sliding motion of the line. The tabs were pulled to the extension distances experienced by each membrane surface (determined earlier) and then released for 10 cycles. Each force difference data set per sheet was averaged to determine one average force difference per surface type. This force difference was added to the actuator data to isolate the force behavior to each actuator alone. The resulting force for each actuator/silicone sheet pair is recorded versus time in coordination with the opening and closing of the vacuum valve.

The demonstration of the wearable motor-sensory module was performed on a healthy subject (the author) to mimic the expected behavior of a patient. The actuator was adhered to the skin near the corner of the mouth and the area just above the cheekbone. The sensor was adhered to the center of the lower chin and the corner of the mouth on the other side of the face. The adhesive (Kryolan Silicone Adhesive Regular Bond) was first applied to the areas of the face where the sensor and actuator were going to be adhered. The adhesive was then applied to the specified areas on the actuator and sensor. Then the adhesive was left to dry for 5 minutes. Once dried, the parts of the wearable covered in adhesive were pressed onto the areas of the skin to set the bond. The actuator was then hooked up to the vacuum circuit and the sensor as hooked up to the bread board circuit. The sensor value when the subject was smiling was quickly determined using the analog signal serial readout and that value was uploaded with the control code to the Arduino as a threshold value for actuation initiation. Video was recorded of the smiling motion of the “healthy” side translating to the contraction of the actuator/smiling mimic on the “paralyzed” side.

## Results

### Actuator and Sensor Characterization

Performance of the actuator under a blocked force and free extension condition is outlined in Figure S2. Blocked force data for three actuators over 100 cycles show a range of about 5 to 6 N of blocked force assuming no elongation (Figure S2a).

Average contraction with a load was about 10 mm for 0.98 N and 8 mm for 1.96 N (Figure S2b). These results are a good start to show that with a 1-2 N load the actuator can pull the corner of the mouth about 10 mm. Sensor data show drift in the initial data but reach equilibrium after a few minutes of use (Figure S2c). The results show that the actuator can successfully operate in the force ranges required for facial smiling movement, and that the sensor gives a clear enough signal to differentiate a strained versus unstrained state.

SB-MTS Curvature Characterization

SB-MTS curvature characterization showed that different underlying hard structures will cause the actuator to apply different force values (Figure 4). The flat and concave vertical surfaces allowed the actuator to provide more force because of a lack of obstructing geometry pressing into the actuator when compared to the other surfaces. The concave horizontal and the convex middle both have geometries that press more into the actuator and so obstruct the actuator, even with a low-friction surface. This is useful because while the force values determined are adequate enough to move the mouth (1-2 N) if more force is desired, actuators may have to be designed to apply higher forces for different underlying surface features. Interesting behavior occurs when there is less of an obstructing hard surface underneath the actuator. The actuator in the concave vertical setup presses into the membrane because there is a gap between the membrane and the modular pins. Effectively, it sinks into the loose membrane areas. Overall, this result confirms the assumption that the actuator design needs to consider the topography of the face as well as the underlying hardness or

softness of the skin and bone composite surface. Harder surfaces and protruding features (such as the cheekbone) will need an actuator with higher force application than areas with softer surfaces (such as the hollow of the cheek).

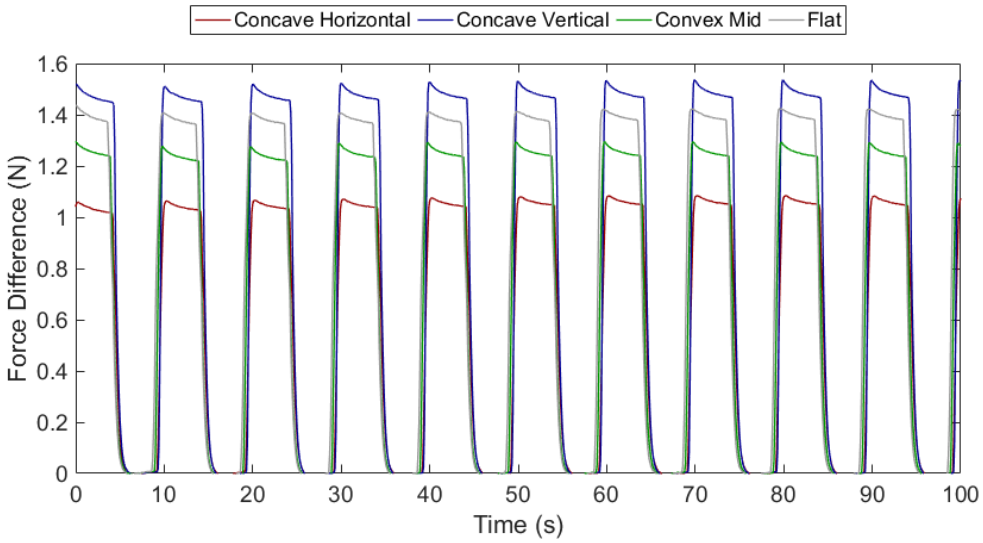


**Figure 4.** Actuator testing results on the SB-MTS (a) Four surfaces of different contours: flat, convex middle, concave vertical, and concave horizontal mimic the possible facial structures on which wearables will function. The force results of four actuators tested across the four different surfaces reveal that the force applied by the actuators does change based on surface topography. The flat and concave vertical results showed the most force application due to the lack of geometry pressing up into the actuator. The concave horizontal and convex middle both have geometrical features that press against the actuator which, even with a low friction surface restrict motion.

**Motor-Sensory Module Demonstration**

The demonstration of the wearable system is performed on a healthy subject. The overall placement, operation steps, and five cycles of sensing and actuation are shown in Figure 5. The video source of Figure 5 is shown in the Supporting Materials. Figure 5a shows the initial relaxed state, the half smile from the "healthy" side of the face, and the resulting contraction from the actuator. The sensor signal when smiling ranged from approximately 575 kΩ to 690 kΩ with a threshold value of 616 kΩ set for the beginning of actuation. The data for sensor resistance with strain (dark gray) and pressure (blue) versus time of test show an immediate actuation after the sensor reaches the threshold value. There is some signal interference in the circuit that causes the baseline of the sensor data to shift when the pressure valve signal is sent, but the sensor data is still clearly seen as a peak before each actuation cycle commences. To set up the wearable for use takes about 15 minutes, a reasonable time for physiotherapy. Overall, we successfully demoed the system to show its applicability for facial exercises. The recorded data are also reflective of a real patient's results.

To illustrate the potential of these methods to create more custom geometries, other actuators with varying force characteristics and geometries were printed. Starting with the basic actuator (Figure 6a), a graded force profile (Figure 6b), graded contraction profile (Figure 6c) or a smaller actuator (6d) can be created. 3D printing makes this possible, and provides options if different types of contraction are needed.

Eventually, 3D printing can produce full masks with multiple force profiles (Figure 6e). By introducing materials with a higher tensile modulus into this 3D printing system, smaller and stronger actuators can be created as well. The printed examples outline the larger scope of the module enabled by fast fabrication.

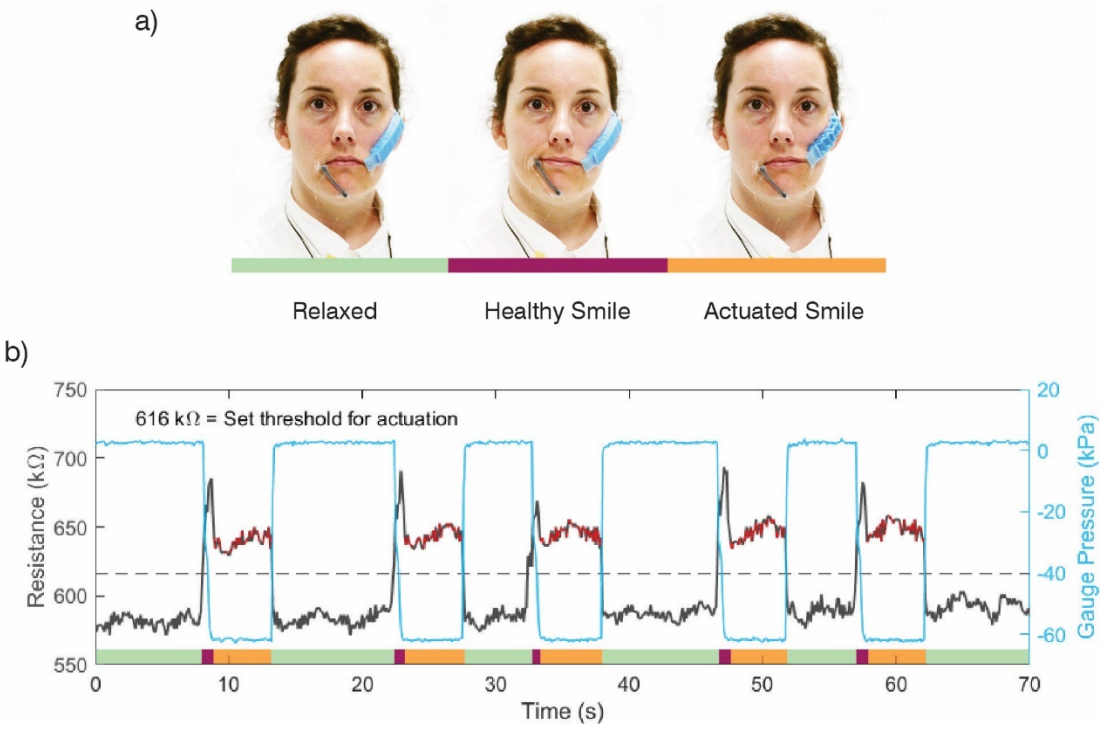


**Figure 5. (a)** The sensor is adhered to the center of the chin and the corner of the mouth. The actuator is adhered to the corner of the mouth and just above the cheekbone, laying in the direction of the zygomaticus muscle. The sequence of actions for the module are (1) relaxed face, (2) smile on the healthy side of the face, and (3) actuated smile from actuator contraction (achieving symmetry). Each action is color coded to correspond to the time period in the graph. **(b)** The sensor resistance ranged from approximately 575 kΩ to 690 kΩ during smiling. The interference in the

Arduino circuit increased the overall values of resistance when actuation signals were sent, but the peaks in the resistance data still represent the increasing strain in the sensor during smiling. The action sequences were performed at irregular intervals to ensure the actuator was not accidentally responding. These data are also more reflective of a real patient's results.

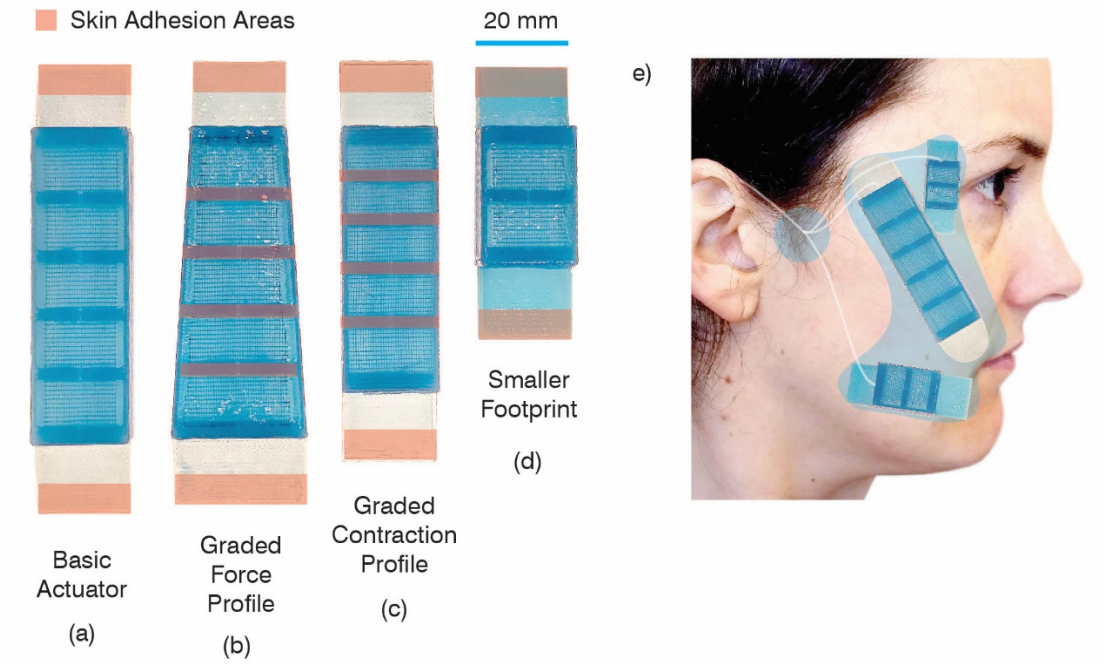


**Figure 6.** (a) The basic actuator design can be altered to have features customized to a patient's facial rehabilitation needs. A few simple examples presented here include (b) a graded force profile, (c) a graded contraction profile, and (d) a smaller footprint. The actuator can be adhered in different areas to provide different amounts of force or contraction if needed. Other options include a smaller overall actuator with the same number of chambers, and actuators printed with a tougher elastomer. (e) 3D printing also allows multiple actuators to be printed within the same mask structure if needed.

## Discussion and Future Work

A complete and cohesive system is crucial for augmenting physiotherapy exercises and tracking patient progress. Ideally this module could be a single printable file customized per patient, such as a mask with sensors embedded into the elastomer base. Since manufacturing in soft robotics is traditionally performed piecemeal with molding and lamination methods, cohesiveness in manufacturing is seldom discussed. 3D printing advances the production of these wearable robotics via precise control of geometry with possibilities for quick iteration and customization, as well as integration of multiple materials and components. Because this manufacturing method can be fully automated, more complex wearables can be printed with less manual intervention.

Facial wearables require a high degree of complexity and a larger range of material properties than current solutions provide. Manufacturing methods, especially 3D printing, are now becoming advanced enough to accommodate multiple materials and multiple components through embedding methods, as seen in this work. 3D printing allows for the creation of custom components that can be resized according to the wearer's body dimensions and also be manufactured relatively quickly. For example, the basis actuator in this work can be made into a working wearable in about 3 hours, including printing, insertion of fabric, insertion of tubing, and adding reinforcing layers. This time can be further reduced with improvements to this system, such as the automation of component placement with a pick and place machine, and also

mixing in of reinforcing fibers into the silicone while printing. In the context of physiotherapy, this means that the wearable can be created for the patient, tested, altered, and remade all within the same day. The use of an on-body actuator and sensor also eliminates the need for complex facial recognition software, equipment, and a specialized environment (*263–265*). This motor-sensory module can be taken home and used with minimal setup. The actuator and sensor solutions developed here are also only one option for those seeking to make a similar system, as the module concept can be applied to other types of actuators, sensors, and fast fabrication methods.

Vacuum actuation is a great solution for wearables, especially around sensitive areas like the eyes and mouth. Vacuum actuation has a higher safety factor than positive pressure actuators because vacuum actuators will fail in the neutral unactuated state as opposed to popping due to overpressure. This limits the force of the actuator surely, but due to the relatively low force requirements (~1-7 N for smiling, for example) this limitation can be lessened by improving the tensile strength of the material(s). To get higher forces, a material with a higher elastic modulus, such as Dragon Skin 30, as well as other formulations with fibers mixed into the silicone, can potentially be printed using this machine. The inherent softness of the silicone elastomer also makes the wearable more comfortable for the patient and more robust to potential damage than some wearables which rely on a mixture of cables and hard components. The open-ended nature of the direct extrusion of silicone allows this printing method to be augmented with both discrete component placement (such as

fabric pieces and hard sensors) as well as injected fluid/soft material deposition that forms to the shape of the silicone reservoir. In both cases, the silicone serves as an excellent encapsulating layer and protective element for delicate components.

Future work on this project revolves around the development of wearable solutions addressing other desired muscular motion of the face as well as studying actuator applications for reducing undesired muscle behavior. Further exploration will be performed on how to construct a more complex SB-MTS to represent generalized facial movement. Testing of the actuator on human faces will be a useful tool to analyze the behavior on patients of several ages and skin types. More analysis into the true deformation of human facial skin in relation to adhered facial appliances is needed. Incorporation of a second sensor into the actuator print is planned for coordination of direct strain readings with contraction on human skin. This module introduces a customizable, novel system that can be implemented to reduce physical and mental pain in those needing facial physiotherapy. The ability to potentially track patient progress is also a valuable tool for quantifying facial symmetry over time. With more development, the module can be implemented with minimal effort at home and in therapy offices.

# Supporting Materials

## Tracker Software Specifications

Displacement data was generated from video data using Tracker, a free video analysis and modeling tool. Red tape squares were attached to the lower region of the 100 g and 200 g weight sets, and served as reference regions for tracking during contraction. Tracking is accomplished by searching each video frame for a region that exactly or approximately matches a reference region specified in an initial key frame. Displacement is calculated between the centroids of the matched and reference regions. The key frame was chosen at a time when the actuator was at an unpressurized rest state and an elliptical reference area was specified in the key frame such that the square feature was inscribed in the boundary ellipse of the area. Key frame evolution rate in the software was set to 0% to require the software to use the same elliptical reference area throughout the analysis, and the visual recognition criteria was set to the default value of 4. Maximum deviation of the boundary ellipse of the matched region from the corners of the square target was visually found to be less than 4 pixels, which equated to approximately 0.25 mm.

## Materials Testing

Materials testing gives insight into the material-level behavior of the silicone and fabric components of the actuator and the sensor. Tensile and cyclic testing were each performed in triplicate on 3D printed silicone dumbbells (3 samples for tensile with silicone only, 3 for cyclic with silicone only, and 3 for tensile with a fabric/silicone

composite). The dumbbell shapes were based on ASTM D412 Die C dimensions. Actual printed dimensions varied slightly (the 2 mm high and 6 mm wide center gauge length turns into an approximately 1.8 mm high and 6.3 mm wide model due to deformation in the silicone). The mean values of three samples are plotted. Gray shading shows the standard deviation.

Average tensile strength at 100% strain of the silicone dumbbell samples in tensile testing was 72 kPa. The average modulus at 100% strain was 63 kPa, which is approximately a third of the 152 kPa 100% modulus reported for the pure Dragon Skin 10 Very Fast polymer. The elongation at break of the tested dumbbell samples was not found due to slippage of the samples out of the grips when the strain passed 1000% (Figure 3). Average tensile strength at 100% strain of the silicone and fabric composite was 216 kPa due to the breakage of the fabric before 100% strain. The maximum fabric strain was 39% and the maximum fabric stress before break was 1.33 MPa. The addition of the fabric to the actuator imparts the actuator with the ability to handle larger stresses, and because the fabric within the actuators is assumed not to be breaking during use, the reinforced actuator areas are not being strained larger than 39%.

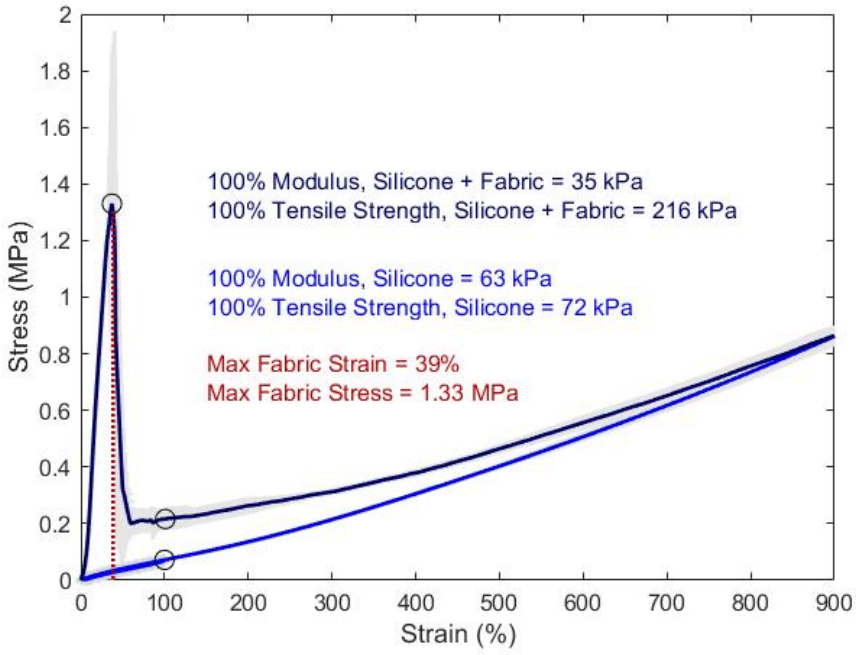


**Figure S1.** Tensile and cyclic testing for 3d printed dumbbells gave values for 100% modulus and tensile strength at 100% modulus. Silicone alone had a 63 kPa modulus and 72 kPa tensile stress, and the silicone/fabric composite had a 35 kPa modulus and 216 kPa tensile stress. The explanation of results for the fabric and silicone composite are complex due to the broken fabric potentially slipping inside of the silicone. The fabric broke inside the silicone at an average of 39% strain and at 1.33 MPa stress.

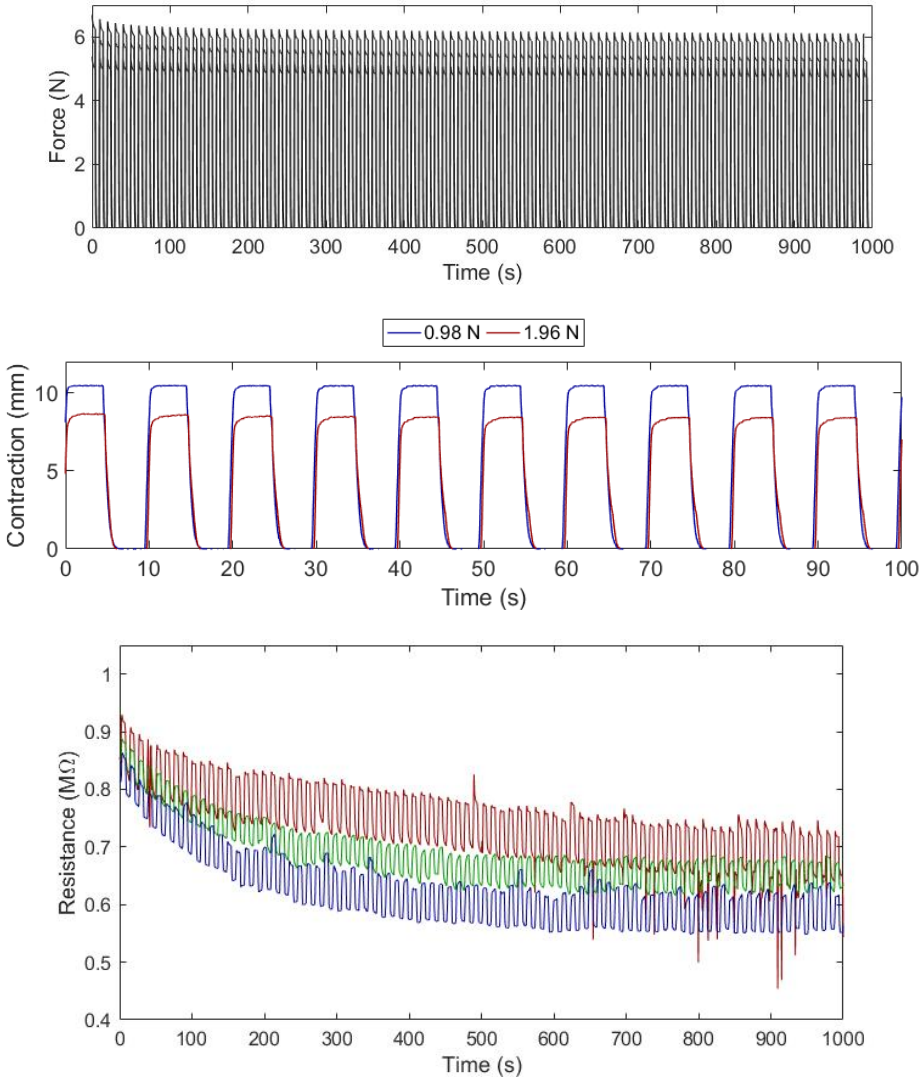


**Figure S2.** Actuator performance was measured both in (a) a fixed configuration where both tabs of the actuator were clamped in the Instron for 100 cycles, and (b) a free configuration where one side was clamped into the Instron and the other side lifted a 100 g and 200 g mass for 10 cycles (force values of 0.98 and 1.96 N). (c) Sensor testing shows an area of relatively constant signal is reached after a few minutes.

Printing Process

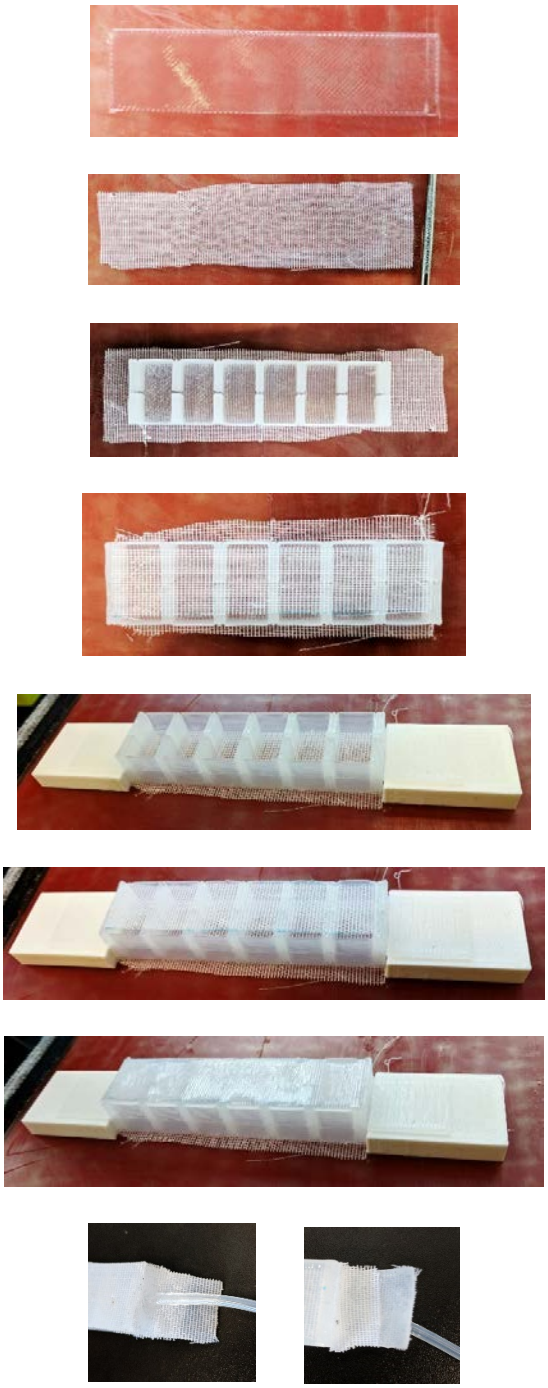

**Figure S3.** The printing process for the actuator is completed in several steps by starting and stopping the extruder and moving it away from the bed while placing pre-cut fabric in the appropriate shape. After the actuator is fully printed, reinforcing pieces of fabric are glued to the actuator tabs and a tube is glued into one side.

SB-MTS Board Design

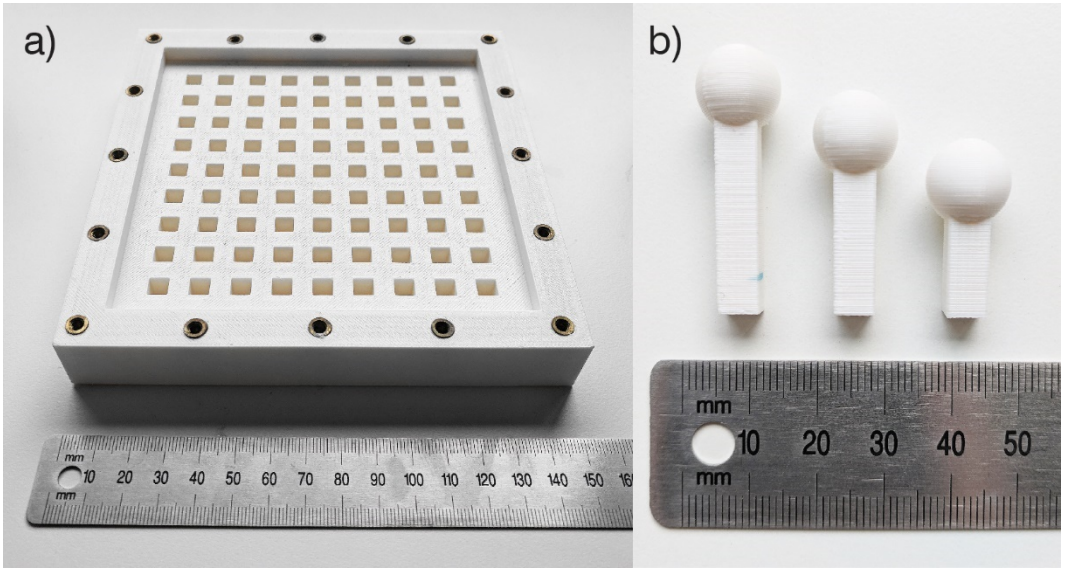


**Figure S4.** The SB-MTS was created so that many surfaces could be tested on the same rig. The heat sink threaded brass inserts are for M4 screws and washers which attach the silicone membrane to the rig.

SB-MTS Membrane Calibration

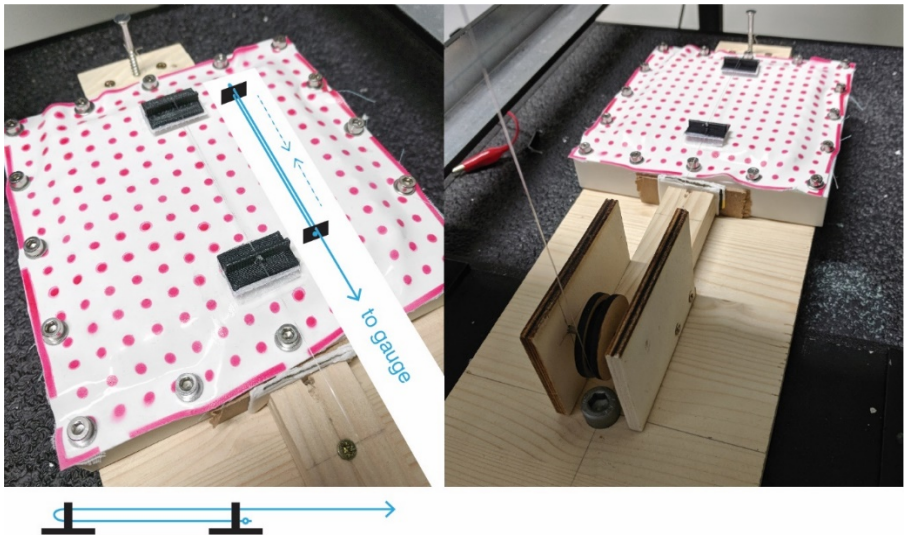


**Figure S5.** To reduce the effect of the forces from the membrane on the force reading of the actuator, the membranes were tested in cyclic contraction with distances and speed determined via actuator video.

Facial Strain Estimation

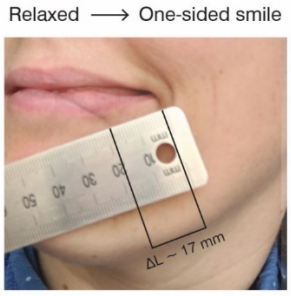


**Figure S6.** To estimate the amount of strain for the facial sensor, the difference between a relaxed corner of the mouth and the mouth in a half smile (of the author) was used. The distance between the corners of the mouth in the two overlaid photos gives an estimate, assuming that the other anchor point there the sensor is adhered (center of the lower chin) is not moving too much.

Circuit Fabrication for Actuator Testing and Sensor-Actuator Demo

To connect the sensor reading to the actuator contraction, the sensor was hooked up in parallel with a 1 MΩ resistor, and the signal was read by an Arduino Uno using the analog read function. The analog sensor signal correlated to the subject smiling was translated into a digital write command to turn a LHDA0531215H Solenoid Valve (The Lee Company) on and off. The vacuum circuit was constructed from house air, a ZH10B vacuum ejector (SMC), a MPX5500DP pressure sensor (Freescale Semiconductor, Inc), a power supply set to 5 V, an Arduino Uno, and a breadboard circuit. The pressure valve was connected to the vacuum ejector and to house air, and vacuum pressure pulses from the valve were controlled via the Arduino directWrite command (high = full vacuum, low = no vacuum (atmospheric pressure)).

Circuit Interference Baseline

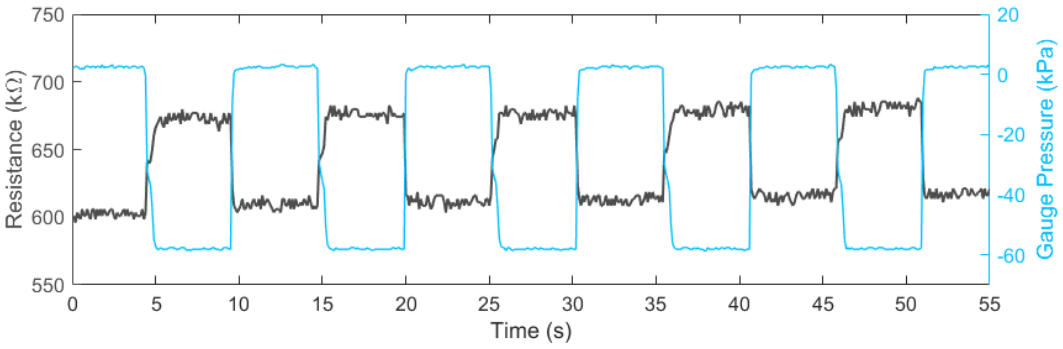


**Figure S7**. The sensor does experience some interference (a shift in the baseline of the sensor data signal) when the digital signal is sent to the pressure valve. This data is distinct from the sensor signal.

Actuator Form Exploration

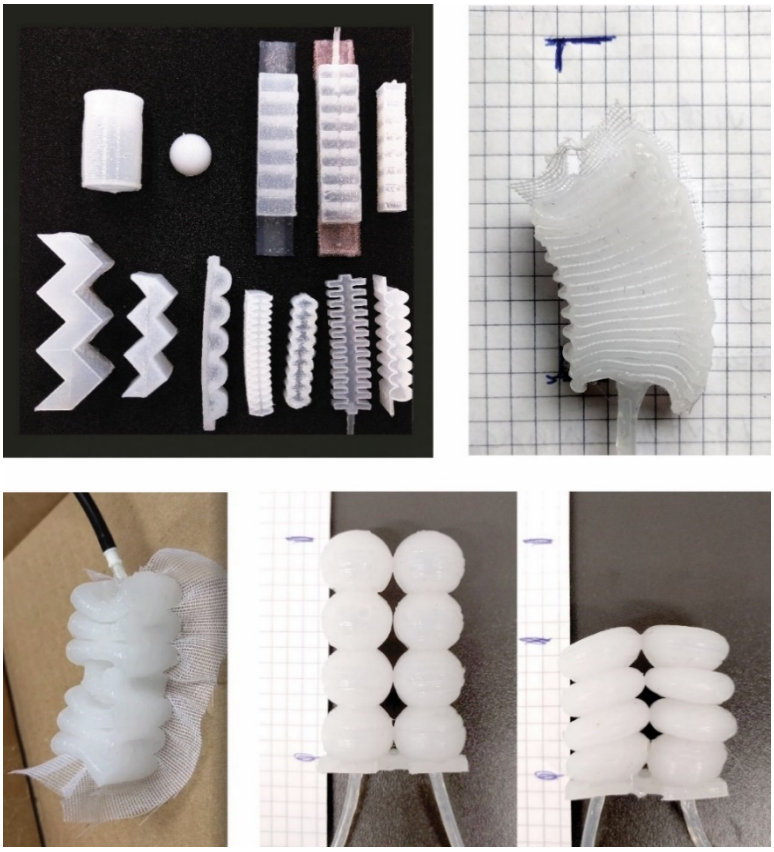

**Figure S8.** Several trials were performed on different actuator geometries to experiment with the geometrical limitations of the printer and to determine better strategies for this direct extrusion system. Ultimately a rectangular shape was chosen so that fabric could be incorporated more easily in order to strengthen the actuator.

# 5
# Conclusions

The goal of this thesis work was to use materials science integrated into soft robotics research to expand upon and introduce new ideas for additive manufacturing and fast fabrication for soft robotics. This was achieved via three main projects including the incorporation of multi-component 3D printing with both hard and fluid elements into a silicone additive manufacturing process, demonstrating the importance of rheology and curing kinetics by taking advantage of transient material properties in 3D printing, and creating new materials which allow the soft robot to be quickly made, as bio-sourced as possible, and safely degradable into the environment.

Chapter 2 introduces simplified polymer syntheses for two elastomers (one heat-cured and the other UV cured) created to make a biodegradable robot actuator. These works first outlined the development of an environmentally benign and degradable elastomer, and then added to the chemistry to allow for the polymer to potentially be used in a photopolymerization 3D printer. For uses of soft robots in military technology and environmental sensing, for example, a disappearing robot is needed either for stealth reasons or to reduce the amount of garbage the robot leaves behind after it “dies”. The point of producing the biodegradable elastomer was to show how soft roboticists, even without much chemistry experience, can customize their materials for a specific ultimate purpose instead of relying on off-the-shelf prepared chemicals which can ultimately limit their final robot possibilities. Having that same

elastomer be UV curable opens up opportunities for not just customization but additive manufacturing. There is currently very little research in soft robotics literature about developing custom materials for biodegradable soft robotics solutions. Developing materials syntheses for specific soft robot morphology and function brings a higher level of control to soft robot fabrication. Eventually, a synthesis procedure based on raw materials can be incorporated into the additive manufacturing process. This will bring a high level of control to the manufacturing process and will also require integration with materials science research.

Chapter 3 introduced how rheology and curing kinetics can be used in tandem to define printing time boundaries in a mixed silicone system. The most important part of the work was the idea that transient material properties (when properly characterized) can be used advantageously to improve 3D print quality. Materials characterization knowledge from rheology and curing kinetics in this case improves the print quality of a soft silicone fluid that would otherwise collapse as a 3D model when printed without support. Current research into silicone 3D printing using direct extrusion methods does not take advantage of the changing material properties during curing. Because the direct extrusion and mixing system does not require any curing conditions besides heat, it leaves open the possibility for other heat curing materials or rheological control additives to be integrated to make graded structures. With further development of the extruder path planning and flow control, this open-source system can be used in the study of several thermoset material systems for soft robot additive manufacturing.

Chapter 4 outlined how the combined use of a silicone 3D printer and placement of fabric and conductive fluid can facilitate the creation of a customizable rehabilitative facial device within a few hours. That work also reiterates a common theme - that the ability of 3D printing systems to quickly create personalized low cost devices anywhere there is a 3D printer. This is especially important in the facial rehabilitative and medical fields, due to the high variability in facial geometry and skin material properties in humans. A 3D printable and fully soft rehabilitative device for facial paralysis does not currently exist in literature. The device itself can also be used as a diagnostic tool during physiotherapy to monitor a patient's progress in rehabilitation exercises. The complexity of the 3D printed actuators can also be increased to include more muscle groups on the face and rehabilitate several areas of facial muscle at once. This work also emphasizes the need to develop custom testing systems for these new 3d printed soft robotics. A standardized skin and bone modular testing surface (SB-MTS) with skin and bone analogs was designed to better understand how the actuator would perform on facial surfaces without the need for a human test subject. This SB-MTS can also be integrated with electronics and motors in the future to automatically change shape for faster testing setup. The work also contributes to the soft robotics field by enhancing understanding of how multiple materials can be incorporated into one printing system assuming automation is possible in the future.

This thesis addresses one of the grand challenges of robotics today – how to create more materials available for soft robotics use, and how to use these materials for 3D printing and additive manufacturing systems (*19*). To do this, understanding of how

the materials can be synthesized, how they can be processed and integrated into additive manufacturing technologies, and how they should be analyzed for material and device performance is required knowledge. This work not only recognizes the available opportunities in additive manufacturing for soft robotics, but emphasizes the important existing materials knowledge required to make these manufacturing systems function optimally. The overall goal from this grand challenge soft robotics is to move away from one-off solutions and create soft robots on a larger scale. Creating robots on a larger scale means more predictable behavior and higher quality soft robotics. This requires in-depth understanding of ***how soft robots are made.***

## Contributions of this Work

*Using an Environmentally Benign and Degradable Elastomer in Soft Robotics*

- Focus on green chemistry in soft robotics elastomer development
- Bio-sourced and (bio)degradable chemicals and final product
- Focus on degradable and temporary robotics
- Development of simpler version of complex synthesis procedure (PGS)
- Biodegradable UV curing crosslinker and photoinitiator incorporation
- Increase of safety factor in photopolymer synthesis
- Laser etching of biodegradable elastomer to achieve specific geometries
- Fast fabrication of a custom elastomer

*Zero Support 3D Printing via Curing Kinetics and Rheology*

- Custom polymer design from commercial silicone + additives
- Rheological and curing kinetics characterization of a 3D printable silicone
- Suggestion of existing material characterization methods to bound 3D printing times of a curing material in soft robotics (using transient behavior)
- Zero support 3D printing of silicone with overhangs of over 30°
- Development of a custom-built open source silicone 3D printer
- Development of operation methods for custom printer

*3D Printed Sensor-Actuator Pair for Facial Rehabilitation*

- First 3D printed silicone facial wearable system
- Incorporation of discrete components into a silicone direct extrusion process
- Controlled path planning strategy for continuous extrusion
- Paired sensor-actuator system
- Exploration of actuator performance on a non-rigid surface (skin)
- Preliminary development of universal testing rig for skin/bone behavior with actuator
- Facial wearable as an on-body take home solution
- Possibility for graded force, contraction, and material properties
- Contribution to knowledge of composite behavior of fabric/silicone

## Practical Implications

Each paper in this thesis is designed to have a practical application by nature. The paired study of soft robotics with materials science as a basis goes beyond just the materials science or mechanical engineering alone. Practical applications of the work include:

*Using an Environmentally Benign and Degradable Elastomer in Soft Robotics*

- Accessible synthesis for a custom elastomer sheet
- Accessible synthesis for a UV curable elastomer
- Methods for how to incorporate green chemistry into soft robotics
- Methods for how to customize an elastomer from base chemicals

*Zero Support 3D Printing via Curing Kinetics and Rheology*

- Open-source 3D printing of soft actuators instead of molding
- Understanding of platinum-cure polymer curing for other soft device applications
- Techniques for improving print quality in curing mixed materials

*3D Printed Sensor-Actuator Pair for Facial Rehabilitation*

- Techniques for continuous extrusion patterning
- Techniques for incorporation of discrete components in silicone prints
- Techniques for removable support printing of silicone
- New device creation
- Strategies for addressing unusual actuation surfaces that change and move

## Limitations of the Current Work / Immediate Needs

All of the works rely on the incorporation of materials into additive manufacturing (either in the work itself or in future work). The current limitations lie in lack of knowledge of how many types of 3D printed models can be created using these additive manufacturing methods. Each work has a demonstration of the materials/additive manufacturing pairing via an actuator example, but the research did not explore the creation of a full robot and the required fully automated system.

### PGS-$CaCO_3$ and PGSI Limitations

The PGS-$CaCO_3$ work is limited by the lack of biodegradability data that confirms degradation via biological organisms versus degradation via other processes. PGS-$CaCO_3$ prepolymer is also not characterized for molecular weight and the final polymer is not characterized for crosslinking density. The PGSI chemistry and rheology needs to be more fully studied to integrate the pre-polymer into a UV curing additive manufacturing system. More exploration is needed in order to determine if the PGSI will be suited for a UV curing bath or an extrusion-based system with a focused UV light source. The PGS-CaCO3 and PGSI works also do not test curing kinetics or polymer bond structure.

### Zero-Support 3D Printing Limitations

The custom-built silicone 3D printer design and methodology will be released as open source information, but the limits of the printing method (maximum height, minimum wall thickness, range of filament diameters possible by varying speed) have not been fully explored. The printing system is also only characterized for one material family which has been optimized for performance in this particular printer. To use other Smooth-On materials, characterization for rheology and curing kinetics will be required for other chemistries. The printer mixer residence time is also relatively slow (~ 3 mins) so higher temperature printing will not be possible until the mixing volume is reduced. Extra additives to maintain filament shape, or extra mechanical alterations to the heating or extruder system of the printer may be required for new materials.

### Motor-Sensory Module Limitations

This research does not use the automated addition of multiple materials. To ensure repeatable behavior automated tools for placing the fabric, electrodes, and conductive fluid would need to be implemented. Although the modulus of the skin and bone modular surface membrane was within literature values for moduli of skin, it was also not designed to match the potentially varying looseness of the skin on the face.

## Open Research Questions

Additive manufacturing of soft robots is currently limited by the lack of implemented material processing techniques and printer designs to enable printing of multiple components. Ideally, one soft robot can be created as a whole with no post-

processing. This requires exploration of individual material printing processes for soft robotics as well as the combination of multiple processes. A generalized manufacturing loop concept is presented in Figure 1 in this section. Using synthesis from basic chemicals, to incorporation of multiple automated processes, to fidelity and performance analysis of the final product, the manufacturing loop yields many rich research opportunities including:

- Custom printer design for multiple fluids and components
- Path planning algorithms for multiple extruded soft materials and components
- Mechanical control of high viscosity soft material flow
- Rheological and chemical characterization of transient soft materials
- Mechanical and chemical influence of additives and modifiers
- Design of soft batteries, valves, circuits, and controllers
- Methods for incorporation of hard electronics into soft structures
- Multi-process manufacturing

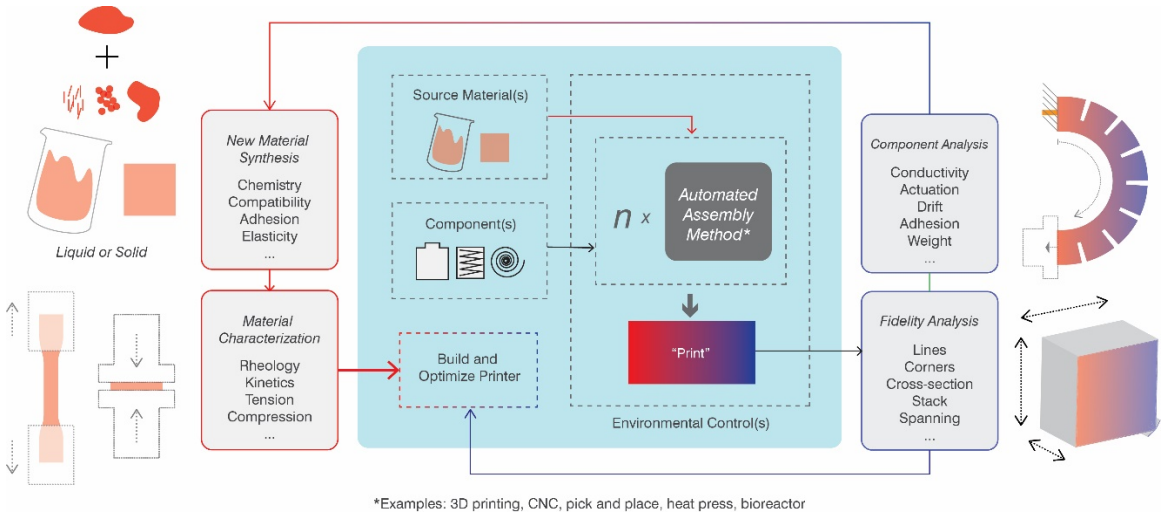


**Figure 1.** The example workflow for material choice, characterization, printer design, fidelity analysis, property optimization, and further optimization of both an additive manufacturing system and its material(s). Ideally, the chosen material should undergo various chemical, kinetics, and rheological characterization to determine expected material behavior. The additive manufacturing system should be designed to accommodate the processing needs in the fluid(s) with acceptable precision. Analysis of the printed structure should occur to determine the accuracy compared to the digital model. Performance results for the finished robot should be adequate depending on needed use. All results should be used to further optimize both the printer and the material.

As these research directions develop, it will become possible to additively manufacture functional and fully formed soft robots. These open questions rely on solutions from interdisciplinary collaboration, increasing design and manufacturing

complexity, and full understanding of the role of each individual material and its properties in the additive manufacturing system.

**Future Research**

A logical extension of these works is to incorporate more materials (both discrete hard components and fluids) into the existing custom printer system and to also expand the printer capabilities by incorporating attachments that facilitate UV curing (such as a direct UV laser) or more focused heating.

When focusing on the biodegradable elastomer synthesis, full materials characterization including more NMR and mechanical properties over time will improve the understanding of the mechanical behavior of the transient robot. Varying the synthesis and curing time to determine various amounts of crosslinking can also expand the material range to both lower and higher elastic moduli. Determining the biodegradation products over time for the PGS-$CaCO_3$ and PGSI will be helpful to determine the expected effects to the surrounding environment during degradation of the polymer. Most importantly, more work is needed to translate the PGSI pre-polymer into a form suitable for photopolymerization 3D printing, whether that be through direct extrusion, projection stereolithography, or other system. In the stereolithography case, solvents would potentially need to be analyzed and incorporated into the pre-polymer fluid to decrease its viscosity while still allowing for curing to take place with UV light. Further in the future, the polymers can be tested for their degradation behavior in vivo and potentially optimized for

incorporation of biodegradable soft robots into the human body. This can be beneficial for placement of medicine or diagnostic soft robots in the body.

When focusing on silicone 3D printing, the logical extension to the rheological and curing kinetics project is to complete a full set of rheology and curing kinetics for the most commonly used silicones in the Smooth-On family of products including Ecoflex 00-30 and Dragon Skin 30. A study of the dynamic as well as the isothermal curing kinetics would be worthwhile to more fully define the silicone curing behavior via mathematical modeling. Assuming that the power of the pumps and other equipment on the printer could be increased to handle the increased viscosity of some of the formulations, mapping the rheological and curing kinetics behavior would allow for researchers to tailor their ultimate desired material properties in their printed model (such as Young's modulus of the cured material) via choice of one or a mixture of several polymers. One weakness of the rheological characterization and curing kinetics characterization work is that it lacks a predictive equation where percent cure can be exactly determined at any time. By pairing this curing kinetics equation with printing experiments, more information on adhesion between layers can be gathered, and more exact required layer printing times can be determined from that to optimize the structural integrity of an unsupported layer of silicone before adding the next layer.

When focusing on the 3D printed motor-sensory module, the most immediate improvement will be the incorporation of multiple vacuum (or positive pressure)

actuators into a single mask. This mask can be an overlay of the muscle placement at the appropriate size in order to contract and expand in a complex manner similar to natural facial movements. More exploration is also needed on the optimization of the actuator dimensions to determine which is the best shape and size for highest and most controllable linear motion. Integration of automated components such as a pick and place machine to place the fabric, and an additional extruder head to insert the conductive fluid into the sensor are also needed. Increasing the elastic modulus of the silicone formulation, assuming that the equipment is powerful enough to extrude the potentially higher viscosity fluid, is a requirement for being able to reduce the overall thickness of the actuator walls. Incorporating fabric fibers or other strengthening additives into the silicone formulation itself will also improve the strength of the actuator. The testing method for the SB-MTS would also benefit from a more accurate representation of skin material properties in the membrane. This can be done by incorporating several different materials in a layered structure similar to real skin. The attachment points of the membrane to the underlying modular hard surface can also be improved by changing the amount of surface area of the membrane to better represent “looser” areas of skin on the face. For example, the skin in the area of the corner of the mouth moves more freely than the skin above the cheekbone. Perhaps in this case, instead of being a square membrane attached to a square frame, the membrane could have an irregular shape that when attached to the square frame to allow for more movement of the corner of the mouth area. The membrane can also be created with varying thickness or moduli in different areas for the same reason. By

increasing the accuracy of the membrane material properties, more accurate performance parameters can be evaluated in actuator design and optimization.

Each of these projects, though slightly different in scope, introduce novel concepts to additive manufacturing and materials science research for soft robotics to address the grand challenge of creating predictable, high quality, and scalable soft robot technologies. There are also more general themes enabled by this work that are worth considering, including the need for strategic interdisciplinary research, the enabling of more complex soft robot behavior, and ultimately, the increased accessibility and improvement of soft robot production via additive manufacturing. Interdisciplinary research in soft robotics will help improve device quality via material interaction, material property knowledge, and processing knowledge. More complex soft robot behavior and scalable production is enabled by both the improvement of additive manufacturing processes with one material as well as the ability to potentially incorporate materially disparate components into one device. Lastly, the ability to additively manufacture soft robots increases the likelihood that soft robotics can be created on the fly in the field, enabling greater on-demand production and customization. Overall, additive manufacturing can make soft robots work better for the user, and materials science makes the manufacturing work better for the robot.

# 6
# References


1. S. Kim, C. Laschi, B. Trimmer, Soft robotics: a bioinspired evolution in robotics. *Trends Biotechnol.* **31**, 287–294 (2013).

2. F. Ilievski, A. D. Mazzeo, R. F. Shepherd, X. Chen, G. M. Whitesides, Soft Robotics for Chemists. *Angew. Chem. Int. Ed.* **50**, 1890–1895 (2011).

3. D. Trivedi, C. D. Rahn, W. M. Kier, I. D. Walker, Soft robotics: Biological inspiration, state of the art, and future research. *Appl. Bionics Biomech.* **5**, 99–117 (2008).

4. S. I. Rich, R. J. Wood, C. Majidi, Untethered soft robotics. *Nat. Electron.* **1**, 102–112 (2018).

5. Y. L. Park, J. Santos, K. G. Galloway, E. C. Goldfield, R. J. Wood, in *2014 IEEE International Conference on Robotics and Automation (ICRA)* (2014), pp. 4805–4810.

6. E. T. Roche, M. A. Horvath, I. Wamala, A. Alazmani, S.-E. Song, W. Whyte, Z. Machaidze, C. J. Payne, J. C. Weaver, G. Fishbein, J. Kuebler, N. V. Vasilyev, D. J. Mooney, F. A. Pigula, C. J. Walsh, *Sci. Transl. Med.*, in press, doi:10.1126/scitranslmed.aaf3925.

7. S. Miyashita, S. Guitron, K. Yoshida, S. Li, D. D. Damian, D. Rus, in *Robotics and Automation (ICRA), 2016 IEEE International Conference on* (IEEE, 2016), pp. 909–916.

8. Food Case Study. *Soft Robot.*, (available at https://www.softroboticsinc.com/food-case-study/).

9. E. W. Hawkes, L. H. Blumenschein, J. D. Greer, A. M. Okamura, *Sci. Robot.*, in press, doi:10.1126/scirobotics.aan3028.

10. R. V. Martinez, J. L. Branch, C. R. Fish, L. Jin, R. F. Shepherd, R. M. D. Nunes, Z. Suo, G. M. Whitesides, Robotic Tentacles with Three-Dimensional Mobility Based on Flexible Elastomers. *Adv. Mater.* **25**, 205–212 (2013).

11. O. D. Yirmibesoglu, J. Morrow, S. Walker, W. Gosrich, R. A. Canizares, H. Kim, U. Daalkhaijav, C. Fleming, C. Branyan, Y. Menguc, Direct 3D Printing of Silicone Elastomer Soft Robots and Their Performance Comparison with Molded Counterparts. *2018 IEEE Int. Conf. Soft Robot. RoboSoft* (2018).

12. U. Daalkhaijav, O. D. Yirmibesoglu, S. Walker, Y. Mengüç, Rheological Modification of Liquid Metal for Additive Manufacturing of Stretchable Electronics. *Adv. Mater. Technol.* (2018), doi:10.1002/admt.201700351.

13. R. L. Truby, M. Wehner, A. K. Grosskopf, D. M. Vogt, S. G. M. Uzel, R. J. Wood, J. A. Lewis, *Adv. Mater.*, in press, doi:10.1002/adma.201706383.

14. A. D. Valentine, T. A. Busbee, J. W. Boley, J. R. Raney, A. Chortos, A. Kotikian, J. D. Berrigan, M. F. Durstock, J. A. Lewis, Hybrid 3D Printing of Soft Electronics. *Adv. Mater.* **29**, 1703817 (2017).

15. M. Wehner, R. L. Truby, D. J. Fitzgerald, B. Mosadegh, G. M. Whitesides, J. Lewis, R. J. Wood, An integrated design and fabrication strategy for entirely soft, autonomous robots (2016) (available at https://dash.harvard.edu/handle/1/29956021).

16. K. Sun, T.-S. Wei, B. Y. Ahn, J. Y. Seo, S. J. Dillon, J. A. Lewis, 3D Printing of Interdigitated Li-Ion Microbattery Architectures. *Adv. Mater.* **25**, 4539–4543 (2013).

17. T. Lu, E. J. Markvicka, Y. Jin, C. Majidi, Soft-Matter Printed Circuit Board with UV Laser Micropatterning. *ACS Appl. Mater. Interfaces*. **9**, 22055–22062 (2017).

18. Y. Lin, C. Cooper, M. Wang, J. J. Adams, J. Genzer, M. D. Dickey, Handwritten, Soft Circuit Boards and Antennas Using Liquid Metal Nanoparticles. *Small*. **11**, 6397–6403 (2015).

19. G.-Z. Yang, J. Bellingham, P. E. Dupont, P. Fischer, L. Floridi, R. Full, N. Jacobstein, V. Kumar, M. McNutt, R. Merrifield, B. J. Nelson, B. Scassellati, M. Taddeo, R. Taylor, M. Veloso, Z. L. Wang, R. Wood, *Sci. Robot.*, in press, doi:10.1126/scirobotics.aar7650.

20. J. Morrow, S. Hemleben, Y. Menguc, Directly Fabricating Soft Robotic Actuators With an Open-Source 3-D Printer. *IEEE Robot. Autom. Lett.* **2**, 277–281 (2017).

21. H. Yuk, X. Zhao, A New 3D Printing Strategy by Harnessing Deformation, Instability, and Fracture of Viscoelastic Inks. *Adv. Mater.*, 1704028 (2017).

22. I. D. Joshipura, H. R. Ayers, C. Majidi, M. D. Dickey, Methods to pattern liquid metals. *J. Mater. Chem. C*. **3**, 3834–3841 (2015).

23. C. Ladd, J.-H. So, J. Muth, M. D. Dickey, 3D Printing of Free Standing Liquid Metal Microstructures. *Adv. Mater.* **25**, 5081–5085 (2013).

24. B. Y. Ahn, S. B. Walker, S. C. Slimmer, A. Russo, A. Gupta, S. Kranz, E. B. Duoss, T. F. Malkowski, J. A. Lewis, Planar and Three-Dimensional Printing of Conductive Inks. *J. Vis. Exp. JoVE* (2011), doi:10.3791/3189.

25. M. A. Skylar-Scott, S. Gunasekaran, J. A. Lewis, Laser-assisted direct ink writing of planar and 3D metal architectures. *Proc. Natl. Acad. Sci.* **113**, 6137–6142 (2016).

26. B. Y. Ahn, E. B. Duoss, M. J. Motala, X. Guo, S.-I. Park, Y. Xiong, J. Yoon, R. G. Nuzzo, J. A. Rogers, J. A. Lewis, Omnidirectional Printing of Flexible, Stretchable, and Spanning Silver Microelectrodes. *Science*. **323**, 1590–1593 (2009).

27. A. Sydney Gladman, E. A. Matsumoto, R. G. Nuzzo, L. Mahadevan, J. A. Lewis, Biomimetic 4D printing. *Nat. Mater.* **15**, 413–418 (2016).

28. J. M. McCracken, A. Badea, M. E. Kandel, A. S. Gladman, D. J. Wetzel, G. Popescu, J. A. Lewis, R. G. Nuzzo, Programming Mechanical and Physicochemical Properties of 3D Hydrogel Cellular Microcultures via Direct Ink Writing. *Adv. Healthc. Mater.* **5**, 1025–1039 (2016).

29. Y. He, F. Yang, H. Zhao, Q. Gao, B. Xia, J. Fu, *Sci. Rep.*, in press, doi:10.1038/srep29977.

30. K. Fu, Y. Wang, C. Yan, Y. Yao, Y. Chen, J. Dai, S. Lacey, Y. Wang, J. Wan, T. Li, Z. Wang, Y. Xu, L. Hu, Graphene Oxide-Based Electrode Inks for 3D-Printed Lithium-Ion Batteries. *Adv. Mater.* **28**, 2587–2594 (2016).

31. J. O. Hardin, T. J. Ober, A. D. Valentine, J. A. Lewis, Microfluidic Printheads for Multimaterial 3D Printing of Viscoelastic Inks. *Adv. Mater.* **27**, 3279–3284 (2015).

32. T. J. Ober, D. Foresti, J. A. Lewis, Active mixing of complex fluids at the microscale. *Proc. Natl. Acad. Sci.* **112**, 12293–12298 (2015).

33. B. Duan, L. A. Hockaday, K. H. Kang, J. T. Butcher, 3D Bioprinting of heterogeneous aortic valve conduits with alginate/gelatin hydrogels. *J. Biomed. Mater. Res. A.* **101A**, 1255–1264 (2013).

34. D. B. Kolesky, R. L. Truby, A. S. Gladman, T. A. Busbee, K. A. Homan, J. A. Lewis, 3D Bioprinting of Vascularized, Heterogeneous Cell-Laden Tissue Constructs. *Adv. Mater.* **26**, 3124–3130 (2014).

35. A. Nadernezhad, N. Khani, G. A. Skvortsov, B. Toprakhisar, E. Bakirci, Y. Menceloglu, S. Unal, B. Koc, Multifunctional 3D printing of heterogeneous hydrogel structures. *Sci. Rep.* **6** (2016), doi:10.1038/srep33178.

36. R. Al, H. Ke, J. Ae, B. Wr, S. Rn, A multimaterial bioink method for 3D printing tunable, cell-compatible hydrogels., A Multi-Material Bioink Method for 3D Printing Tunable, Cell-Compatible Hydrogels. *Adv. Mater. Deerfield Beach Fla Adv. Mater. Deerfield Beach Fla*. **27**, **27**, 1607, 1607–1614 (2015).

37. W. Liu, Y. S. Zhang, M. A. Heinrich, F. De Ferrari, H. L. Jang, S. M. Bakht, M. M. Alvarez, J. Yang, Y.-C. Li, G. Trujillo-de Santiago, A. K. Miri, K. Zhu, P. Khoshakhlagh, G. Prakash, H. Cheng, X. Guan, Z. Zhong, J. Ju, G. H. Zhu, X. Jin, S. R. Shin, M. R. Dokmeci, A. Khademhosseini, *Adv. Mater.*, in press, doi:10.1002/adma.201604630.

38. L. Leng, A. McAllister, B. Zhang, M. Radisic, A. Günther, Mosaic Hydrogels: One-Step Formation of Multiscale Soft Materials. *Adv. Mater.* **24**, 3650–3658 (2012).

39. J. Visser, B. Peters, T. J. Burger, J. Boomstra, W. J. A. Dhert, F. P. W. Melchels, J. Malda, Biofabrication of multi-material anatomically shaped tissue constructs. *Biofabrication.* **5**, 35007 (2013).

40. H.-W. Kang, S. J. Lee, I. K. Ko, C. Kengla, J. J. Yoo, A. Atala, A 3D bioprinting system to produce human-scale tissue constructs with structural integrity. *Nat. Biotechnol.* **34**, 312–319 (2016).

41. D. Kokkinis, M. Schaffner, A. R. Studart, Multimaterial magnetically assisted 3D printing of composite materials. *Nat. Commun.* **6**, 8643 (2015).

42. R. R. Kohlmeyer, A. J. Blake, J. O. Hardin, E. A. Carmona, J. Carpena-Núñez, B. Maruyama, J. Daniel Berrigan, H. Huang, M. F. Durstock, Composite batteries: a simple yet universal approach to 3D printable lithium-ion battery electrodes. *J Mater Chem A.* **4**, 16856–16864 (2016).

43. T. Bhattacharjee, S. M. Zehnder, K. G. Rowe, S. Jain, R. M. Nixon, W. G. Sawyer, T. E. Angelini, Writing in the granular gel medium. *Sci. Adv.* **1**, e1500655 (2015).

44. C. S. O'Bryan, T. Bhattacharjee, S. Hart, C. P. Kabb, K. D. Schulze, I. Chilakala, B. S. Sumerlin, W. G. Sawyer, T. E. Angelini, Self-assembled micro-organogels for 3D printing silicone structures. *Sci. Adv.* **3**, e1602800 (2017).

45. T. J. Hinton, A. Hudson, K. Pusch, A. Lee, A. W. Feinberg, 3D Printing PDMS Elastomer in a Hydrophilic Support Bath via Freeform Reversible Embedding. *ACS Biomater. Sci. Eng.* **2**, 1781–1786 (2016).

46. C. B. Highley, C. B. Rodell, J. A. Burdick, Direct 3D Printing of Shear-Thinning Hydrogels into Self-Healing Hydrogels. *Adv. Mater.* **27**, 5075–5079 (2015).

47. T. J. Hinton, Q. Jallerat, R. N. Palchesko, J. H. Park, M. S. Grodzicki, H.-J. Shue, M. H. Ramadan, A. R. Hudson, A. W. Feinberg, Three-dimensional printing of complex biological structures by freeform reversible embedding of suspended hydrogels. *Sci. Adv.* **1**, e1500758 (2015).

48. G. M. Gratson, M. Xu, J. A. Lewis, Microperiodic structures: Direct writing of three-dimensional webs. *Nature*. **428**, 386–386 (2004).

49. Q. Gao, Y. He, J. Fu, A. Liu, L. Ma, Coaxial nozzle-assisted 3D bioprinting with built-in microchannels for nutrients delivery. *Biomaterials*. **61**, 203–215 (2015).

50. picsima3d. *picsima3d*, (available at http://www.picsima.com).

51. W. Wu, A. DeConinck, J. A. Lewis, Omnidirectional Printing of 3D Microvascular Networks. *Adv. Mater.* **23**, H178–H183 (2011).

52. J. T. Muth, D. M. Vogt, R. L. Truby, Y. Mengüç, D. B. Kolesky, R. J. Wood, J. A. Lewis, Embedded 3D Printing of Strain Sensors within Highly Stretchable Elastomers. *Adv. Mater.* **26**, 6307–6312 (2014).

53. R. L. Truby, M. Wehner, A. K. Grosskopf, D. M. Vogt, S. G. M. Uzel, R. J. Wood, J. A. Lewis, Soft Somatosensitive Actuators via Embedded 3D Printing. *Adv. Mater.* **30**, 1706383.

54. The Dow Chemical Company, SYLGARD 184 Silicone Elastomer, (available at https://consumer.dow.com/content/dam/dcc/documents/en-us/productdatasheet/11/11-31/11-3184-sylgard-184-elastomer.pdf?iframe=true).

55. The Dow Chemical Company, DOWSIL SE 1700 Adhesive.

56. Silicone Rubber - Platinum Cure. *Smooth- Inc*, (available at https://www.smooth-on.com/category/platinum-silicone/).

57. German RepRap GmbH, (available at https://www.germanreprap.com/myfactory/web/cms/home-en.aspx?WPParams=43CCD7D4B5DDE6B7C2E0B1CDE1C8B6B79495).

58. Our Process. *Carbon 3D*, (available at https://www.carbon3d.com/process/).

59. Discov3ry 2.0 Complete. *Struct. Print. Go Plast.*, (available at https://www.structur3d.io/discov3ry-2-complete/).

60. ACEO® Silicones - Introducing a New Material for 3D Printing. *ACEO*, (available at https://www.aceo3d.com/silicones/).

61. J. I. Lipton, D. Cohen, M. Heinz, M. Lobovsky, W. Parad, G. Bernstien, T. Li, J. Quartiere, K. Washington, A. Umaru, in *Solid Freeform Fabrciation Symposium* (2009).

62. J. I. Lipton, S. Angle, H. Lipson, in *2014 Annual International Solid Freeform Fabrication Symposium* (Laboratory for Freeform Fabrication and University of Texas Austin, TX, 2014), pp. 4–6.

63. A. Frutiger, J. T. Muth, D. M. Vogt, Y. Mengüç, A. Campo, A. D. Valentine, C. J. Walsh, J. A. Lewis, Capacitive Soft Strain Sensors via Multicore-Shell Fiber Printing. *Adv. Mater.* **27**, 2440–2446 (2015).

64. S. Shan, S. H. Kang, J. R. Raney, P. Wang, L. Fang, F. Candido, J. A. Lewis, K. Bertoldi, Multistable Architected Materials for Trapping Elastic Strain Energy. *Adv. Mater.* **27**, 4296–4301 (2015).

65. F. B. Coulter, A. Ianakiev, 4D Printing Inflatable Silicone Structures. *3D Print. Addit. Manuf.* **2**, 140–144 (2015).

66. J. U. Lind, T. A. Busbee, A. D. Valentine, F. S. Pasqualini, H. Yuan, M. Yadid, S.-J. Park, A. Kotikian, A. P. Nesmith, P. H. Campbell, J. J. Vlassak, J. A. Lewis, K. K. Parker, Instrumented cardiac microphysiological devices via multimaterial three-dimensional printing. *Nat. Mater.* **16**, 303–308 (2017).

67. M. M. Durban, J. M. Lenhardt, A. S. Wu, W. Small, T. M. Bryson, L. Perez-Perez, D. T. Nguyen, S. Gammon, J. E. Smay, E. B. Duoss, J. P. Lewicki, T. S. Wilson, *Macromol. Rapid Commun.*, in press, doi:10.1002/marc.201700563.

68. Silicone. *Carbon*, (available at https://www.carbon3d.com/materials/silicone/).

69. D. McCoul, S. Rosset, S. Schlatter, H. Shea, Inkjet 3D printing of UV and thermal cure silicone elastomers for dielectric elastomer actuators. *Smart Mater. Struct.* **26**, 125022 (2017).

70. D. Periard, E. Malone, H. Lipson, *Printing Embedded Circuits*.

71. German RepRap, *German RepRap LAM prints ECCO shoe sole* (https://www.youtube.com/watch?v=1fqMei2MEKU).

72. T. J. Wallin, J. H. Pikul, S. Bodkhe, B. N. Peele, B. C. Mac Murray, D. Therriault, B. W. McEnerney, R. P. Dillon, E. P. Giannelis, R. F. Shepherd, Click chemistry stereolithography for soft robots that self-heal. *J Mater Chem B* (2017), doi:10.1039/C7TB01605K.

73. A. Cazón, P. Morer, L. Matey, PolyJet technology for product prototyping: Tensile strength and surface roughness properties. *Proc. Inst. Mech. Eng. Part B J. Eng. Manuf.* **228**, 1664–1675 (2014).

74. A. Zatopa, S. Walker, Y. Menguc, Fully Soft 3D-Printed Electroactive Fluidic Valve for Soft Hydraulic Robots. *Soft Robot.* **5**, 258–271 (2018).

75. D. Drotman, S. Jadhav, M. Karimi, P. deZonia, M. T. Tolley, in *2017 IEEE International Conference on Robotics and Automation (ICRA)* (2017), pp. 5532–5538.

76. W. Crooks, G. Vukasin, M. O'Sullivan, W. Messner, C. Rogers, Fin Ray® Effect Inspired Soft Robotic Gripper: From the RoboSoft Grand Challenge toward Optimization. *Front. Robot. AI.* **3** (2016), doi:10.3389/frobt.2016.00070.

77. N. W. Bartlett, M. T. Tolley, J. T. B. Overvelde, J. C. Weaver, B. Mosadegh, K. Bertoldi, G. M. Whitesides, R. J. Wood, A 3D-printed, functionally graded soft robot powered by combustion. *Science*. **349**, 161–165 (2015).

78. R. MacCurdy, R. Katzschmann, Y. Kim, D. Rus, in *Robotics and Automation (ICRA), 2016 IEEE International Conference on* (IEEE, 2016; http://ieeexplore.ieee.org/abstract/document/7487576/), pp. 3878–3885.

79. J.-Y. Lee, J. An, C. K. Chua, Fundamentals and applications of 3D printing for novel materials. *Appl. Mater. Today*. **7**, 120–133 (2017).

80. Q. Ge, A. H. Sakhaei, H. Lee, C. K. Dunn, N. X. Fang, M. L. Dunn, Multimaterial 4D Printing with Tailorable Shape Memory Polymers. *Sci. Rep.* **6** (2016), doi:10.1038/srep31110.

81. B. N. Peele, T. J. Wallin, H. Zhao, R. F. Shepherd, 3D printing antagonistic systems of artificial muscle using projection stereolithography. *Bioinspir. Biomim.* **10**, 55003 (2015).

82. D. K. Patel, A. H. Sakhaei, M. Layani, B. Zhang, Q. Ge, S. Magdassi, Highly Stretchable and UV Curable Elastomers for Digital Light Processing Based 3D Printing. *Adv. Mater.* **29**, 1606000 (2017).

83. J. Odent, T. J. Wallin, W. Pan, K. Kruemplestaedter, R. F. Shepherd, E. P. Giannelis, Highly Elastic, Transparent, and Conductive 3D-Printed Ionic Composite Hydrogels. *Adv. Funct. Mater.* **27**, 1701807 (2017).

84. Y. Mao, K. Yu, M. S. Isakov, J. Wu, M. L. Dunn, H. Jerry Qi, Sequential Self-Folding Structures by 3D Printed Digital Shape Memory Polymers. *Sci. Rep.* **5** (2015), doi:10.1038/srep13616.

85. D. Raviv, W. Zhao, C. McKnelly, A. Papadopoulou, A. Kadambi, B. Shi, S. Hirsch, D. Dikovsky, M. Zyracki, C. Olguin, R. Raskar, S. Tibbits, Active Printed Materials for Complex Self-Evolving Deformations. *Sci. Rep.* **4** (2015), doi:10.1038/srep07422.

86. S. Tibbits, 4D Printing: Multi-Material Shape Change. *Archit. Des.* **84**, 116–121 (2014).

87. J. Wu, C. Yuan, Z. Ding, M. Isakov, Y. Mao, T. Wang, M. L. Dunn, H. J. Qi, *Sci. Rep.*, in press, doi:10.1038/srep24224.

88. Tango, (available at http://www.stratasys.com/materials/search/tango).

89. Vero Clear, (available at http://www.stratasys.com/materials/search/veroclear).

90. E. MacDonald, R. Wicker, *Science*, in press, doi:10.1126/science.aaf2093.

91. 3D Printing multifunctionality: structures with electronics.

92. SYLGARD<SUP>®</SUP> 184 761036. *Sigma-Aldrich*, (available at https://www.sigmaaldrich.com/catalog/product/aldrich/761036).

93. FTIR Basics - US, (available at https://www.thermofisher.com/us/en/home/industrial/spectroscopy-elemental-isotope-analysis/spectroscopy-elemental-isotope-analysis-learning-center/molecular-spectroscopy-information/ftir-information/ftir-basics.html).

94. J. Rueben, S. Walker, S. Huhn, J. Simonsen, Y. Mengüç, Developing a UV-Curable, Environmentally Benign and Degradable Elastomer for Soft Robotics. *MRS Adv.* **3**, 1551–1556 (2018).

95. I.-K. Hong, S. Lee, Cure kinetics and modeling the reaction of silicone rubber. *J. Ind. Eng. Chem.* **19**, 42–47 (2013).

96. L. M. Lopez, A. B. Cosgrove, J. P. Hernandez-Ortiz, T. A. Osswald, Modeling the vulcanization reaction of silicone rubber. *Polym. Eng. Sci.* **47**, 675–683 (2007).

97. S. Sourour, M. R. Kamal, Differential scanning calorimetry of epoxy cure: isothermal cure kinetics. *Thermochim. Acta*. **14**, 41–59 (1976).

98. M. R. Kamal, S. Sourour, Kinetics and thermal characterization of thermoset cure. *Polym. Eng. Sci.* **13**, 59–64 (1973).

99. TA Instruments, A Review of DSC Kinetics Methods (TA073), (available at http://www.tainstruments.com/pdf/literature/TA073.pdf).

100. M. Frigione, C. E. Corcione, Rheological and kinetic characterization of UV photopolymerizable formulations as a function of the boehmite nanoparticle content. *Open Mater. Sci. J.* **6**, 68–76 (2012).

101. C. Decker, The use of UV irradiation in polymerization. *Polym. Int.* **45**, 133–141 (1998).

102. J. L. Ifkovits, J. A. Burdick, Review: Photopolymerizable and Degradable Biomaterials for Tissue Engineering Applications. *Tissue Eng.* **13**, 2369–2385 (2007).

103. C. K. Chua, S. M. Chou, T. S. Wong, A study of the state-of-the-art rapid prototyping technologies. *Int. J. Adv. Manuf. Technol.* **14**, 146–152 (1998).

104. C. Decker, T. Nguyen Thi Viet, D. Decker, E. Weber-Koehl, UV-radiation curing of acrylate/epoxide systems. *Polymer*. **42**, 5531–5541 (2001).

105. R. Landers, U. Hübner, R. Schmelzeisen, R. Mülhaupt, Rapid prototyping of scaffolds derived from thermoreversible hydrogels and tailored for applications in tissue engineering. *Biomaterials*. **23**, 4437–4447 (2002).

106. J. E. Smay, G. M. Gratson, R. F. Shepherd, J. Cesarano, J. A. Lewis, others, Directed colloidal assembly of 3D periodic structures. *Adv. Mater.* **14**, 1279–1283 (2002).

107. A. Franck, Viscoelasticity and dynamic mechanical testing. *TA Instrum. New Castle USA AN004*.

108. TA Instruments, Understanding Rheology of Structured Fluids, (available at http://www.tainstruments.com/pdf/literature/AAN016_V1_U_StructFluids.pdf).

109. L. Weng, X. Chen, W. Chen, Rheological Characterization of in situ Crosslinkable Hydrogels Formulated from Oxidized Dextran and N-Carboxyethyl Chitosan. *Biomacromolecules*. **8**, 1109–1115 (2007).

110. M. Wehner, M. T. Tolley, Y. Menguc, Y.-L. Park, A. Mozeika, Y. Ding, C. Onal, R. F. Shepherd, G. M. Whitesides, R. J. Wood, Pneumatic Energy Sources for Autonomous and Wearable Soft Robotics. *Soft Robot.* **2** (2014).

111. S. Walker, U. Daalkhaijav, D. Thrush, C. Branyan, O. D. Yirmibesoglu, G. Olson, Y. Menguc, Zero - Support 3D Printing of Thermoset Silicone via Simultaneous Control of Both Reaction Kinetics and Transient Rheology. *3D Print. Addit. Manuf.* **Submitted** (2018).

112. C. Gorsche, R. Harikrishna, S. Baudis, P. Knaack, B. Husar, J. Laeuger, H. Hoffmann, R. Liska, Real Time-NIR/MIR-Photorheology: A Versatile Tool for the in Situ Characterization of Photopolymerization Reactions. *Anal. Chem.* **89**, 4958–4968 (2017).

113. L. E. Schmidt, Y. Leterrier, J.-M. Vesin, M. Wilhelm, J.-A. E. Månson, Photorheology of Fast UV-Curing Multifunctional Acrylates. *Macromol. Mater. Eng.* **290**, 1115–1124 (2005).

114. B. G. Compton, J. A. Lewis, 3D-Printing of Lightweight Cellular Composites. *Adv. Mater.* **26**, 5930–5935 (2014).

115. P. J. Halley, M. E. Mackay, Chemorheology of thermosets—an overview. *Polym. Eng. Sci.* **36**, 593–609 (1996).

116. J. W. Stansbury, M. J. Idacavage, 3D printing with polymers: Challenges among expanding options and opportunities. *Dent. Mater.* **32**, 54–64 (2016).

117. J. R. Tumbleston, D. Shirvanyants, N. Ermoshkin, R. Janusziewicz, A. R. Johnson, D. Kelly, K. Chen, R. Pinschmidt, J. P. Rolland, A. Ermoshkin, E. T. Samulski, J. M. DeSimone, Continuous liquid interface production of 3D objects. *Science*. **347**, 1349–1352 (2015).

118. M. Larsson, J. Duffy, M. I. N. AB, An overview of measurement techniques for determination of yield stress. *Annu. Trans. Nord. Rheol. Soc.* **21**, 125–138 (2013).

119. F. P. W. Melchels, J. Feijen, D. W. Grijpma, A review on stereolithography and its applications in biomedical engineering. *Biomaterials*. **31**, 6121–6130 (2010).

120. B. Scientific, Contact Angle | Measurements | Biolin Scientific, (available at https://www.biolinscientific.com/measurements/contact-angle).

121. E. Schwahn, thesis, University of Nebraska-Lincoln (2015).

122. S. Li, D. M. Vogt, D. Rus, R. J. Wood, Fluid-driven origami-inspired artificial muscles. *Proc. Natl. Acad. Sci.* **114**, 13132–13137 (2017).

123. B. Mosadegh, P. Polygerinos, C. Keplinger, S. Wennstedt, R. F. Shepherd, U. Gupta, J. Shim, K. Bertoldi, C. J. Walsh, G. M. Whitesides, Pneumatic Networks for Soft Robotics that Actuate Rapidly. *Adv. Funct. Mater.* **24**, 2163–2170 (2014).

124. S. Walker, A. Firouzeh, M. Robertson, Y. Menguc, J. Paik, 3D Printed Motor-Sensory Module for Facial Rehabilitation. *Soft Robot. Plan. Submiss.* (2018).

125. L. Mullins, Softening of Rubber by Deformation. *Rubber Chem. Technol.* **42**, 339–362 (1969).

126. H. Zhao, B. Chen, F. Gu, Q.-X. Huang, J. Garcia, Y. Chen, C. Tu, B. Benes, H. Zhang, D. Cohen-Or, Connected fermat spirals for layered fabrication. *ACM Trans. Graph.* **35**, 1–10 (2016).

127. PolyJet Technology for 3D Printing | Stratasys, (available at http://www.stratasys.com/polyjet-technology).

128. D. Rus, M. T. Tolley, Design, fabrication and control of soft robots. *Nature*. **521**, 467–475 (2015).

129. Y. Li, G. A. Thouas, Q.-Z. Chen, Biodegradable soft elastomers: synthesis/properties of materials and fabrication of scaffolds. *RSC Adv.*, 8829–8242 (2012).

130. P. T. Anastas, *Green chemistry : theory and practice* (Oxford University Press, Oxford England ; New York, 1998).

131. S. Valdes, I. Urza, P. Pounds, S. Singh, in *Robotics: Science and Systems Workshop on Robotics for Environmental Monitoring* (Citeseer, 2012; http://citeseerx.ist.psu.edu/viewdoc/download?doi=10.1.1.470.4128&rep=rep1&type=pdf).

132. J. C. Breger, C. Yoon, R. Xiao, H. R. Kwag, M. O. Wang, J. P. Fisher, T. D. Nguyen, D. H. Gracias, Self-Folding Thermo-Magnetically Responsive Soft Microgrippers. *ACS Appl. Mater. Interfaces*. **7**, 3398–3405 (2015).

133. D. J. Mulla, Twenty five years of remote sensing in precision agriculture: Key advances and remaining knowledge gaps. *Biosyst. Eng.* **114**, 358–371 (2013).

134. A. Suprem, N. Mahalik, K. Kim, A review on application of technology systems, standards and interfaces for agriculture and food sector. *Comput. Stand. Interfaces.* **35**, 355–364 (2013).

135. G. Muscato, F. Bonaccorso, L. Cantelli, D. Longo, C. D. Melita, Volcanic Environments: Robots for Exploration and Measurement. *IEEE Robot. Autom. Mag.* **19**, 40–49 (2012).

136. R. R. Murphy, J. Peschel, C. Arnett, D. Martin, in *2012 IEEE International Symposium on Safety, Security, and Rescue Robotics (SSRR)* (2012), pp. 1–4.

137. J.-J. Cabibihan, S. Pattofatto, M. Jomaa, A. Benallal, M. C. Carrozza, Towards Humanlike Social Touch for Sociable Robotics and Prosthetics: Comparisons on the Compliance, Conformance and Hysteresis of Synthetic and Human Fingertip Skins. *ArXiv09093559 Phys.* (2009) (available at http://arxiv.org/abs/0909.3559).

138. S. Bauer, S. Bauer-Gogonea, I. Graz, M. Kaltenbrunner, C. Keplinger, R. Schwödiauer, 25th Anniversary Article: A Soft Future: From Robots and Sensor Skin to Energy Harvesters. *Adv. Mater.* **26**, 149–162 (2014).

139. R. Shankar, T. K. Ghosh, R. J. Spontak, Dielectric elastomers as next-generation polymeric actuators. *Soft Matter*. **3**, 1116 (2007).

140. S. Shian, K. Bertoldi, D. R. Clarke, Dielectric Elastomer Based "Grippers" for Soft Robotics. *Adv. Mater.* **27**, 6814–6819 (2015).

141. B. Laubie, A. Ohannessian, V. Desjardin, P. Germain, Methodology to Assess Silicone (Bio)Degradation and its Effects on Microbial Diversity. *J. Polym. Environ.* **20**, 1019–1026 (2012).

142. B. D. Ratner, A. S. Hoffman, F. J. Schoen, J. E. Lemons, *Biomaterials Science: An Introduction to Materials in Medicine* (Academic Press, 2004).

143. W. M. Saltzman, *Tissue Engineering: Engineering Principles for the Design of Replacement Organs and Tissues* (Oxford University Press, 2004).

144. Dow Corning, Fascinating Silicone™ Chemistry – How Polydimethylsiloxane Degrades, (available at http://www.dowcorning.com/content/discover/discoverchem/how-si-degrades.aspx).

145. Y. Fu, W. J. Kao, Drug Release Kinetics and Transport Mechanisms of Non-degradable and Degradable Polymeric Delivery Systems. *Expert Opin. Drug Deliv.* **7**, 429–444 (2010).

146. W. M. Saltzman, *Drug Delivery: Engineering Principles for Drug Therapy* (Oxford University Press, 2001).

147. L. Han, J. Dai, L. Zhang, S. Ma, J. Deng, R. Zhang, J. Zhu, Diisocyanate free and melt polycondensation preparation of bio-based unsaturated poly(ester-urethane)s and their properties as UV curable coating materials. *RSC Adv.* **4**, 49471–49477 (2014).

148. The Dow Chemical Company, Product Safety Assessment: DOW™ Acrylic Acid, (available at http://msdssearch.dow.com/PublishedLiteratureDOWCOM/dh_096d/0901b8038096dabc.pdf?filepath=productsafety/pdfs/noreg/233-00269.pdf&fromPage=GetDoc).

149. B. C. Mac Murray, X. An, S. S. Robinson, I. M. van Meerbeek, K. W. O'Brien, H. Zhao, R. F. Shepherd, Poroelastic Foams for Simple Fabrication of Complex Soft Robots. *Adv. Mater.* **27**, 6334–6340 (2015).

150. J. Guan, M. S. Sacks, E. J. Beckman, W. R. Wagner, Synthesis, characterization, and cytocompatibility of elastomeric, biodegradable poly(ester-urethane)ureas based on poly(caprolactone) and putrescine. *J. Biomed. Mater. Res.* **61**, 493–503 (2002).

151. C. L. E. Nijst, J. P. Bruggeman, J. M. Karp, L. Ferreira, A. Zumbuehl, C. J. Bettinger, R. Langer, Synthesis and Characterization of Photocurable Elastomers from Poly(glycerol-co-sebacate). *Biomacromolecules.* **8**, 3067–3073 (2007).

152. M. Kharaziha, M. Nikkhah, S.-R. Shin, N. Annabi, N. Masoumi, A. K. Gaharwar, G. Camci-Unal, A. Khademhosseini, PGS:Gelatin nanofibrous scaffolds with tunable mechanical and structural properties for engineering cardiac tissues. *Biomaterials.* **34**, 6355–6366 (2013).

153. Y. Wang, G. A. Ameer, B. J. Sheppard, R. Langer, A tough biodegradable elastomer. *Nat. Biotechnol.* **20**, 602 (2002).

154. Conference on the Application of External Power in Prosthetics and Orthotics: Lake Arrowhead, Calif., *The application of external power in prosthetics and orthotics; a report.* (Washington, National Academy of Sciences, National Research Council, 1961), *Publication (National Research Council (U.S.)) ; 874*.

155. W. M. Kier, K. K. Smith, Tongues, tentacles and trunks: the biomechanics of movement in muscular-hydrostats. *Zool. J. Linn. Soc.* **83**, 307–324 (1985).

156. R. F. Shepherd, F. Ilievski, W. Choi, S. A. Morin, A. A. Stokes, A. D. Mazzeo, X. Chen, M. Wang, G. M. Whitesides, Multigait soft robot. *Proc. Natl. Acad. Sci.* **108**, 20400–20403 (2011).

157. A. A. Stokes, R. F. Shepherd, S. A. Morin, F. Ilievski, G. M. Whitesides, A Hybrid Combining Hard and Soft Robots. *Soft Robot.* **1**, 70–74 (2014).

158. S. A. Morin, Y. Shevchenko, J. Lessing, S. W. Kwok, R. F. Shepherd, A. A. Stokes, G. M. Whitesides, Using "Click-e-Bricks" to Make 3D Elastomeric Structures. *Adv. Mater.* **26**, 5991–5999 (2014).

159. S. A. Morin, S. W. Kwok, J. Lessing, J. Ting, R. F. Shepherd, A. A. Stokes, G. M. Whitesides, Elastomeric Tiles for the Fabrication of Inflatable Structures. *Adv. Funct. Mater.* **24**, 5541–5549 (2014).

160. C.-P. Chou, B. Hannaford, Measurement and modeling of McKibben pneumatic artificial muscles. *IEEE Trans. Robot. Autom.* **12**, 90–102 (1996).

161. S. Davis, N. Tsagarakis, J. Canderle, D. G. Caldwell, Enhanced Modelling and Performance in Braided Pneumatic Muscle Actuators. *Int. J. Robot. Res.* **22**, 213–227 (2003).

162. G. Chen, L. Fu, M. T. Pham, T. Redarce, in *2013 IEEE International Conference on Mechatronics and Automation (ICMA)* (2013), pp. 243–248.

163. F. J. Chen, S. Dirven, W. L. Xu, X. N. Li, Soft Actuator Mimicking Human Esophageal Peristalsis for a Swallowing Robot. *IEEEASME Trans. Mechatron.* **19**, 1300–1308 (2014).

164. L. D. Chambers, J. Winfield, I. Ieropoulos, J. Rossiter, in *SPIE Smart Structures and Materials+ Nondestructive Evaluation and Health Monitoring* (International Society for Optics and Photonics, 2014; http://proceedings.spiedigitallibrary.org/proceeding.aspx?articleid=1845843), p. 90560B–90560B.

165. A. Stoica, in *Advanced Technologies for Enhanced Quality of Life, 2009. AT-EQUAL '09.* (2009), pp. 47–51.

166. S. Miyashita, S. Guitron, M. Ludersdorfer, C. Sung, D. Rus, in *IEEE International Conference on Robotics and Automation (ICRA), submitted* (http://shu21th.sakura.ne.jp/file/ICRA2015v26Final.pdf).

167. B. A. Trimmer, H.-T. Lin, A. Baryshyan, G. G. Leisk, D. L. Kaplan, in *2012 4th IEEE RAS EMBS International Conference on Biomedical Robotics and Biomechatronics (BioRob)* (2012), pp. 599–605.

168. S. Fusco, M. S. Sakar, S. Kennedy, C. Peters, R. Bottani, F. Starsich, A. Mao, G. A. Sotiriou, S. Pané, S. E. Pratsinis, D. Mooney, B. J. Nelson, An Integrated Microrobotic Platform for On-Demand, Targeted Therapeutic Interventions. *Adv. Mater.* **26**, 952–957 (2014).

169. L. V. Thomas, P. D. Nair, (Citric acid–co–polycaprolactone triol) polyester. *Biomatter*. **1**, 81–90 (2011).

170. C. Xu, C. Xu, J. Zheng, A novel dielectric elastomer actuator based on polyvinyl alcohol hydrogel electrodes. *ArXiv Prepr. ArXiv14092611* (2014) (available at http://arxiv.org/abs/1409.2611).

171. J. Yang, A. R. Webb, G. A. Ameer, Novel Citric Acid-Based Biodegradable Elastomers for Tissue Engineering. *Adv. Mater.* **16**, 511–516 (2004).

172. D. S. Ogunniyi, Castor oil: A vital industrial raw material. *Bioresour. Technol.* **97**, 1086–1091 (2006).

173. C. A. G. Quispe, C. J. R. Coronado, J. A. Carvalho Jr., Glycerol: Production, consumption, prices, characterization and new trends in combustion. *Renew. Sustain. Energy Rev.* **27**, 475–493 (2013).

174. Oregon. Environmental Toxicology Section. Calcium Carbonate "lime, Limewater" (1998), (available at http://library.state.or.us/repository/2008/200808011132585/).

175. R. Rai, M. Tallawi, A. Grigore, A. R. Boccaccini, Synthesis, properties and biomedical applications of poly(glycerol sebacate) (PGS): A review. *Prog. Polym. Sci.* **37**, 1051–1078 (2012).

176. S. Liang, W. D. Cook, Q. Chen, Physical characterization of poly(glycerol sebacate)/Bioglass® composites. *Polym. Int.* **61**, 17–22 (2012).

177. Q.-Z. Chen, H. Ishii, G. A. Thouas, A. R. Lyon, J. S. Wright, J. J. Blaker, W. Chrzanowski, A. R. Boccaccini, N. N. Ali, J. C. Knowles, S. E. Harding, An elastomeric patch derived from poly(glycerol sebacate) for delivery of embryonic stem cells to the heart. *Biomaterials.* **31**, 3885–3893 (2010).

178. Safety Data Sheet: Vinegar (2014), (available at https://www.fishersci.com/content/dam/fishersci/en_US/documents/programs/education/regulatory-documents/sds/chemicals/chemicals-v/S25623.pdf).

179. Sebacic Acid Material Safety Data Sheet (2015), (available at http://www.sigmaaldrich.com/MSDS/MSDS/DisplayMSDSPage.do?country=US&language=en&productNumber=283258&brand=ALDRICH&PageToGoToURL=http%3A%2F%2Fwww.sigmaaldrich.com%2Fcatalog%2Fproduct%2Faldrich%2F283258%3Flang%3Den).

180. Material Safety Data Sheet: Vinegar (2012), (available at http://www.flinnsci.com/Documents/MSDS/UV/Vinegar.pdf).

181. R. Dobson, V. Gray, K. Rumbold, Microbial utilization of crude glycerol for the production of value-added products. *J. Ind. Microbiol. Biotechnol.* **39**, 217–226 (2012).

182. Glycerol MSDS (2016), (available at http://www.sigmaaldrich.com/MSDS/MSDS/DisplayMSDSPage.do?country=US&language=en&productNumber=G7893&brand=SIAL&PageToGoToURL=http%3A%2F%2Fwww.sigmaaldrich.com%2Fcatalog%2Fsearch%3Fterm%3Dglycerol%26interface%3DAll%26N%3D0%2B%26mode%3Dpartialmax%26lang%3Den%26region%3DUS%26focus%3Dproduct).

183. Safety Data Sheet, Calcium Carbonate (2014), (available at https://www.avantormaterials.com/documents/MSDS/usa/sap/00002948.pdf).

184. Z.-J. Sun, L. Wu, W. Huang, C. Chen, Y. Chen, X.-L. Lu, X.-L. Zhang, B.-F. Yang, D.-L. Dong, Glycolic acid modulates the mechanical property and degradation of poly(glycerol, sebacate, glycolic acid). *J. Biomed. Mater. Res. A.* **92A**, 332–339 (2010).

185. A. Patel, A. K. Gaharwar, G. Iviglia, H. Zhang, S. Mukundan, S. M. Mihaila, D. Demarchi, A. Khademhosseini, Highly elastomeric poly(glycerol sebacate)-co-poly(ethylene glycol) amphiphilic block copolymers. *Biomaterials*. **34**, 3970–3983 (2013).

186. I. H. Jaafar, M. M. Ammar, S. S. Jedlicka, R. A. Pearson, J. P. Coulter, Spectroscopic evaluation, thermal, and thermomechanical characterization of poly(glycerol-sebacate) with variations in curing temperatures and durations. *J. Mater. Sci.* **45**, 2525–2529 (2010).

187. Q.-Z. Chen, A. Bismarck, U. Hansen, S. Junaid, M. Q. Tran, S. E. Harding, N. N. Ali, A. R. Boccaccini, Characterisation of a soft elastomer poly(glycerol sebacate) designed to match the mechanical properties of myocardial tissue. *Biomaterials*. **29**, 47–57 (2008).

188. S.-L. Liang, W. D. Cook, G. A. Thouas, Q.-Z. Chen, The mechanical characteristics and in vitro biocompatibility of poly(glycerol sebacate)-Bioglass® elastomeric composites. *Biomaterials*. **31**, 8516–8529 (2010).

189. V. Krishnan, T. Lakshmi, Bioglass: A novel biocompatible innovation. *J. Adv. Pharm. Technol. Res.* **4**, 78–83 (2013).

190. J. R. Jones, Review of bioactive glass: From Hench to hybrids. *Acta Biomater.* **9**, 4457–4486 (2013).

191. C. M. Bellingham, M. A. Lillie, J. M. Gosline, G. M. Wright, B. C. Starcher, A. J. Bailey, K. A. Woodhouse, F. W. Keeley, Recombinant human elastin polypeptides self-assemble into biomaterials with elastin-like properties. *Biopolymers*. **70**, 445–455 (2003).

192. R. Olsson, Inbound, Controlled, Air-Releasable, Unrecoverable Systems, (available at http://www.darpa.mil/program/inbound-controlled-air-reasonable-unrecoverable-systems).

193. B. Mosadegh, P. Polygerinos, C. Keplinger, S. Wennstedt, R. F. Shepherd, U. Gupta, J. Shim, K. Bertoldi, C. J. Walsh, G. M. Whitesides, Pneumatic Networks for Soft Robotics that Actuate Rapidly. *Adv. Funct. Mater.* **24**, 2163–2170 (2014).

194. F. Ilievski, A. D. Mazzeo, R. F. Shepherd, X. Chen, G. M. Whitesides, Soft Robotics for Chemists. *Angew. Chem. Int. Ed.* **50**, 1890–1895 (2011).

195. M. J. Kim, M. Y. Hwang, J. Kim, D. J. Chung, M. J. Kim, M. Y. Hwang, J. Kim, D. J. Chung, Biodegradable and Elastomeric Poly(glycerol sebacate) as a Coating Material for Nitinol Bare Stent, Biodegradable and Elastomeric Poly(glycerol sebacate) as a Coating Material for Nitinol Bare Stent. *BioMed Res. Int. BioMed Res. Int.* **2014**, **2014**, e956952 (2014).

196. X. Zhao, Y. Wu, Y. Du, X. Chen, B. Lei, Y. Xue, P. X. Ma, A highly bioactive and biodegradable poly(glycerol sebacate)–silica glass hybrid elastomer with tailored mechanical properties for bone tissue regeneration. *J. Mater. Chem. B.* **3**, 3222–3233 (2015).

197. S. Walker, J. Rueben, T. V. Volkenburg, S. Hemleben, C. Grimm, J. Simonsen, Y. Mengüç, Using an environmentally benign and degradable elastomer in soft robotics. *Int. J. Intell. Robot. Appl.*, 1–19 (2017).

198. J. Shintake, H. Sonar, E. Piskarev, J. Paik, D. Floreano, Soft Pneumatic Gelatin Actuator for Edible Robotics. *ArXiv170301423 Cs* (2017) (available at http://arxiv.org/abs/1703.01423).

199. H. Daemi, S. Rajabi-Zeleti, H. Sardon, M. Barikani, A. Khademhosseini, H. Baharvand, A robust super-tough biodegradable elastomer engineered by supramolecular ionic interactions. *Biomaterials.* **84**, 54–63 (2016).

200. Y. Wang, G. A. Ameer, B. J. Sheppard, R. Langer, A tough biodegradable elastomer. *Nat. Biotechnol.* **20**, 602 (2002).

201. C. L. E. Nijst, J. P. Bruggeman, J. M. Karp, L. Ferreira, A. Zumbuehl, C. J. Bettinger, R. Langer, Synthesis and Characterization of Photocurable Elastomers from Poly(glycerol-co-sebacate). *Biomacromolecules*. **8**, 3067–3073 (2007).

202. Sigma-Aldrich, Product Specification, Acryloyl Chloride (2004).

203. A. I. Magalhães, J. C. de Carvalho, J. D. C. Medina, C. R. Soccol, Downstream process development in biotechnological itaconic acid manufacturing. *Appl. Microbiol. Biotechnol.* **101**, 1–12 (2017).

204. D. G. Barrett, T. J. Merkel, J. C. Luft, M. N. Yousaf, One-Step Syntheses of Photocurable Polyesters Based on a Renewable Resource. *Macromolecules*. **43**, 9660–9667 (2010).

205. X. Li, J. Shi, K. Wu, F. Luo, S. Zhang, X. Guan, M. Lu, A novel pH-sensitive aqueous supramolecular structured photoinitiator comprising of 6-modified per-methylated β-cyclodextrin and 1-hydroxycyclohexyl phenyl ketone. *J. Photochem. Photobiol. Chem.* **333**, 18–25 (2017).

206. Sigma-Aldrich, “1-hydroxycyclohexyl phenyl ketone” (Safety Data Sheet, Sigma-Aldrich, 2014).

207. Ciba Specialty Chemicals, “Ciba® IRGACURE® 184” (2001), p. 3.

208. C. M. Bellingham, M. A. Lillie, J. M. Gosline, G. M. Wright, B. C. Starcher, A. J. Bailey, K. A. Woodhouse, F. W. Keeley, Recombinant human elastin polypeptides self-assemble into biomaterials with elastin-like properties. *Biopolymers.* **70**, 445–455 (2003).

209. P. Y. Bruice, *Organic Chemistry, 6th Edition* (Prentice Hall, 6 edition., 2009).

210. Organic Division Information, (available at https://www.chem.wisc.edu/areas/organic/index-chem.htm).

211. Sigma-Aldrich, SDS Itaconic Acid.

212. G. M. Gratson, J. A. Lewis, Phase behavior and rheological properties of polyelectrolyte inks for direct-write assembly. *Langmuir*. **21**, 457–464 (2005).

213. D. Kokkinis, F. Bouville, A. R. Studart, 3D Printing of Materials with Tunable Failure via Bioinspired Mechanical Gradients. *Adv. Mater.*, 1705808 (2018).

214. J. R. Raney, J. A. Lewis, Printing mesoscale architectures. *MRS Bull.* **40**, 943–950 (2015).

215. R. L. Truby, J. A. Lewis, Printing soft matter in three dimensions. *Nature*. **540**, 371–378 (2016).

216. J. E. Smay, J. Cesarano, J. A. Lewis, Colloidal Inks for Directed Assembly of 3-D Periodic Structures. *Langmuir*. **18**, 5429–5437 (2002).

217. M. Wehner, B. Quinlivan, P. M. Aubin, E. Martinez-Villalpando, M. Baumann, L. Stirling, K. Holt, R. Wood, C. Walsh, in *Robotics and Automation (ICRA), 2013 IEEE International Conference on* (IEEE, 2013), pp. 3362–3369.

218. Y. Mengüç, Y.-L. Park, H. Pei, D. Vogt, P. M. Aubin, E. Winchell, L. Fluke, L. Stirling, R. J. Wood, C. J. Walsh, Wearable soft sensing suit for human gait measurement. *Int. J. Robot. Res.* **33**, 1748–1764 (2014).

219. P. Polygerinos, Z. Wang, K. C. Galloway, R. J. Wood, C. J. Walsh, Soft robotic glove for combined assistance and at-home rehabilitation. *Robot. Auton. Syst.* **73**, 135–143 (2015).

220. H. In, B. B. Kang, M. Sin, K.-J. Cho, Exo-Glove: A Wearable Robot for the Hand with a Soft Tendon Routing System. *IEEE Robot. Autom. Mag.* **22**, 97–105 (2015).

221. P. Polygerinos, K. C. Galloway, E. Savage, M. Herman, K. O'Donnell, C. J. Walsh, in *Robotics and Automation (ICRA), 2015 IEEE International Conference on* (IEEE, 2015), pp. 2913–2919.

222. T. Noritsugu, M. Takaiwa, D. Sasaki, in *2008 15th International Conference on Mechatronics and Machine Vision in Practice* (2008), pp. 539–544.

223. Y.-L. Park, B. Chen, C. Majidi, R. J. Wood, R. Nagpal, E. Goldfield, in *Intelligent Robots and Systems (IROS), 2012 IEEE/RSJ International Conference on* (IEEE, 2012), pp. 1595–1602.

224. N. W. Bartlett, V. Lyau, W. A. Raiford, D. Holland, J. B. Gafford, T. D. Ellis, C. J. Walsh, A Soft Robotic Orthosis for Wrist Rehabilitation. *J. Med. Devices*. **9**, 30918 (2015).

225. K. Subramanyam, E. Rogers, M. Kulesza, D. Holland, J. Gafford, E. Goldfield, C. Walsh, Soft Wearable Orthotic Device for Assisting Kicking Motion in Developmentally Delayed Infants. *J. Med. Devices*. **9**, 30913 (2015).

226. Y.-L. Park, B. Chen, N. O. Pérez-Arancibia, D. Young, L. Stirling, R. J. Wood, E. C. Goldfield, R. Nagpal, Design and control of a bio-inspired soft wearable robotic device for ankle–foot rehabilitation. *Bioinspir. Biomim.* **9**, 16007 (2014).

227. C. T. O'Neill, N. S. Phipps, L. Cappello, S. Paganoni, C. J. Walsh, in *Rehabilitation Robotics (ICORR), 2017 International Conference on* (IEEE, 2017), pp. 1672–1678.

228. N. J. Holland, G. M. Weiner, Recent developments in Bell's palsy. *BMJ*. **329**, 553–557 (2004).

229. M. J. Sheehan, M. W. Nachman, Morphological and population genomic evidence that human faces have evolved to signal individual identity. *Nat. Commun.* **5**, 4800 (2014).

230. D. Jayatilake, T. Isezaki, Y. Teramoto, K. Eguchi, K. Suzuki, Robot Assisted Physiotherapy to Support Rehabilitation of Facial Paralysis. *IEEE Trans. Neural Syst. Rehabil. Eng.* **22**, 644–653 (2014).

231. D. Jayatilake, K. Suzuki, in *2008 IEEE/RSJ International Conference on Intelligent Robots and Systems* (2008), pp. 4048–4053.

232. D. Jayatilake, K. Suzuki, Robot assisted facial expressions with segmented shape memory alloy actuators. *Int. J. Mechatron. Autom.* **1**, 224–235 (2011).

233. A. Firouzeh, thesis, Ecole Polytechnique Fédérale de Lausanne (2017).

234. A. Firouzeh, J. Paik, in *IEEE/RSJ International Conference on Intelligent Robots and Systems (IROS)* (2017).

235. Facial Paralysis | Conditions & Treatments | UCSF Medical Center, (available at https://www.ucsfhealth.org/conditions/facial_paralysis/).

236. C. H. Beurskens, P. G. Heymans, Positive effects of mime therapy on sequelae of facial paralysis: stiffness, lip mobility, and social and physical aspects of facial disability. *Otol. Neurotol.* **24**, 677–681 (2003).

237. R. F. Baugh, G. J. Basura, L. E. Ishii, S. R. Schwartz, C. M. Drumheller, R. Burkholder, N. A. Deckard, C. Dawson, C. Driscoll, M. B. Gillespie, R. K. Gurgel, J. Halperin, A. N. Khalid, K. A. Kumar, A. Micco, D. Munsell, S. Rosenbaum, W. Vaughan, Clinical Practice Guideline: Bell's Palsy. *Otolaryngol.-Head Neck Surg.* **149**, S1–S27 (2013).

238. R. W. Lindsay, M. Robinson, T. A. Hadlock, Comprehensive Facial Rehabilitation Improves Function in People With Facial Paralysis: A 5-Year Experience at the Massachusetts Eye and Ear Infirmary. *Phys. Ther.* **90**, 391–397 (2010).

239. J. VanSwearingen, Facial Rehabilitation: A Neuromuscular Reeducation, Patient-Centered Approach. *Facial Plast. Surg.* **24**, 250–259 (2008).

240. C. H. Beurskens, P. G. Heymans, Mime therapy improves facial symmetry in people with long-term facial nerve paresis: a randomised controlled trial. *Aust. J. Physiother.* **52**, 177–183 (2006).

241. M. S. Patel, D. A. Asch, K. G. Volpp, Wearable devices as facilitators, not drivers, of health behavior change. *Jama*. **313**, 459–460 (2015).

242. Y.-X. Hung, P.-C. Huang, K.-T. Chen, W.-C. Chu, What Do Stroke Patients Look for in Game-Based Rehabilitation. *Medicine (Baltimore)*. **95** (2016), doi:10.1097/MD.0000000000003032.

243. C. B. Novak, Rehabilitation Strategies for Facial Nerve Injuries. *Semin. Plast. Surg.* **18**, 47–52 (2004).

244. P. M. Niedenthal, Embodying Emotion. *Science*. **316**, 1002–1005 (2007).

245. J. G. Neely, R. G. Pomerantz, Measurement of Facial Muscle Strength in Normal Subjects. *The Laryngoscope*. **112**, 1562–1568 (2002).

246. B. Palmer, D. Gershbein, *The wearables for good challenge* (http://wearablesforgood.com/WearablesForGood-UseCaseHandbook.pdf).

247. J. Lee, D. Kim, H.-Y. Ryoo, B.-S. Shin, Sustainable Wearables: Wearable Technology for Enhancing the Quality of Human Life. *Sustainability*. **8**, 466 (2016).

248. Soft Somatosensitive Actuators via Embedded 3D Printing - Truby - 2018 - Advanced Materials - Wiley Online Library, (available at https://onlinelibrary-wiley-com.ezproxy.proxy.library.oregonstate.edu/doi/full/10.1002/adma.201706383).

249. M. Acer, M. Salerno, K. Agbeviade, J. Paik, Development and characterization of silicone embedded distributed piezoelectric sensors for contact detection. *Smart Mater. Struct.* **24**, 75030 (2015).

250. H. A. Sonar, J. Paik, Soft Pneumatic Actuator Skin with Piezoelectric Sensors for Vibrotactile Feedback. *Front. Robot. AI*. **2** (2016), doi:10.3389/frobt.2015.00038.

251. R. K. Kramer, C. Majidi, R. J. Wood, in *2011 IEEE International Conference on Robotics and Automation* (2011), pp. 1103–1107.

252. D. Yang, M. S. Verma, J.-H. So, B. Mosadegh, C. Keplinger, B. Lee, F. Khashai, E. Lossner, Z. Suo, G. M. Whitesides, Buckling Pneumatic Linear Actuators Inspired by Muscle. *Adv. Mater. Technol.* **1**, 1600055 (2016).

253. Yang Dian, Verma Mohit S., Lossner Elton, Stothers Duncan, Whitesides George M., Negative-Pressure Soft Linear Actuator with a Mechanical Advantage. *Adv. Mater. Technol.* **2**, 1600164 (2017).

254. M. A. Robertson, J. Paik, *Sci. Robot.*, in press, doi:10.1126/scirobotics.aan6357.

255. D. Yang, B. Mosadegh, A. Ainla, B. Lee, F. Khashai, Z. Suo, K. Bertoldi, G. M. Whitesides, Buckling of Elastomeric Beams Enables Actuation of Soft Machines. *Adv. Mater.* **27**, 6323–6327 (2015).

256. A. Ainla, M. S. Verma, D. Yang, G. M. Whitesides, Soft, Rotating Pneumatic Actuator. *Soft Robot.* (2017), doi:10.1089/soro.2017.0017.

257. M. S. Verma, A. Ainla, D. Yang, D. Harburg, G. M. Whitesides, A Soft Tube-Climbing Robot. *Soft Robot.* (2017), doi:10.1089/soro.2016.0078.

258. V. Arabagi, O. Felfoul, A. H. Gosline, R. J. Wood, P. E. Dupont, Biocompatible Pressure Sensing Skins for Minimally Invasive Surgical Instruments. *IEEE Sens. J.* **16**, 1294–1303 (2016).

259. Y. Takema, Y. Yorimoto, M. Kawai, G. Imokawa, Age-related changes in the elastic properties and thickness of human facial skin. *Br. J. Dermatol.* **131**, 641–648 (1994).

260. M. Pawlaczyk, M. Lelonkiewicz, M. Wieczorowski, Age-dependent biomechanical properties of the skin. *Adv. Dermatol. Allergol. Dermatol. Alergol.* **30**, 302–306 (2013).

261. Creating a Silicone Suture Pad. *Smooth- Inc*, (available at https://www.smooth-on.com/tutorials/creating-silicone-suture-pad/).

262. W. F. Larrabee, A finite element model of skin deformation. I. Biomechanics of skin and soft tissue: A review. *The Laryngoscope*. **96**, 399–405 (1986).

263. M. H. Siddiqi, R. Ali, A. M. Khan, E. S. Kim, G. J. Kim, S. Lee, Facial expression recognition using active contour-based face detection, facial movement-based feature extraction, and non-linear feature selection. *Multimed. Syst.* **21**, 541–555 (2015).

264. N. M. Duc, B. Q. Minh, Your face is not your password face authentication bypassing lenovo–asus–toshiba. *Black Hat Brief.* **4**, 158 (2009).

265. M. T. Mahmood, *Face detection by image discriminating* (2006).